

# **Imaging Electrons in Ultra-thin Nanowires**

A thesis presented

by

Erin E. Boyd

to

The Department of Physics  
in partial fulfillment of the requirements  
for the degree of  
Doctor of Philosophy  
in the subject of

Physics

Harvard University  
Cambridge, Massachusetts

January 2011

©2011 – Erin E. Boyd

All rights reserved.

Thesis advisor

Author

**Robert M. Westervelt**

**Erin E. Boyd**

## **Imaging Electrons in Ultra-thin Nanowires**

### **Abstract**

Ultra-thin semiconductor nanowires are promising systems in which to explore novel low-dimensional physics and are attractive candidates for future nanoelectronics. Ultra-thin nanowires with diameters of 20 to 30 nm are essentially one-dimensional (1D) for moderate electron number, because only one radial subband is occupied. Low-temperature scanning gate microscopy is especially well suited for improving our understanding of nanowires in order to optimize the construction of nanowire systems. We use a home-built liquid-He cooled scanning gate microscope (SGM) to probe and manipulate electrons beneath the surface of devices. The SGM's conductance images are obtained by scanning the charged SGM tip above the sample and recording the change in conductance through the device as a function of tip position.

We present simulations of extracting the amplitude of the 1D electron wavefunction along the length of the quantum dot in an ultra-thin InAs/InP heterostructure nanowire (diameter = 30 nm) using a SGM. A weakly perturbing SGM tip slightly dents the electron wavefunction inside the quantum dot, and we propose measuring the change in energy of the dot due to the perturbation as a function of tip

position. By measuring the change in energy of the dot and by knowing the form of the tip potential, the amplitude of the wavefunction can be found. This extraction technique could serve as a powerful tool to improve our understanding of electron behavior in quasi-1D systems.

We have used our SGM to image the conductance through an ultra-thin (diameter  $\sim 30$  nm) InAs nanowire with two InP barriers. Our imaging technique provides detailed information regarding the position and flow of electrons in the nanowire. We demonstrate that the charged SPM tip's position or voltage can be used to control the number of electrons on the quantum dots. We spatially locate three quantum dots in series along the length of the ultra-thin nanowire. Using energy level spectroscopy and the conductance images, we find the length of all three of the dots, and we determine the dots' relative coupling strength.

# Table of Contents

Title Page . . . . .	i
Abstract . . . . .	iii
Table of Contents . . . . .	v
Acknowledgements . . . . .	vii
<b>Chapter 1: Introduction</b>	<b>1</b>
1.1 Motivation and background . . . . .	2
1.2 Overview . . . . .	7
<b>Chapter 2: Semiconductor nanowires and quantum dots</b>	<b>12</b>
2.1 Overview . . . . .	12
2.2 InAs/InP heterostructure nanowires . . . . .	13
2.3 Quantum dots and Coulomb blockade . . . . .	16
2.4 Coulomb blockade imaging technique . . . . .	23
2.5 Multiple quantum dots . . . . .	27
<b>Chapter 3: Experimental techniques</b>	<b>32</b>
3.1 Sample fabrication . . . . .	32
3.1.1 Nanowire growth . . . . .	33
3.1.2 Si wafer preparation . . . . .	34
3.1.3 Photolithography . . . . .	35
3.1.4 Electron beam lithography . . . . .	37
3.1.5 Nanowire deposition . . . . .	39
3.1.6 Electrically contacting nanowires . . . . .	41
3.1.7 Mounting sample . . . . .	43
3.2 Low-temperature scanning gate microscopy . . . . .	46
3.2.1 Scanning gate microscope – mechanical . . . . .	46
3.2.2 Scanning gate microscope – electrical . . . . .	53
3.2.3 Imaging procedure . . . . .	55

<b>Chapter 4: Imaging the amplitude of the wavefunction of a quantum state</b>	<b>57</b>
4.1 Overview . . . . .	57
4.2 Model . . . . .	59
4.3 Extracting the wavefunction - imaging mechanism . . . . .	61
4.3.1 Density profile $ \Psi ^2$ . . . . .	63
4.3.2 Tip potential $\Phi_{tip}$ . . . . .	64
4.3.3 Convolution - change in energy $\Delta E_N(x_{tip})$ . . . . .	65
4.3.4 Deconvolution - $ \Psi_{ext} ^2$ . . . . .	67
4.4 Imaging resolution . . . . .	67
4.4.1 Accuracy of $\Phi_{tip}$ and $\Delta E(x_{tip})$ . . . . .	68
4.4.2 Relative width of tip potential $\Phi_{tip}$ and wavefunction features	69
4.5 Measuring the energy shift $\Delta E_N$ - experimental setup . . . . .	71
<b>Chapter 5: Imaging quantum dots in 1D ultra-thin InAs/InP nanowires</b>	<b>78</b>
5.1 Overview . . . . .	78
5.2 Ultra-thin InAs/InP nanowire devices . . . . .	82
5.3 Experimental results - traditional transport measurements . . . . .	86
5.4 Experimental results - SGM images of ultra-thin InAs/InP nanowires .	87
5.4.1 Quantum dot number and location . . . . .	87
5.4.2 Quantum dot size . . . . .	90
5.4.3 Capacitances of epitaxial dot . . . . .	97
5.5 Metal/semiconductor contacts . . . . .	100
<b>Chapter 6: Summary and future directions</b>	<b>101</b>
<b>Bibliography</b>	<b>104</b>
<b>Appendix A: Fitting the plane at cold temperatures</b>	<b>110</b>

# Acknowledgements

I have received advice and support from a wide range of people during the past five and a half years as I worked on my Ph.D. at Harvard. I would like to thank all of these people who have been instrumental in encouraging me to reach this point. First, I want to thank my advisor, Bob Westervelt, for always making time to talk when I had a question or puzzle and providing a very strong understanding of the big-picture. I would especially like to thank him for his support of my goal to transition into a career in science and technology policy. The other two members of my committee, Rick Heller and Amir Yacoby, have also been very helpful in ensuring my research project stayed on track.

I was fortunate to collaborate with Dr. Mike Stopa, who is a gifted teacher and an exceptional scientist. I would like to thank Mike for his clear explanations and the time at the white board that made density functional theory and other complex systems and methods easily accessible.

In the Westervelt group, I have been very fortunate to work with a superb group of individuals who are talented scientists and who also foster a fun work environment. I would like to thank the members of the imaging group, Ania Bleszynski-Jayich, Kathy Aidala, and Parisa Fallahi, who were finishing-up when I began my Ph.D. They supplied me with a wealth of knowledge before they left the Westervelt group and continued to be an important source of information via phone calls and their Ph.D. theses throughout my

doctoral work. Halvar Trodahl and I joined the Westervelt imaging group at the same time and worked closely for the first few years of our studies. I would like to thank Halvar for being there to learn together with us as we began our Ph.D.s and more recently, as we have developed our own projects, for being a sounding board to trouble-shoot challenges as they arise. Dr. Jesse Berezovsky was a postdoctoral fellow in the imaging side of the Westervelt group during the middle of my time in the Westervelt group. I would like to thank Jesse for bringing his research experience and problem-solving skills to bear on the scanning gate microscope to create a more reliable system with less down time.

I would also like to thank the members of the Westervelt group from the non-imaging side of the lab, especially Keith Brown for fruitful discussions and for providing assistance whenever I had a computer question and Alex Nemiroski for thoughtful conversations. It has been fun getting to know the new students in the lab, Sagar Bhandari and Casper Floryan, and I wish them the best of luck. I would also like to thank Naomi Brave for keeping the Westervelt group running smoothly, for being a whiz with paperwork, and for being a fun person to chat with!

The work in this thesis would not have been possible without the collaboration with the talented scientists from Lund University. I would like to thank Professor Lars Samuelson for sharing his group's expertise on nanowire growth and for the hospitality I was shown when visiting. I would like to thank Linus Fröberg, who was the graduate student on the project when I began my Ph.D., for sharing his expertise on nanowires. Kristian Storm is the current graduate student with whom I have been working on the

project. I would like to thank him for his perseverance in growing nanowires with a wide range of properties, even when the fabrication equipment was not cooperating.

I would like to thank all of Harvard's Center of Nanoscale Systems' staff for keeping the cleanroom running and doing a great job. I would especially like to thank Noah Clay for being amazingly accessible, to solve both scientific challenges and administrative ones.

Sheila Ferguson is the Wonder Woman for Harvard's physics graduate students. When I had a question or problem, Sheila found the answer or pointed me to the best resource. Thank you Sheila for all your help over the past 5 years. It has meant so much to me.

During my time at Harvard, I had the opportunity to become involved with the student organization Harvard Graduate Women in Science and Engineering (HGWISE). This was an amazing experience. I had the opportunity to get to know and learn from people at all levels of the university, from deans to fellow graduate students. I would like to give a special thank you to the other women with whom I served on the executive board, Eun-Young Choi, Eliza Morris, Tess Williams, and Emily Gardal. I learned a great deal working with them and seeing the different ways in which they approached challenges. I would also like to thank all the GSAS dean's and the Office of Career Services councilors with whom I worked, especially Dean Margot Gill for being a strong female role model for me.

I would like to thank all my friends at Harvard and elsewhere that have listened about my research and Ph.D. when I needed to talk and have otherwise always been there to relax and have fun with.

The love and support of my family was been crucial to my success and happiness during my doctoral work. I would like to thank my father David Boyd for sharing his love of science with me and for always encouraging me to use the gifts God gave me. It was fun to take undergraduate physics courses at the same time as he and for me to be able to help him with physics problems. I want to thank my mother Rosa Snyder-Boyd for always being there to encourage me and to listen, even if that often meant talking about non-physics topics during frustrating times. I want to thank my grandmother Arlene Snyder for always loving me and being proud of me and for sending me “angels” and thanks to my brother Chris for his faith and support. I want to thank Ken Ofslager for his ideas and encouragement and for sharing his expertise, which made my thesis work stronger. Thank you to my fiancé Michael for his endless support, encouragement, and love and for always believing I can accomplish my goals. Thank you for always being there to laugh, cry, and celebrate with and for being a wonderful friend.

# Chapter 1

## Introduction

This thesis describes the usefulness of scanning gate microscopy for characterizing ultra-thin semiconductor nanowires in order to study novel 1D physical phenomena and to optimize the nanowires' characteristics for use in future applications such as nanoelectronics. We demonstrate that scanning gate microscopy is a powerful tool for extracting information about electrons beneath the surface of a device, which are confined in very small nanostructures. In chapter 2, we lay out the theory behind quantum dots and the Coulomb blockade effect, which is the effect that provides the contrast mechanism in scanning gate microscope (SGM) conductance images of quantum dots. Chapter 3 covers device fabrication, the experimental setup of our SGM, and the Coulomb blockade imaging technique. In chapter 4, we present simulations to demonstrate an SGM imaging technique to extract the amplitude of the 1D electronic wavefunction of a quantum dot. Conductance images of ultra-thin InAs/InP nanowires are presented in chapter 5. We use the SGM to find the number and location of all

quantum dots in the system, their relative sizes, and the coupling strength. Chapter 6 summarizes our findings.

## 1.1 Motivation and background

Nanoscale science and technology addresses materials and devices at approximately the 1 to 100 nanometer (nm) size scale. Materials on this size scale behave intrinsically differently than in their bulk form, opening the door to a variety of novel applications. Research and development is currently focused on understanding and harnessing these unique properties of nanomaterials to develop new technologies, such as spintronics or quantum information processing, and to design materials and structures with properties tailored to meet the needs of a variety of industries, such as electronics, energy, health, and agriculture.

Semiconductor nanowires are generating significant attention as building blocks for future nanoelectronic circuits and sensing technologies [Lieber 2003; Samuelson *et al.* 2004; Yang *et al.* 2005]. One class of nanowires, semiconductor heterostructure nanowires, is comprised of alternating layers of semiconductor material. The variations in nanowire composition allow one to manipulate the electron flow through the device. Figure 1.1(a) demonstrates that high quality heterostructure nanowires with sharp transitions between material layers, well-defined individual atomic planes, and uniform diameter can be grown from a bottom-up approach [Björk *et al.* 2002]. Figure 1.1(b) shows that there is also a high level of control over the location, length, and diameter of the nanowires.

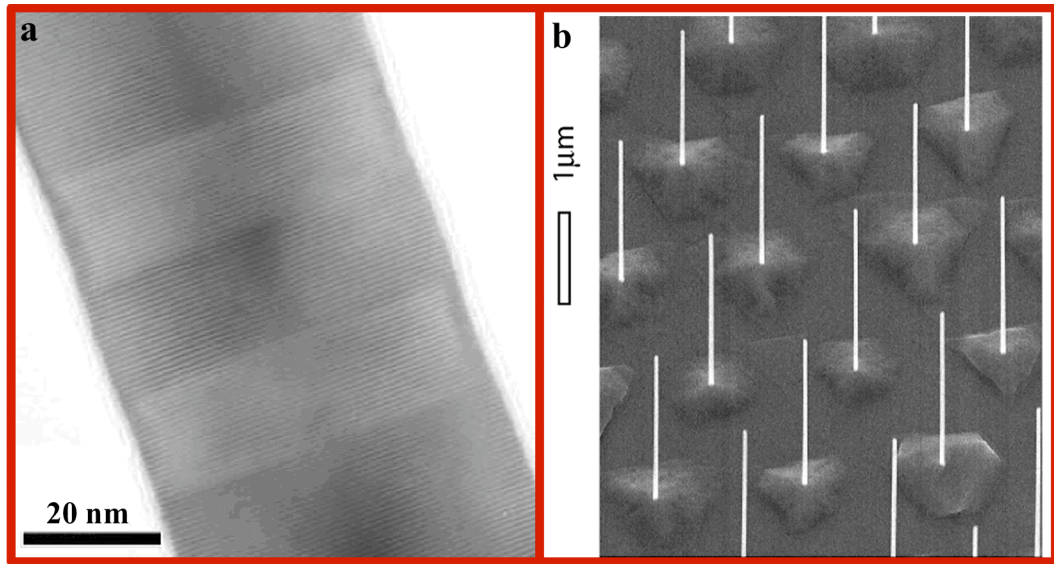


**Figure 1.1:** (a) Transmission electron microscope (TEM) image of an InAs (dark areas) and InP (light areas) nanowire. The interfaces between the two materials are sharp and the individual atomic planes are visible [Björk *et al.* 2002]. (b) Scanning electron microscope (SEM) micrograph of an array of InAs/InP nanowires, which demonstrates a high level of control over nanowire placement, length, and diameter [Jensen *et al.* 2004].

Quantum mechanical phenomena play a crucial role in determining the properties of nanomaterials and nanostructures. Electron waves cannot be treated as classical particles. The wave-particle duality of matter becomes apparent in these systems. Figure 1.2 shows one result of quantum mechanics, which is that an electron, which is represented by a wavepacket, has a non-zero probability of “tunneling” through a potential barrier, over which the electron does not have enough energy to pass. With two or more barriers present, the tunneling process forms confined electronic states, which are called quantum dots. In figure 1.2 the continuum of states in the source and drain leads is represented by the purple regions, with the highest occupied state in the source and the

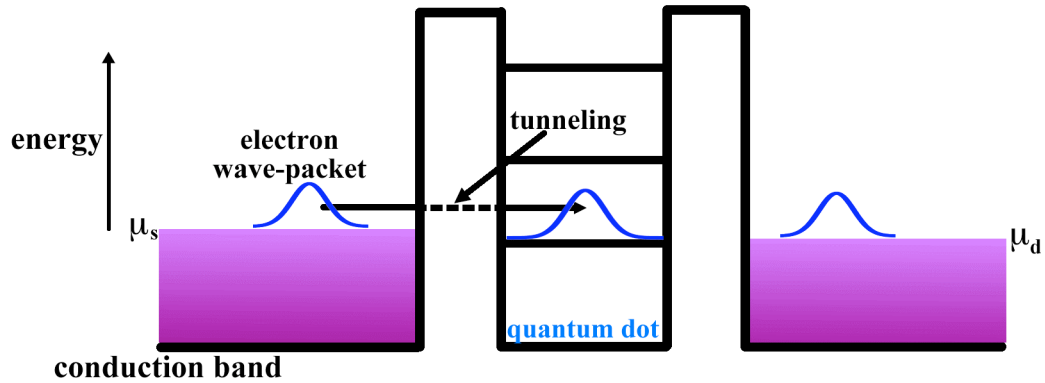


**Figure 1.2:** An example of a conduction band for a nanowire with alternating layers of semiconductor. Classically an electron, represented here by a wavepacket, would need to have enough energy to pass over the barrier. However, due to the quantum mechanical nature of electrons there is a probability that the electron can tunnel through the barrier. The presence of the second barrier forms a confined region of electrons (quantum dot) in the nanowire. The purple regions correspond to the continuum of states located in the source and the drain. The highest occupied state in the source and drain is given by the chemical potentials  $\mu_s$  and  $\mu_d$  respectively. The electron has a probability of tunneling into one of the unoccupied discrete states in the quantum dot that is located between  $\mu_s$  and  $\mu_d$ .

drain being located at the chemical potential  $\mu_s$  and  $\mu_d$  respectively. An electron tunnels into a confined state on the quantum dot, which has a discrete energy spectrum. The various materials used to produce heterostructure nanowires (e.g. indium arsenide (InAs) and indium phosphide (InP)) have different values for the electron conductance band edge and band offsets, which allows the precise placement of barriers and quantum dots in a nanowire in order to tailor the device to a specific application.

Ultra-thin heterostructure nanowires (diameter  $d_{NW} \sim 20$  to  $30$  nm) are especially exciting systems to study, because only one radial subband is occupied at moderate electron number, making ultra-thin nanowires effectively one-dimensional (1D) systems. In addition to developing new technologies and applications with ultra-thin nanowires,

there is great enthusiasm for expanding the understanding of novel 1D physical phenomena such as electron spin-charge separation [Auslaender *et al.* 2005], the charge density probability [Fallahi 2006], and the transition from a Luttinger Liquid to a Wigner Crystal as the charge carrier density decreases [Matveev 2004; Deshpande and Bockrath 2008; Qian *et al.* 2010].

Despite the intensive research in the field, many gaps remain in understanding how best to design nanostructures for applications. Spatial imaging of nanostructure devices is well suited to help answer these questions. Compared to transport measurements that supply information about the average characteristics over the entire device, imaging provides a means to locally probe and influence the spatial electronic properties of the device.

An assortment of scanning probe microscopes (SPMs) exists that offer a variety of imaging mechanisms to gather information about diverse properties of nanomaterials. For example, atomic force microscopes (AFMs) provide topographical maps of a sample surface, and scanning tunneling microscopes (STMs) supply information about the electrons on the surface of a conducting sample. Meyer *et al.* (2004) provides a broad review of SPMs. I used a home-built liquid-He cooled scanning gate microscope (SGM) to probe and manipulate electrons in an ultra-thin nanowire. Figure 1.3 shows a schematic of an SGM. No current flows between the tip and the device. Rather the tip and the electron gas are capacitively coupled, which allows the SGM to study electrons that are near the tip, but not touching. SGMs have a charged tip that serves as a local movable gate or scatterer in the system via the capacitive coupling  $C_{t-d}$  between the tip

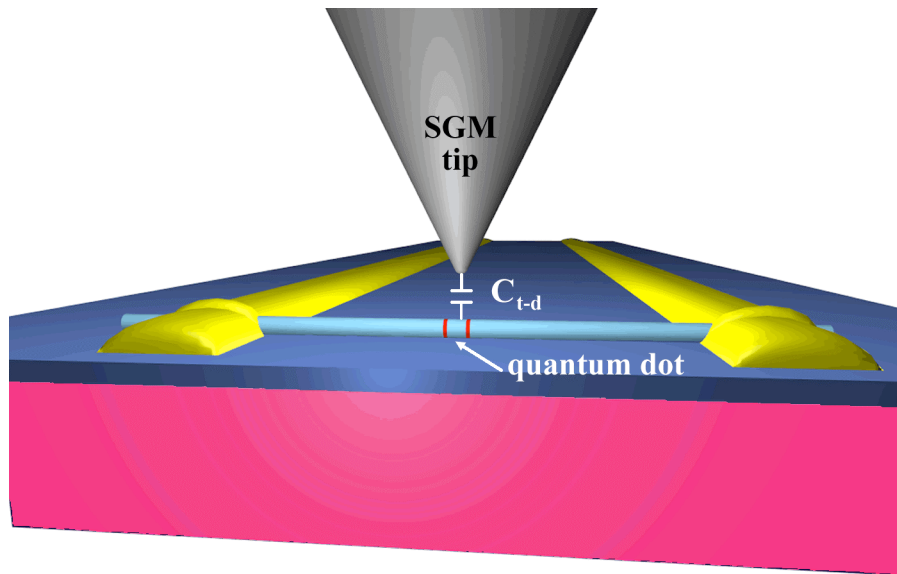


**Figure 1.3:** Sketch of a scanning gate microscope set-up. The imaging mechanism is the change in capacitance  $C_{t-d}$  between the charged tip and the device. The SGM tip serves as a movable local gate in the system to probe electrons beneath the surface and influence their motion. The tip is raster scanned at a constant height above the surface and the change in conductance through the device is measured.

and the sample. The SGM allows the extraction of spatial information regarding the electrons that are buried beneath the surface of a sample, which is quite relevant when considering electrons in nanoelectronic devices. Additionally, the SGM can manipulate the charge carriers under the tip. The Westervelt group has imaged electron flow in two-dimensional electron gases (2DEGs) using the movable tip as a scatterer [Topinka *et al.* 2000; Topinka *et al.* 2001; LeRoy *et al.* 2002; LeRoy *et al.* 2005; Aidala *et al.* 2007] and in graphene [Berezovsky *et al.* 2010a; Berezovsky *et al.* 2010b]. Additionally, the Westervelt group has imaged electrons in quantum dots using the tip as a movable gate [Fallahi *et al.* 2005; Bleszynski *et al.* 2006; Bleszynski-Jayich *et al.* 2008]. Several other groups also use SGMs to study electrons beneath the surface, including the Ensslin group

in 2DEGs [Gildemeister *et al.* 2007] and graphene [Schnez *et al.* 2010], the McEuen group in carbon nanotubes [Woodside and McEuen 2002], and the Goldhaber-Gordon group who have imaged electron flow in 2DEGs [Jura *et al.* 2007]. The information that is acquired from SGM images is useful in designing and implementing nanoelectronics and in extending the understanding of unique physical phenomena.

## 1.2 Overview

This thesis begins in chapter 2 with a thorough description of the Coulomb blockade imaging mechanism. The Coulomb blockade effect is the suppression of current through a device where the charge is quantized in integer multiples of  $e$  and the self-capacitance of the device requires a relatively large amount of energy to add an electron to the device. We review the conditions necessary for a device to exhibit the Coulomb blockade effect and how multiple quantum dots in series influence electron transport. InAs/InP heterostructure nanowires are investigated in this thesis due to the particularly favorable properties of InAs, such as a large electron affinity at the surface and a large g-factor.

I have put a good deal of effort into developing a batch fabrication process to make nanowire samples that are ready for imaging as described in chapter 3. As part of our collaboration, the Samuelson group at Lund University grows the InAs/InP heterostructure nanowires, and we perform the bulk of the processing to prepare the nanowires for imaging. Chapter 3 also presents a description of the home-built liquid-He cooled SGM design and operation. Figure 1.4 is a photo of the microscope and dewar.



**Figure 1.4:** Preparing the SGM to cool down to liquid-He temperatures. (See chapter 3 for a detailed description of the experimental apparatus.)

InAs/InP ultra-thin nanowires are effectively 1D for a moderate number of electrons, because only one radial subband is occupied. By being effectively 1D, ultra-thin nanowires offer the possibility of extracting information about the electron wavefunction along the nanowire axis. We propose using a weakly perturbing SGM tip to slightly dent the wavefunction. By measuring the change in energy of the dot as a function of tip position, we could then map the amplitude of the 1D wavefunction (charge probability density) along the length of the nanowire. I perform computations to show the viability of this imaging and extraction technique, which is the topic of chapter 4. I consider a model with an ideal wavefunction to demonstrate the capability of the technique, but the method is viable on a system with any arbitrary wavefunction. The purpose of the extraction technique is to serve as a diagnostic tool to improve the

understanding of any system by supplying information about the system's ground state wavefunction. The knowledge gained would be useful in designing and implementing applications using quasi-1D nanostructures.

Figure 1.5(a) shows a model of the change in energy  $\Delta E$  of a quantum dot as the SGM tip is scanned in a straight line along the nanowire axis. The change in energy  $\Delta E$  of the dot is what would be measured in an experiment. This plot will be discussed in more detail in chapter 4, but for now we note the two peaks in  $\Delta E$ . Figure 1.5(b) shows the potential  $\Phi_{tip}$  from a negatively charged SGM tip held above the sample. By knowing the information in both figure 1.5(a) and figure 1.5(b), the 1D amplitude of the wavefunction  $|\Psi|^2$  of the state is extracted, Figure 1.5(c). We note that the amplitude of the wavefunction  $|\Psi|^2$  has two very well defined peaks. A simple picture to help understand the extraction technique is to consider that the tip potential  $\Phi_{tip}$  (figure 1.5(b)) blurs out the wavefunction features  $|\Psi|^2$  (figure 1.5(c)) to give the change in energy of the dot  $\Delta E$  (figure 1.5(a)). However, by mathematically reversing the tip's effect the original amplitude of the wavefunction can be found. The imaging technique we propose combines Coulomb blockade transport measurements with a weakly perturbing SGM tip to perform energy level spectroscopy and wavefunction extraction with the same experimental setup.

There is much interest in producing very clean high quality nanowires for studying the physics of 1D systems and for use in future nanoelectronics and sensor technologies. Scanning gate microscopy is well suited to providing images that will assist in developing high quality nanowires, because it can image where electrons reside

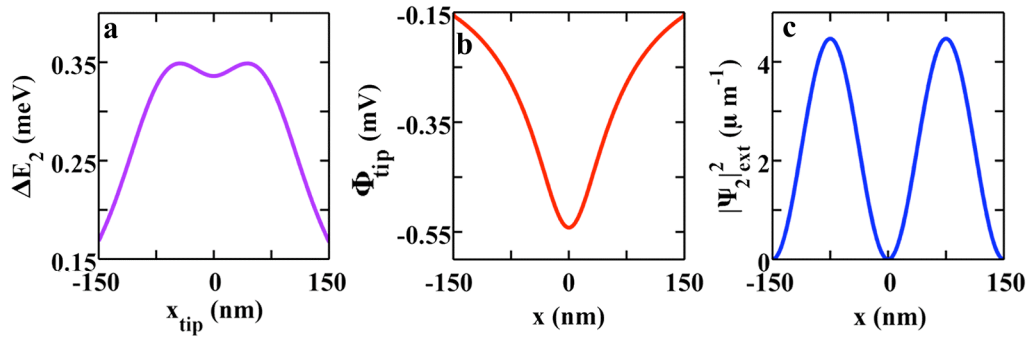


**Figure 1.5:** Theoretical results of extracting the amplitude of the electron wavefunction  $|\Psi|^2$  in an ultra-thin nanowire quantum dot. (a) Shows the change in energy  $\Delta E(x_{tip})$  of the dot's state vs. tip position  $x_{tip}$  as the tip is scanned in a straight line above the wire. The change in energy  $\Delta E$  is the quantity that would be measured experimentally. (b) Plots the tip potential  $\Phi_{tip}$  from a negatively charged tip held above the nanowire. (c) By mathematically reversing the effect of the SGM tip, the amplitude of the wavefunction  $|\Psi|^2$  can be extracted from the measured change in energy  $\Delta E$ . (See chapter 4 for a more in-depth discussion of the extraction technique.)

in the nanowire and how electrons flow through the device. SGM conductance images contain information about the number of quantum dots, the location, size, and capacitance of quantum dots, and the energies of the system, as discussed in chapter 5.

Figure 1.6 is a SGM conductance image of an ultra-thin InAs nanowire with two InP tunnel barriers. The conductance is plotted as a function of the tip position as the tip is scanned over the device. Figure 1.6(a) shows the area over the nanowire that was scanned with respect to the leads. Figure 1.6(b) will be analyzed in more detail in chapter 5, but for now we note the three sets of concentric elliptical conductance rings centered on each white circle. The center of each set of rings marks the location of a quantum dot. By moving the tip across a single ring, an electron is added to the quantum dot at its center. This image provides valuable information to optimize the growth process to

produce high quality wires. SGM conductance images disentangle the transport information for multi-dot systems by spatially resolving the Coulomb blockade rings for each dot. Scanning gate microscopy supplies information beyond that of optical microscopy or traditional transport measurements to aid in the development of very high quality 1D devices.

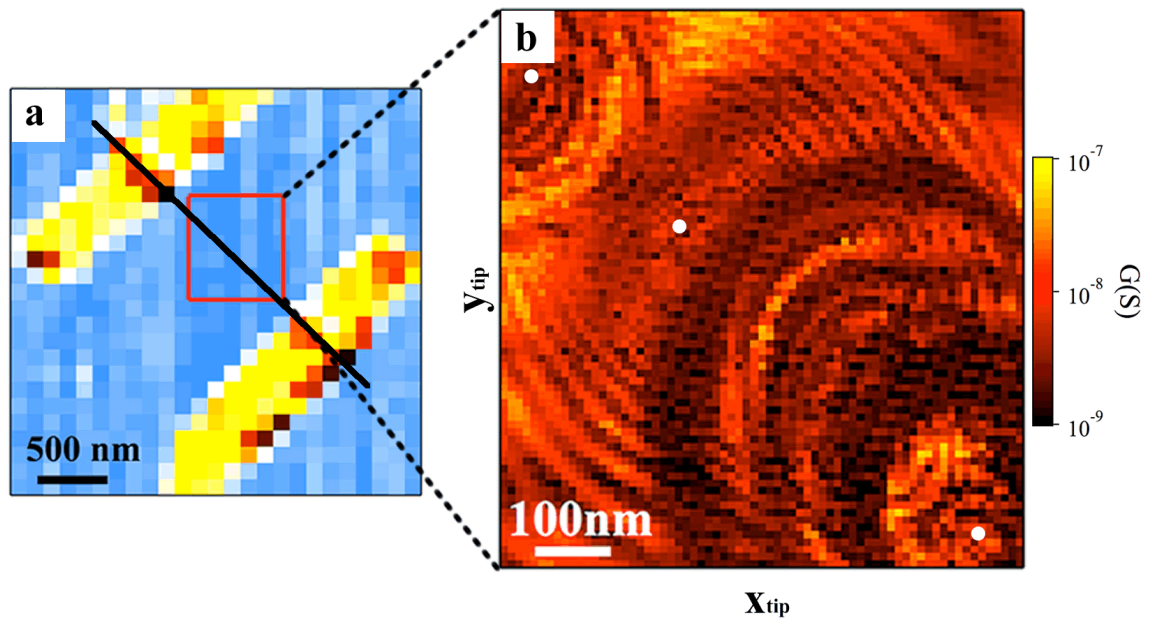


**Figure 1.6:** (a) Shows the location of the gold leads (yellow) and nanowire axis (black line) relative to the scan area (red box) in (b). (b) SGM conductance image from scanning over an ultra-thin InAs nanowire with two InP tunnel barriers. Three quantum dots are identified from the three sets of elliptical conductance rings centered on the white circles. In Chapter 5, we will discuss the additional information that can be found from such an image.

## **Chapter 2**

# **Semiconductor nanowires and quantum dots**

### **2.1 Overview**

Quantum dots in semiconductor nanowires are promising candidates for components in future nanotechnologies. In section 2.2, the advantages of studying semiconductor nanowires, specifically InAs/InP heterostructure nanowires, for use in future devices is explored. Section 2.3 introduces the theory of Coulomb blockade conductance in quantum dots for zero and finite source-drain bias. In section 2.4, we describe the Coulomb blockade imaging technique. Using the scanning gate microscope (SGM) tip as a movable gate, an image is obtained where the contrast is supplied by the change in conductance through the nanowire as the tip is scanned above the sample. This technique probes the quantum mechanical characteristics of electrons in confined

structures and gives control over electron flow through the nanowire. Finally in section 2.5, we introduce systems with multiple quantum dots and describe Coulomb blockade through multi-dot structures.

## 2.2 InAs/InP heterostructure nanowires

Semiconductor nanowires are promising candidates for use in future nanoelectronics, quantum information processing, and nanophotonics [Lieber 2003; Samuelson *et al.* 2004; Yang *et al.* 2005]. Bottom-up fabrication offers a high level of control over nanowire dimensions and composition [Hiruma *et al.* 1996; Ohlsson *et al.* 2001]. The variety of materials (e.g., InAs, InP, Si, Ge) with which nanowires can be grown provides flexibility in achieving desired material properties. Due to the small size scale of the quantum dots, quantum mechanical effects dominate and single electron devices are possible [Björk *et al.* 2004; Bleszynski-Jayich *et al.* 2008].

Imaging nanowires with a SGM provides information on how electrons flow through these confined structures. This information, while supplying insight into interesting low-dimensional physics, also has the potential to improve the control over the electronic properties of nanowires, so that nanowires can be manipulated to achieve new low-dimensional technologies. Understanding the spatial properties of electrons in nanowires aids in designing optimal nanoelectronics, such as nanowire transistors [Bryllert *et al.* 2006; Björk *et al.* 2008]. Semiconductor nanowires are attractive for use as building blocks for smaller and faster nanoelectronic circuits, and nanowires have the

capability to serve as interconnects and active devices in nanoelectronic circuits [Lieber 2003].

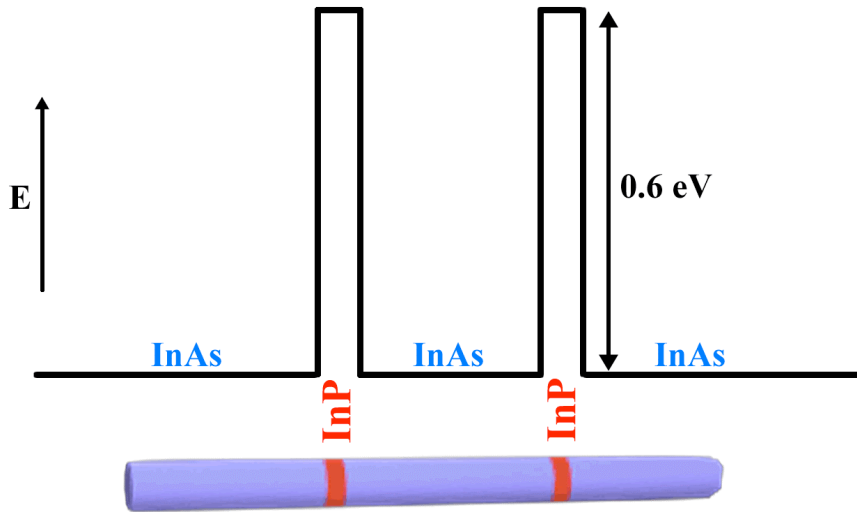


**Figure 2.1:** Alternating layers of InAs (blue) and InP (red) are grown using CBE. The conduction band offset between InAs and InP is approximately 0.6 eV. The deep potential well forms strong electronic confinement of the electrons in the quantum dot.

Chemical beam epitaxy (CBE) InAs/InP heterostructure nanowires are a particularly favorable system to probe low-dimensional semiconductor physics [Björk *et al.* 2002a; Björk *et al.* 2002b; Jensen *et al.* 2004]. InAs is known to have a charge accumulation layer at the surface [Olsson *et al.* 1996], which makes it possible to grow quantum dots in ultra-thin nanowires that are not depleted of electrons. InAs has a large  $g$ -factor, which can be varied from the bulk value of  $|g| = 14$  to 2 depending on the dot size [Björk *et al.* 2005], and a small effective mass, bulk value  $0.022m_e$ , increasing the ease of spin manipulation. InAs sections and InP barriers are grown by switching gas precursors during growth. Either triethylindium (TEIn) or trimethylindium (TMIn) is

used for the In growth source. TMIn contains higher amounts of carbon atoms, which effectively n-dopes the TMIn sections relative to the TEIn sections. In figure 2.1, the energy landscape of an InAs/InP nanowire is shown. The  $\sim 0.6$  eV conduction band offset between InAs and InP forms a potential well with strong electronic confinement.

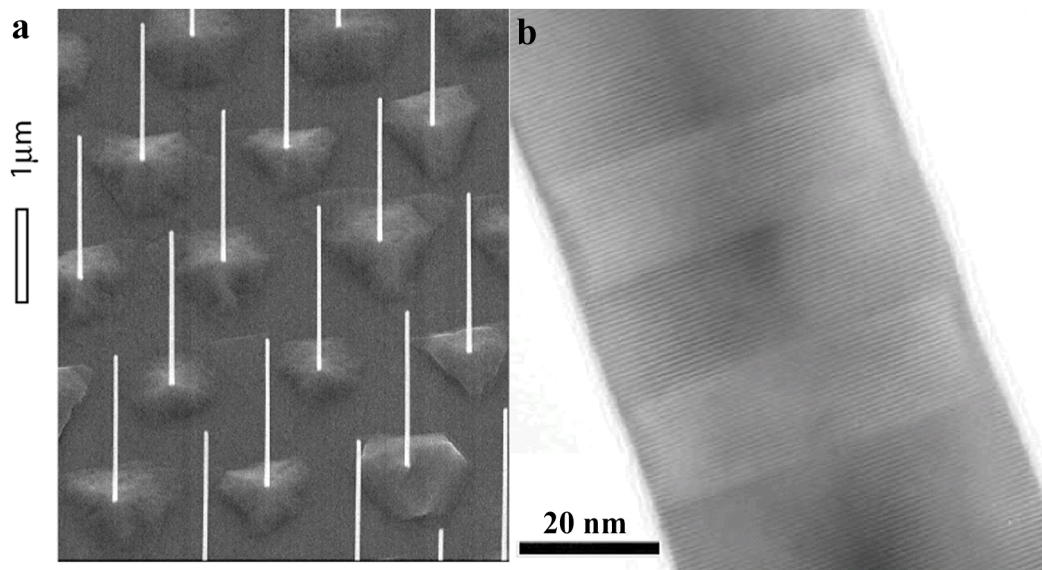


**Figure 2.2:** Images of InAs/InP heterostructure nanowires. (a) A scanning electron microscope (SEM) image of an array of nanowires grown with electron beam lithography patterned gold disks as catalysts [Jensen *et al.* 2004]. We note the uniformity of the nanowires' length and diameter. (b) A TEM image of a heterostructure nanowire. The lighter colored regions are InP and the darker regions are InAs. The precision of the atomic planes is seen in this image [Björk *et al.* 2002].

Growing nanowires using CBE gives precise control over the dot length and diameter, figure 2.2(a). Nanowires with very small diameters ( $d_{NW} \sim 20$  to 30 nm) can be grown with only one occupied subband in the radial direction for moderate electron number, producing nanowires that are effectively one-dimensional (1D). Figure 2.2(b) is

a transmission electron microscope (TEM) image of a short InAs quantum dot where the individual atomic layers are visible, showing that CBE can produce single crystal nanowires with atomically smooth surfaces [Jensen *et al.* 2004]. Quantum dots that are defined by tunnel barriers that are incorporated into the nanowire are especially favorable structures to study with an SGM when compared to dots that are defined by lateral metal top gates. The metal top gates exhibit strong shielding effects, which distort the image when a conducting SGM tip approaches the dot to image. In general, nanowires with in-grown quantum dots are desirable for nanoelectronic circuits due to the ease of production compared to dots that must be individually defined with top gates.

### 2.3 Quantum dots and Coulomb blockade

Electrons on a quantum dot are confined in all three dimensions. In a heterostructure nanowire, the diameter of the nanowire confines the electrons in two dimensions and the in-grown tunnel barriers confine the electrons along the length of the wire, figure 2.1. Due to the strong quantum confinement a dot contains an integer number of electrons and has a discrete energy spectrum.

Coulomb blockade is the suppression of current through a quantum dot, which occurs when the tunnel barriers provide sufficient isolation of the quantum dot from the leads ( $G \ll e^2/h$ ) so the charge on the dot is quantized, and an energy price must be paid to add an electron to the dot to overcome the Coulomb repulsion between electrons. The following conditions must be met for a quantum dot to exhibit Coulomb blockade. The charging energy  $E_c$  of the quantum dot, which is the energy required to add an electron to

the dot to overcome electrostatic repulsion, must be greater than the thermal energy of the system so that electrons do not tunnel due to the temperature [Kouwenhoven *et al.* 1991]:

$$E_C = e^2 / C_\Sigma \gg k_B T \quad (2.1)$$

where  $C_\Sigma$  is the total capacitance between the dot and the rest of the world,  $k_B$  is the Boltzman constant, and  $T$  is the electron temperature. Additionally, the resistance  $R$  through the device must be [Kouwenhoven *et al.* 1991]:

$$R \gg h / e^2 \quad (2.2)$$

Intuitively, smaller dots will have larger single particle energy spacings  $\Delta E_i$  from the greater electron confinement and a larger energy  $E_c$  needed to overcome the electrostatic repulsion and add an electron to the dot. However, Björk *et al.* (2004) found that for CBE grown InAs/InP nanowires, changes in the nanowire diameter have a greater effect on  $E_c$  than changes to the quantum dot length. The sizes of  $E_c$  and  $\Delta E_i$  in these nanowires were large compared to  $E_c$  and  $\Delta E_i$  of larger quantum dots defined in a 2 dimensional electron gas (2DEG). Larger energy spacings are desirable because quantum mechanical effects are more visible at a given temperature. The heterostructure nanowires presented in this work are in the Coulomb blockade regime due to the low operating temperature ( $T = 1.7\text{K}$  to  $4.2\text{ K}$ ), the small size of the quantum dot, and the weak coupling between the dot and the leads.

The theoretical parameters of a quantum dot in the Coulomb blockade regime are covered in detail in Beenakker (1991) and Kouwenhoven *et al.* (1991). The total energy  $U$  of a quantum dot with  $N$  electrons is the sum of the electrostatic energy and the energy of the occupied quantum states [Beenakker 1991]:

$$U(N) = \frac{(C_{bg-d}V_{bg} - Ne)^2}{2C_{\Sigma}} + \sum_{i=1}^N E_i \quad (2.3)$$

where  $C_{bg-d}$  is the capacitance between the backgate and dot,  $V_{bg}$  is the voltage applied to the backgate with respect to the dot, and  $E_i$  is the energy of the occupied single particle states. The chemical potential  $\mu_{dot}$  of a quantum dot with  $N$  electrons is [Kouwenhoven *et al.* 1991]:

$$\mu_{dot}(N) = U(N) - U(N-1) = \frac{e^2(N-1/2)}{C_{\Sigma}} - \frac{eC_{bg-d}V_{bg}}{C_{\Sigma}} + E_N \quad (2.4)$$

The addition energy  $E_{add}$  needed to add an electron to the quantum dot is the difference in chemical potentials of the dot with  $N+1$  and with  $N$  electrons.

$$E_{add} = \mu_{dot}(N+1) - \mu_{dot}(N) = E_c + E_{N+1} - E_N \quad (2.5)$$

Figure 2.3(a) is a graphical representation of the energy  $U$  of the dot vs. backgate voltage  $V_{bg}$  [Tinkham 1996]. This plot assumes that the single particle energy spacings are much less than the charging energy  $E_i \ll E_C^1$ , which produces Coulomb blockade conductance peaks that are periodic in  $V_{bg}$ , figure 2.3(b). If  $E_i$  and  $E_c$  are comparable then the spacing between Coulomb blockade peaks shifts and the periodicity is broken (discussed in Chapter 4). At the minimum of the parabola each charge state is stable and the total charge on the dot is fixed. The dot is in the Coulomb blockade regime and no current flows except when two parabolas intersect, and electrons are able to tunnel on and off the dot. At the intersection point the two charge states are degenerate in energy and

---

<sup>1</sup> This would be true for a large semiconductor quantum dot or for a metal or superconductor.

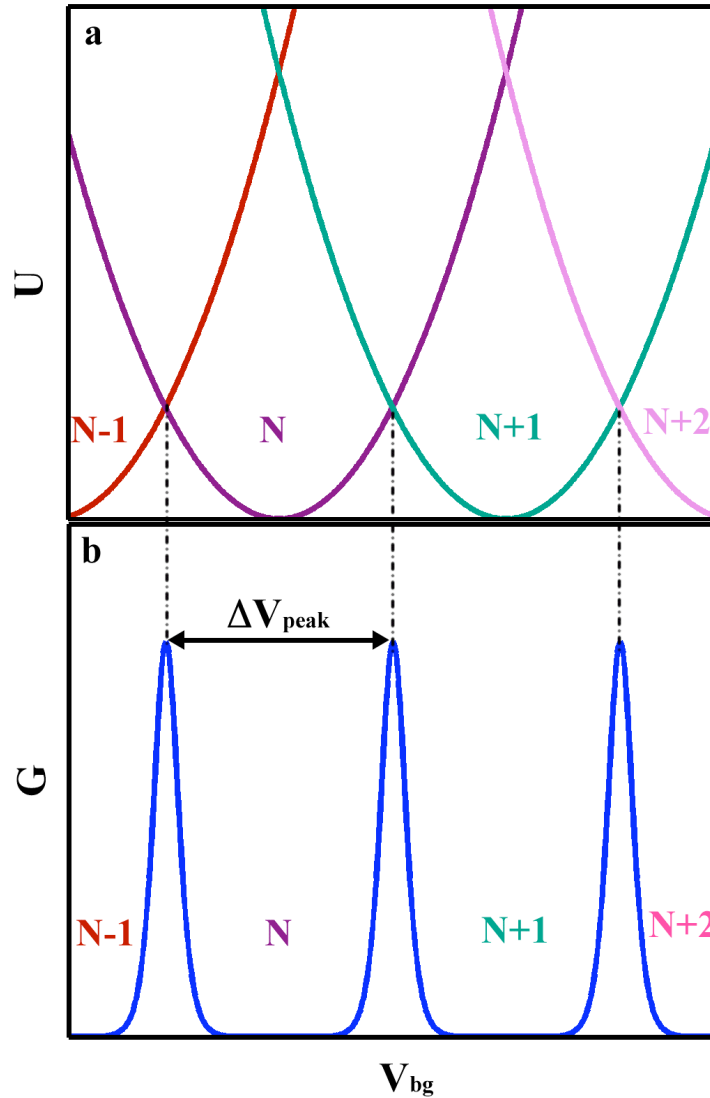


**Figure 2.3:** Coulomb blockade of a quantum dot where the single particle energies  $E_i$  can be neglected compared to the charging energy  $E_c$ . (a) A plot of the energy  $U$  of the dot vs. the backgate voltage  $V_{bg}$ . The charge on the dot is fixed, except when two parabolae intersect. At the intersection point the Coulomb blockade is lifted because having either  $N$  or  $N+1$  electrons on the dot is equally energetically favorable. (b) Sweeping  $V_{bg}$  tunes the number of electrons on the dot. The Coulomb blockade peaks occur at the backgate voltage  $V_{bg}$  where the parabolae intersect, and the electrons tunnel through a single quantum state. The change in  $V_{bg}$  between Coulomb peaks  $\Delta V_{peak}$  (equation 2.7) is proportional to the addition energy  $E_{add}$ . Therefore, the spacing between Coulomb peaks contains information about the shell structure of the dot.

the Coulomb blockade is broken. By tuning  $V_{bg}$ , the Coulomb blockade of a dot can be lifted. The backgate voltage  $V_{peak}$  at which two charge states are degenerate can be found by:

$$U(N-1) = U(N) \rightarrow \quad (2.6)$$

$$V_{peak} = (e/2C_{bg-d})(2N-1) + (C_{\Sigma}/eC_{bg-d})(E_N - E_{N-1})$$

The spacing  $\Delta V_{peak}$  between Coulomb blockade peaks in figure 2.3(b) can be found by setting  $U(N-1) = U(N)$  and  $U(N) = U(N+1)$ , finding the location of each peak, and subtracting to find  $\Delta V_{peak}$  or by recognizing that the chemical potential of each charge state must be equal, when the backgate voltage is set to where the Coulomb blockade is broken for that particular state:

$$\mu_{dot}(N+1, V_{bg} + \Delta V_{peak}) = \mu_{dot}(N, V_{bg}) \rightarrow \Delta V_{peak} = \frac{C_{\Sigma}}{eC_{bg-d}} \left( \frac{e^2}{C_{\Sigma}} + E_{N+1} - E_N \right) \quad (2.7)$$

Figure 2.4 illustrates that in order for current to flow through the nanowire the chemical potential of the dot  $\mu_{dot}$  must be equal to the chemical potential  $\mu_s$  of the source and the chemical potential  $\mu_d$  of the drain. By changing the applied  $V_{bg}$ , the chemical potential of the dot  $\mu_{dot}$  can be shifted with respect to  $\mu_s$  and  $\mu_d$  and the number of electrons on the dot can be controlled. The line-shape of the Coulomb blockade peaks for tunneling into a single quantum state (figure 2.3(b) and figure 2.4(b)) is given by [Beenakker 1991]:

$$G = G_{max} [\text{Cosh}(\Delta_{E_F} / 2k_B T)]^{-2} \quad (2.8)$$

where  $G_{max}$  is the maximum conductance through the nanowire and  $\Delta_{E_F}$  is the difference in energy between the lowest unoccupied energy level in the dot and the Fermi energy in the leads.

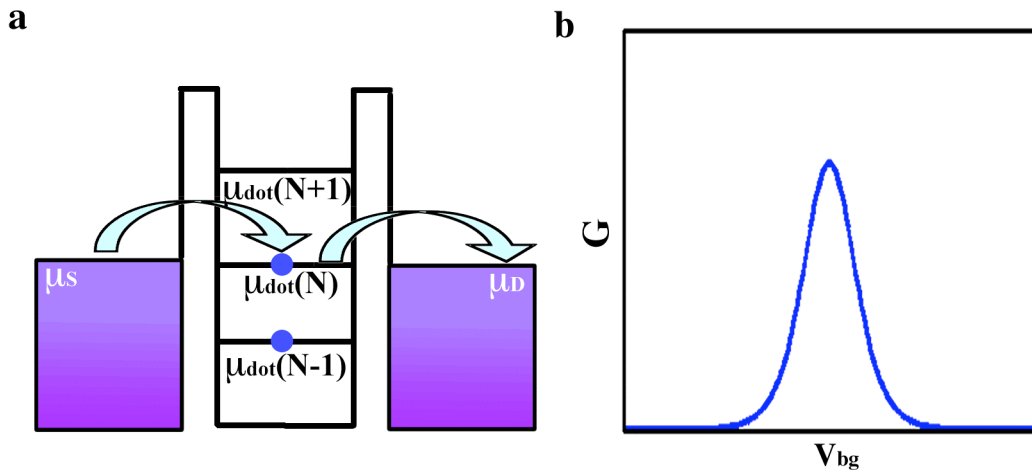


**Figure 2.4:** (a) At zero source-drain bias  $V_{sd}$ , the chemical potential  $\mu_{dot}$  of the dot must be in resonance with the Fermi energy of the leads for current to flow. If that condition is not met the conductance through the quantum dot is blocked. The backgate voltage  $V_{bg}$  is used to shift  $\mu_{dot}$  and control the number of electrons on the dot. (b) Illustrates the shape of a Coulomb blockade peak for electron tunneling through a single quantum state (equation 2.8).

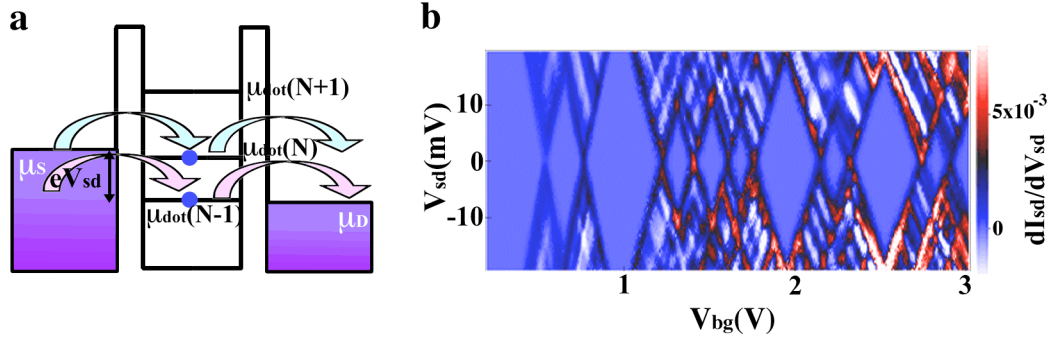


**Figure 2.5:** Conductance through a single quantum dot with finite  $V_{sd}$ . (a) Energy profile of a quantum dot coupled to the source and drain. Two levels fall within the source-drain bias window  $eV_{sd}$  opening two channels for conductance. (b) Coulomb blockade diamond plot from Bleszynski (2006) of a short quantum dot ( $L_{dot} = 18$  nm and  $d_{NW} = 50$  nm) defined in an InAs/InP heterostructure nanowire. The differential conductance  $dI_{sd}/dV_{sd}$  is plotted vs.  $V_{sd}$  and  $V_{bg}$ . The solid lighter blue diamonds correspond to voltages where conductance through the quantum dot is blocked. At zero  $V_{sd}$  the diamond vertices correspond to the Coulomb blockade peaks. At higher  $V_{sd}$  the lines running parallel to the diamond edge are electronic tunneling through excited states. The variation in size of the Coulomb diamonds indicates a difference in the single particle energy spacing of states and in the energy spectrum of the dot.

In addition to applying  $V_{bg}$  to lift the Coulomb blockade, a finite source-drain bias  $V_{sd}$  can be applied to permit electron tunneling. In figure 2.5(a) the source-drain bias window is increased to allow tunneling through excited states. Figure 2.5(b) shows a Coulomb blockade diamond plot of a quantum dot, where the differential conductance  $dI_{sd}/dV_{sd}$  is plotted vs.  $V_{bg}$  and  $V_{sd}$  [Bleszynski-Jayich *et al.* 2008]. The Coulomb blockade diamonds of zero conductance mark the voltages at which the chemical potential  $\mu_{dot}$  of the dot is not within the source-drain bias window. For the dot in figure 2.5(b),  $E_i$  is comparable to  $E_c$ , and the size of the Coulomb blockade diamonds varies with electron number due to the differences in addition energy  $E_{add}$  (equation 2.5). The change in  $E_{add}$  with electron number provides energy level spectroscopy of the ground

states of the quantum dot. Due to the small size of the dot in figure 2.5(b) the size of each diamond is not constant which indicates the atomic-like shell structure of the quantum dot [Tarucha *et al.* 1996]. In figure 2.5(b) tunneling through excited states can be seen at higher  $V_{sd}$  by the lines of increased differential conductance  $dI_{sd}/dV_{sd}$  parallel to the diamond edges. Parameters of the system such as capacitances and charging energy can be found from the diamond characteristics [Kouwenhoven *et al.* 2001].

## 2.4 Coulomb blockade imaging technique

The conducting SGM tip is utilized as a movable local gate to manipulate and probe electrons on the quantum dot. The general experimental setup is illustrated in figure 2.6. The tip is raster scanned in a plane at a specified constant height  $H_{tip}$  above the nanowire, and a constant voltage  $V_{tip}$  is applied to the tip with respect to the nanowire. The conductance  $G$  through the nanowire is mapped vs. the tip position  $x_{tip}$  and  $y_{tip}$ . The SGM has been used to image the flow of electrons through 2DEGs using the tip as a backscatterer or an adjustable strength scatterer [Tessmer *et al.* 1998; Topinka *et al.* 2001a; Topinka *et al.* 2001b; Aidala *et al.* 2006; Jura *et al.* 2007; Berezovsky *et al.* 2010a; Berezovsky *et al.* 2010b]. The SGM tip has also served as a movable gate to control and image electrons in low-dimensional systems [Woodside *et al.* 2002; Fallahi *et al.* 2005; Bleszynski *et al.* 2007; Gildemeister *et al.* 2007; Bleszynski-Jayich *et al.* 2008; Schnez *et al.* 2010]. For the experiments where the tip acts as a movable gate the

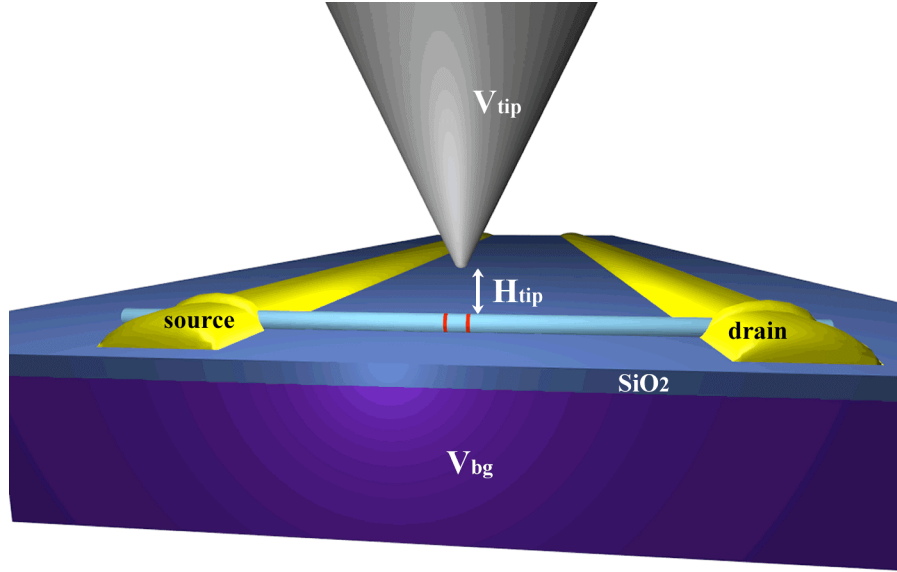


**Figure 2.6:** Illustration of the experimental setup for the Coulomb blockade imaging technique. The nanowire is deposited and contacted on a degenerately n-doped Si substrate with a SiO<sub>2</sub> layer on the top. A backgate voltage  $V_{bg}$  with respect to the nanowire can be applied to the underside of the substrate. A conducting tip with radius  $R_{tip}$  is raster scanned above the nanowire at a set constant height  $H_{tip}$ , and a constant voltage  $V_{tip}$  is applied to the SGM tip relative to the nanowire.

imaging mechanism as the tip is scanned is the change in capacitive coupling between the tip and the sample.<sup>2</sup>

The charged SGM tip performs gating functions analogous to the backgate, such as energy level spectroscopy and manipulating the electronic state of the quantum dot as demonstrated in section 2.2. The charge  $Q$  induced on the dot by the tip is given by:

$$Q = C_{d-t}V_{tip} \quad (2.9)$$

where  $C_{d-t}$  is the capacitance between the quantum dot and the tip. The induced charge  $Q$  is controlled either by varying  $V_{tip}$  or by varying  $C_{d-t}$  by changing the distance between

---

<sup>2</sup> In our SGM there is no current flowing between the tip and the sample.

the tip and the dot. Changing either  $V_{tip}$  or the tip position  $x_{tip}$  and  $y_{tip}$  controls the local gating strength of the tip. The backgate is a universal gate to the device, while the tip locally gates all or part of the device. Two independent gates open the possibility to manipulate multiple dots.

Altering either the tip position  $x_{tip}$  and  $y_{tip}$  or the tip voltage  $V_{tip}$  shifts the chemical potential  $\mu_{dot}$  and changes the conductance  $G$  through the dot. Figure 2.7 schematically represents the change in  $G$  as the tip is scanned above the dot with a constant negative  $V_{tip}$ . In figure 2.7(a) the tip is to the left of the dot's center and the current is blocked, because  $\mu_{dot}$  is out of resonance with the leads. When the negatively charged tip is moved closer to the dot, figure 2.7(b),  $\mu_{dot}$  is shifted into resonance with the source and the drain and current flows. When the tip moves closer and gates the dot more strongly, figure 2.7(c),  $\mu_{dot}$  is shifted further upward and conductance is blocked again. Likewise, moving the tip the same distance away, but to the other side of the dot, has the same effect, figure 2.7(d)-(e). Figure 2.7(f) illustrates a line plot of the conductance through the nanowire vs. the positions of the tip from figure 2.7(a)-(e). When the 1D scan is translated into scanning the tip in a plane above the nanowire, an image similar to figure 2.7(g) is obtained [Bleszynski-Jayich *et al.* 2008]. The blue regions of zero conductance in figure 2.7(g) indicate that for those tip locations the conductance through the nanowire is blocked and the number of electrons on the dot is fixed. A Coulomb blockade peak creates the contrast for the greenish ring, a Coulomb blockade conductance ring of high conductance, which corresponds to a region of

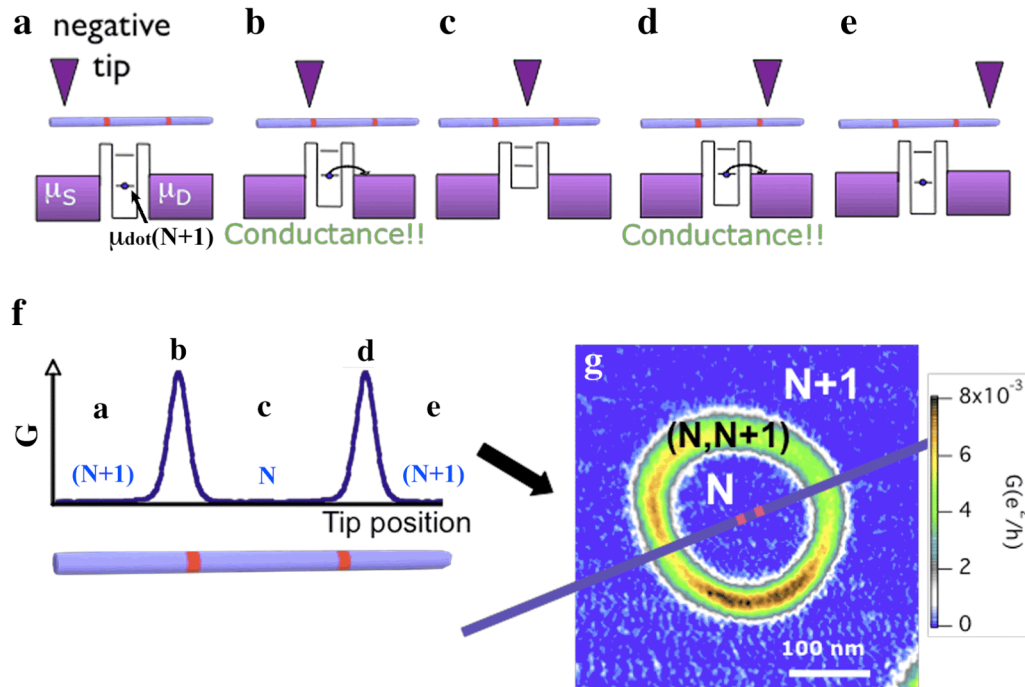


**Figure 2.7:** Schematic of the Coulomb blockade imaging technique for zero  $V_{sd}$ . (a)-(e) Changing the distance between a negatively charged SPM tip and a quantum dot manipulates the charge on the dot by controlling the strength of the tip-to-dot coupling  $C_{t-d}$ . (a) The chemical potential of the dot  $\mu_{dot}$  is out of resonance with the source and the drain and conductance is blocked. (b) As the negative tip is moved closer to the dot, the tip gates the dot more strongly and raises the chemical potential of the dot into resonance so current may flow. (c) As the tip gates the dot even more strongly,  $\mu_{dot}$  is shifted even higher and conductance is blocked again. In (d) and (e) moving the tip the same distance away, but to the other side of the dot, has the same effect as in (a) and (b). (f) A plot of the conductance through the nanowire as the tip is scanned in a straight line along the length of the wire. (g) Translating the plot from a 1D scan to the image obtained when raster scanning over the wire in 2D produces images with Coulomb blockade conductance rings. The blue regions of zero conductance in (g) correspond to locations of the tip where conductance through the wire is blocked. As the tip moves relative to the dot,  $\mu_{dot}$  is brought into resonance with the source and the drain when the tip is above the area of the green and brown ring of high conductance. In this manner the charge on the dot is manipulated.

constant tip-to-dot coupling. When the tip is above the conductance ring, the energy state of  $N$  or  $N+1$  electrons on the dot is degenerate.

## 2.5 Multiple quantum dots

Understanding the electronic interactions of nanoscale semiconductor devices containing multiple quantum dots is of great interest for designing nanoelectronic circuits. Double dot systems have been extensively studied [van der Wiel *et al.* 2003 and references therein; Fuhrer *et al.* 2007] and higher order multi-dot systems have been investigated, such as single-electron rectifiers [Vidan *et al.* 2004; Stopa 2002]. Loss and DiVincenzo (1998) proposed that electron spin in quantum dots can act as qubits for quantum information processing. In the last few years, much work has been performed to investigate electron spin in single and multiple quantum dots, which is fundamental in building spintronics [Hanson *et al.* 2007].

Current will flow through a multi-dot system for dots in series only when the total energy of two different charge states is equal. The plot of the energy  $U$  of a single dot (figure 2.3(a)) can be modified to represent the inter-dot tunneling of two quantum dots in series, figure 2.8(a). In figure 2.8(a) the energy of the charge states  $(N,N)$ <sup>3</sup> and  $(N+1,N+1)$  are the two parabolas (purple and green) with lower energy. The polarized charge states  $(N, N+1)$  and  $(N+1,N)$  are represented by the light red dashed parabola that is higher in energy. If there is no coupling between the dots, current will flow only at the

---

<sup>3</sup>  $(n_1, n_2)$  signifies that there are  $n_1$  electrons on the left dot and  $n_2$  electrons on the right dot.

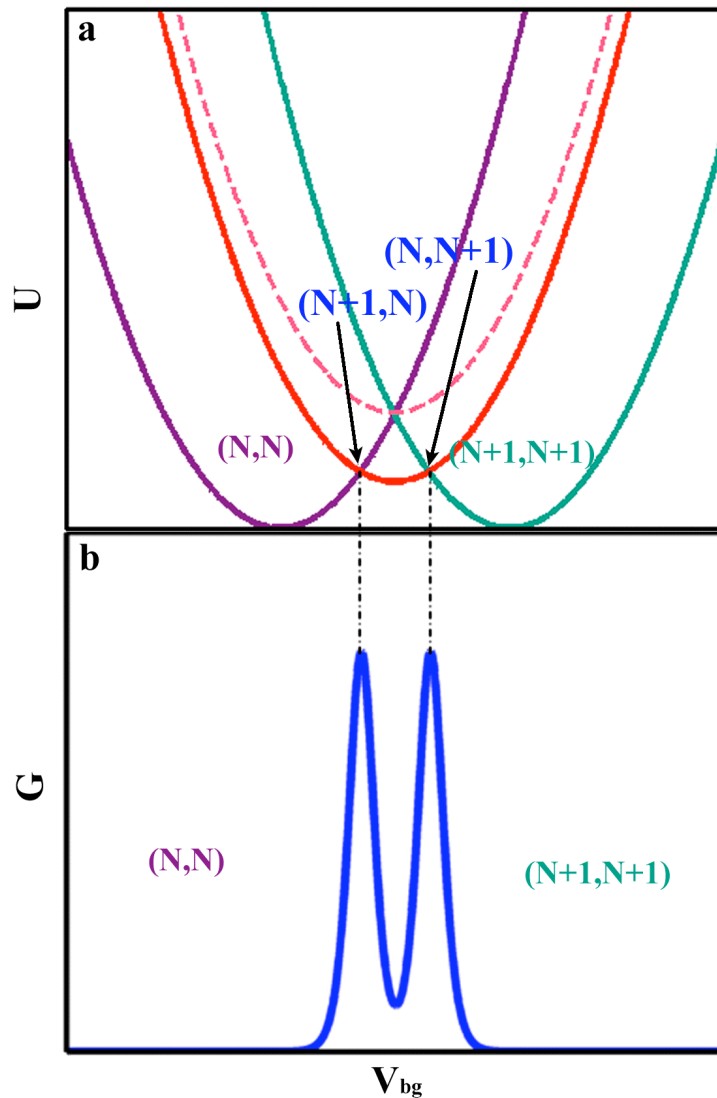


**Figure 2.8:** Coulomb blockade of a double quantum dot system with inter-dot tunneling where  $E_i$  is much smaller than  $E_c$ . (a) Plot of the energy  $U$  of the system vs.  $V_{bg}$ . The purple and green parabolas, which are at a lower energy, represent the charge states  $(N, N)$  and  $(N+1, N+1)$ , respectively. The polarized charge states  $(N, N+1)$  and  $(N+1, N)$  are higher in energy. If there is no coupling between the two dots, then the parabola for the polarized charge states is the light red dashed line and conductance can occur only at the triple point where all three parabolas intersect. If inter-dot tunneling is included, the parabola of the polarized charge states is shifted down and creates two intersection points. (b) Coulomb blockade conductance peaks for a double dot system with inter-dot tunneling. The shift to lower energy of the parabola for charge states  $(N, N+1)$  and  $(N+1, N)$  splits the single conductance peak in two.

triple-point where all three parabolas intersect. The triple-point corresponds to the condition when the chemical potential of all the dots are in resonance with the chemical potential of the source  $\mu_s$  and the drain  $\mu_d$ . When inter-dot tunneling is included the charge on each dot is no longer required to be quantized. By sharing electrons between the dots, the electrostatic energy of the system is reduced. With tunnel coupling included the solid red parabola for the charge states (N, N+1) and (N+1,N) in figure 2.8(a) is shifted down to reflect the lower energy of the multi-dot system when sharing of electrons is allowed. Figure 2.8(b) shows that shifting the parabolas creates two intersections, which translates the single Coulomb blockade conductance peak into two split peaks.

Livermore *et al.* (1996) demonstrated charge stability diagrams for a double dot system, figure 2.9 [Waugh *et al.* 1995; Blick *et al.* 1996]. The quantum dots were defined in a GaAs/AlGaAs 2DEG with metal top gates, and the tunnel coupling was varied using an electrostatic gate. Figure 2.9(a) shows the conductance through the system *vs.* the sidegate voltage of dot 1  $V_{g1}$  and dot 2  $V_{g2}$  for a double dot with weak tunnel coupling. Conductance occurs only at the triple-points where  $V_{g1}$  and  $V_{g2}$  bring the dots into resonance. As the tunnel coupling increases, figure 2.9 (b)-(e), the points split and spread apart until in figure 2.9(e) the coupling is so strong that one single dot is formed.

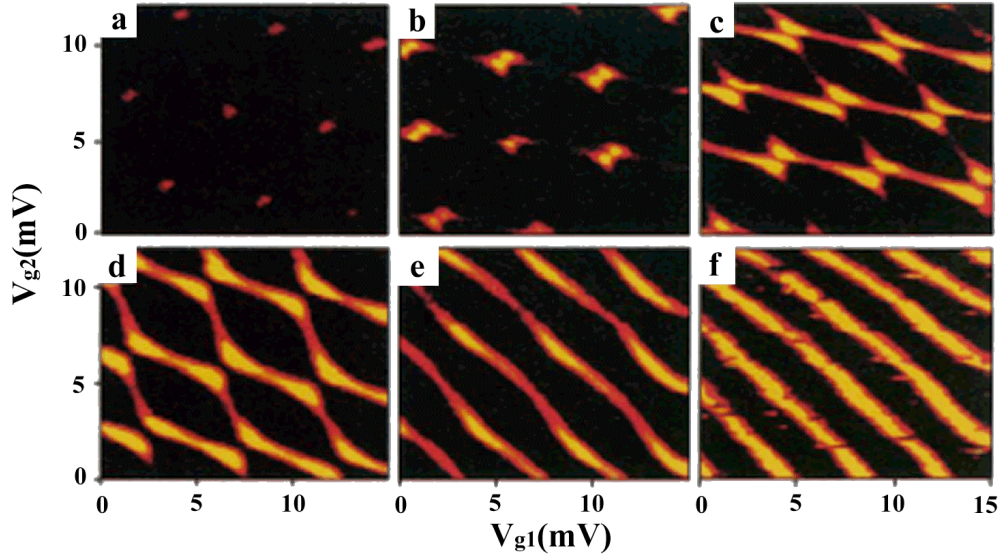


**Figure 2.9:** Charge stability diagrams as the inter-dot tunneling is increased of a double quantum dot defined in a 2DEG 57 nm below the surface by metal top gates on GaAs/AlGaAs [Livermore *et al.* 1996]. The charge stability diagram plots conductance  $G$  vs. the sidegate voltages of dot 1  $V_{g1}$  and dot 2  $V_{g2}$ . (a) With weak tunnel coupling between the dots conductance is only seen near the triple points. (b)-(e) As the tunnel coupling between the dots increases, the points from (a) split in two and spread out to form the classic honeycomb pattern. This corresponds in figure 2.8(a) to the red parabola being shifted to lower and lower energy. In (f) the array of straight lines shows that the inter-dot coupling is sufficiently strong that the two dots form one large single dot. The size of the lithographically defined opening of each dot was 500 nm x 800 nm.

The SGM tip enables the spatial tuning of the electronic states of a multi-dot system. Trodahl *et al.* (2009) calculated the spatial charge stability diagram of a double dot system with zero tunnel coupling in an InAs/InP heterostructure nanowire. In figure 2.10 the conductance through the wire is plotted vs. the tip position  $x_{tip}$  and  $y_{tip}$ . The series of white labels, for example (N,N), indicates the charge on each dot when the tip is above those regions. For zero capacitive coupling, current flows through the system only where the rings from the individual dots overlap (red conductance peaks). As the

capacitive coupling increases (the tunnel coupling remains zero in this model), the peaks of high conductance widen, split, and begin to move apart. At high capacitive coupling the regions of high conductance join to form a single set of conductance rings centered around a single large dot.

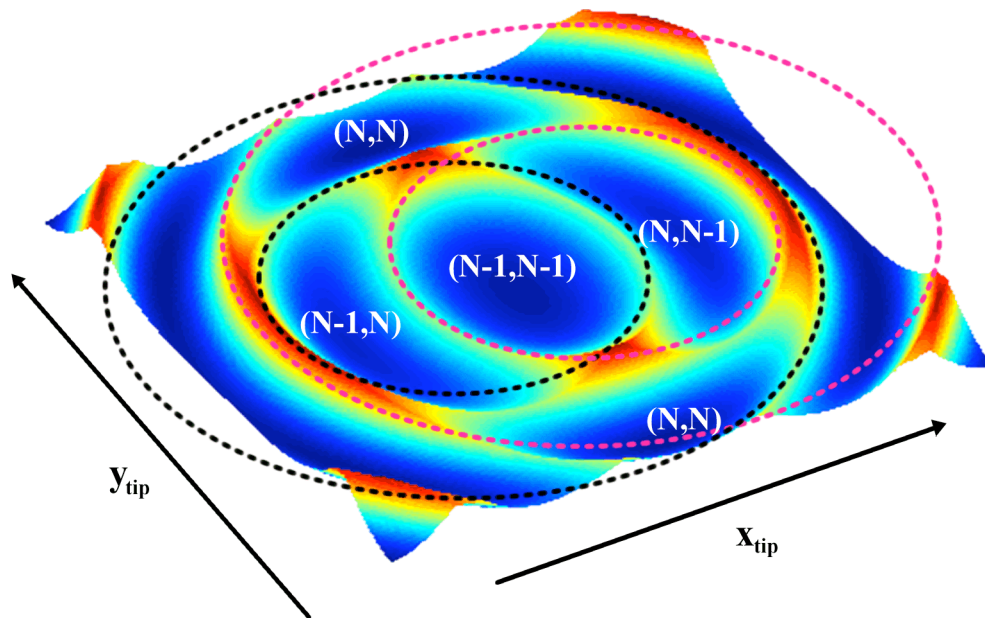


**Figure 2.10:** Spatial charge stability diagram of a double quantum dot in an InAs/InP heterostructure nanowire with weak capacitive coupling and no tunnel coupling [Trodahl *et al.* 2009]. The nanowire diameter is 50 nm, the dot lengths are 35 nm,  $T = 4.2$  K, and the tip is negatively charged. The black dashed lines correspond to the conductance rings from the left dot if the dot was isolated and the pink dashed lines correspond to the rings from the right dot. Current will only flow through the nanowire where the black and pink rings meet. The number of electrons on each dot is marked with the white label (left dot, right dot). As the capacitive coupling is increased (not shown) the red conductance peaks will split and move apart. At large values of capacitive coupling the peaks will form closed conductance rings corresponding to a single large dot.

# Chapter 3

## Experimental techniques

### 3.1 Sample fabrication

This section describes the detailed fabrication steps needed to produce nanowire samples to image in our scanning gate microscope (SGM) system. Previous work done by our group on nanowire samples [Bleszynski-Jayich *et al.* 2008] did not perform as much processing in-house as the work described in this thesis. The nanowires in this thesis were grown by Kristian Storm as part of a collaboration with Lars Samuelson's group at Lund University, Sweden. The post-growth processing took place in three stages, alternating between Harvard and Lund, to produce the final device. In section 3.1.1, we describe the nanowire growth. Section 3.1.2 covers preparation of the silicon wafer. In section 3.1.3 and section 3.1.4 respectively, the photolithography and electron beam lithography (EBL) are described. Section 3.1.5 outlines the procedure for depositing the nanowires. Finally, section 3.1.6 describes the process of electrically

contacting the nanowires, and section 3.1.7 illustrates the method we use to mount the sample to the sample holder.

### 3.1.1 Nanowire growth

InAs nanowires are epitaxially grown on InAs <111>B substrates using chemical beam epitaxy at Lund University [Jensen *et al.* 2004]. Size selected gold aerosol particles are chosen as growth catalysts to produce ultra-thin nanowires with diameter  $d_{NW} \sim 30$  nm and length  $l_{NW} \sim 2$  to 3  $\mu\text{m}$ . The nanowires contain an InAs quantum dot defined by InP tunnel barriers. InAs sections and InP barriers are grown by switching gas precursors during growth. The  $\sim 0.6$  eV conduction band offset between InAs and InP forms a potential well with strong electronic confinement. The figures 1.2 and 1.3 show, respectively, a sketch of the conduction band offset and a schematic of a contacted nanowire sample.

The InAs substrates with a forest of nanowires on the surface are usually sent to us via express mail from Lund (as seen in figure 1.1(b)). The InAs nanowires are quite sensitive to oxygen and should be immediately placed in the scroll vacuum pump when they arrive. The nanowires become even more sensitive after they have been electrically contacted. The next few series of steps take place at Harvard.

### **3.1.2 Si wafer preparation**

The sample size that fits in the SGM used for these experiments is quite small, between 2 mm x 3 mm and 3 mm x 4 mm. If the samples are much larger they are difficult to attach to the sample holder. In the past in the Westervelt group, all processing steps for fabricating each device were done separately for each small sample. I developed a fabrication process that utilizes batch processing for as many steps as possible, creating a more efficient system.

I begin with 2" degenerately doped n-type Si wafers that are coated in a 100 nm layer of thermal oxide.<sup>1</sup> In order to make a good electrical contact to the backgate, we remove the oxide on the backside of the wafer by etching only the back of the wafer with hydrogen fluoride (HF). One must ALWAYS use proper safety equipment and practices when dealing with HF as it is highly toxic and deadly. We first coat the top of the wafer with 950K poly(methyl methacrylate) (PMMA) in 5% anisole to protect the wafer. We use a plastic disposable mechanical pipette from the cleanroom to deposit HF on the backside of the wafer and to move the HF to cover the entire surface. The HF will not etch the Si, therefore when the HF starts to ball up on the surface it indicates that all of the SiO<sub>x</sub> has been etched. Then we use another pipette to remove the HF and then dunk and rinse the Si wafer in DI water and dry with nitrogen. We immediately take the Si wafer to the thermal evaporator and place it in vacuum to prevent oxide growth. We evaporate 10 nm of Cr and 40 nm of Au onto the backgate.

---

<sup>1</sup> Nova Electronic Materials, Ltd, 2833 Trinity Sq Dr. #173, Carrollton, TX 75006, (972) 478-7002

After the backgate is coated in Cr/Au, we clean the Si wafer using three solvents, Trichloroethylene (TCE), acetone, and methanol. The process is the same as found in a previous thesis [LeRoy 2003], except I have found it advantageous to do all the cleaning steps at Harvard's Laboratory for Integrated Science and Engineering (LISE) in the Center for Nanoscale Science (CNS) basement cleanroom instead of in the Westervelt sample prep room. Samples that are cleaned in the sample prep room acquire microscopic particles on the surface that cannot be removed. For this reason, I have taken to doing every step in the LISE cleanroom until the sample is ready for wirebonding.

### 3.1.3 Photolithography

I designed a Cr photolithography mask to write an array of 167 bonding pads and leads on a 2" wafer to make samples more quickly and efficiently, figure 3.1(a). In my design each element in the array is 2 mm x 3 mm, figure 3.1(b), which produces even smaller samples when cleaved, which require extensive experience to manipulate. An area for improvement in the future is to design a Cr mask with the identical bonding pads and leads, but with larger array elements (e.g. 2.75 mm x 3.75 mm) so that cleaved samples are approximately 2.5 mm x 3.5 mm.

#### *Spinning*

I prepare the Si wafer for photolithography by prebaking the wafer and then spinning a layer of Primer and then a layer of Shipley 1813 positive photoresist on the wafer. The spinner is set for a ramp up of 5 sec at 500 rpm and a spin time of 40 sec at

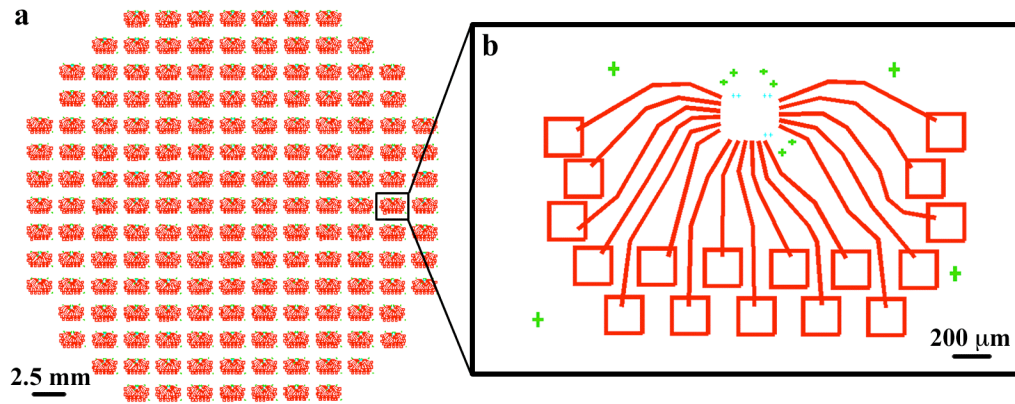


**Figure 3.1:** Photolithography mask design for bonding pads and large and medium alignment markers for nanowire samples. (a) The mask is designed with an array of 167 samples that will fit on a 2" Si wafer. (b) Zoomed-in image of a pattern for a single sample. Each sample is 2 mm x 3 mm.

5,000 rpm. No bake is needed between the Primer and the 1813. After spinning the 1813, I bake the wafer on a hot plate set to 117 °C for 3.5 min.

### *Writing*

Using the Suss MJB 4 mask aligner in the LISE cleanroom, I found an exposure of  $\sim 190 \text{ mWs/cm}^2$  produces the best write results. An exposure time between 4 sec - 4.5 sec was required for the values of the lamp intensity when I used the aligner. The important number to keep constant from write-to-write is the exposure, although I have found that the same exposure on different aligners gives different results. I then develop the wafer in CD26 developer for  $\sim 90$  sec and rinse in DI water. Until there is confidence that the development process is correct, it is essential to check the sample in the optical microscope after developing. If a film appears over the pattern, the sample is

most likely underexposed or underdeveloped. The sample can be developed in CD26 again to see if the film is removed.

### *Evaporation*

After development, the Si wafer is placed in oxygen plasma at a pressure of 120 mT and a power of 100 W for 30 sec to remove any vestiges of organics from the pattern. I deposit 10 nm of Cr and 40 nm of Au using a thermal evaporator and then lift-off using acetone.

## **3.1.4 Electron beam lithography**

The next step in the device processing is to produce a number grid at the center of the leads to serve as reference points for the location of nanowires and as fine alignment markers, figure 3.2. Photolithography does not have high enough resolution to write the lines that define the numbers (0.15  $\mu\text{m}$ ), so we must use electron beam lithography (EBL) to individually write each number grid. The most efficient method of writing the individual grids is to cut the 2" wafer into 4 approximately even pieces using the cleaving machine or the dicing saw. Before doing any cleaving or dicing the sample must always be coated in a layer of PMMA to prevent dirt from sticking. Each fourth of the wafer will have approximately 30 to 40 sets of bonding pads. Usually the sample will need to be cleaned after being cut and then respun for the EBL. I use a single layer of 950K PMMA in 5% anisole that is spun in two steps: 5 sec at 100 rpm/sec at 500 rpm

and 50 sec at 1,000 rpm/sec at 5,000rpm, and then the sample is baked for 2 min at 180 °C.

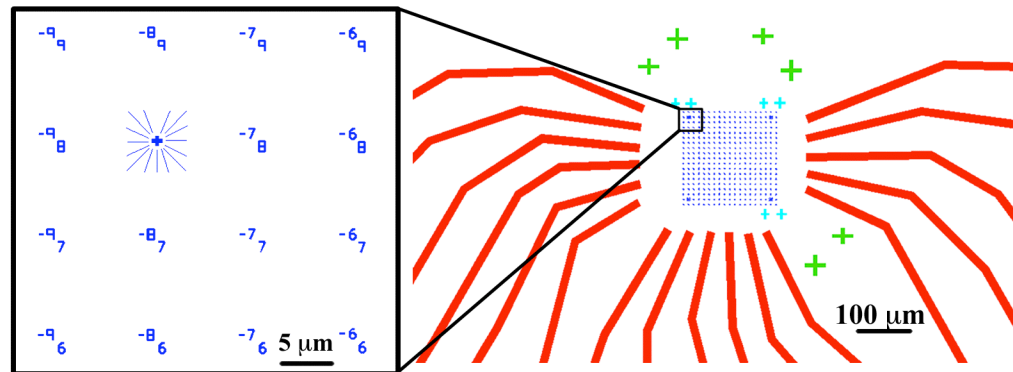


**Figure 3.2:** The number grid (blue) is written using electron beam lithography (EBL). The number grid provides Cartesian coordinates to serve as reference points of the nanowires' locations.

Figure 3.3(a) shows the JOEL-7000 EBL, which was used for all the EBL steps for sample fabrication. To hold the sample to the EBL stage, I apply a dab of carbon paint to either side of the wafer, figure 3.3(b). In one session all the number grids for one quarter of a 2" wafer are written. Starting with a set of bonding pads in one corner of the wafer, I perform the alignment for the large and medium alignment markers and write the number grid. The electron beam is kept blanking and is moved to the next array. I quickly perform the alignment, write the pattern, and move to the next array, continuing this process until number grids are written for all the arrays. After writing the grid and developing, the sample is exposed to oxygen plasma at 100 mT at 27 W for 30 sec. The thermal evaporator is used to deposit 7 nm of Cr and 18 nm of Au for the grid. Note: We usually try to keep the numbers as thin as possible to reduce stress on the SGM tip when

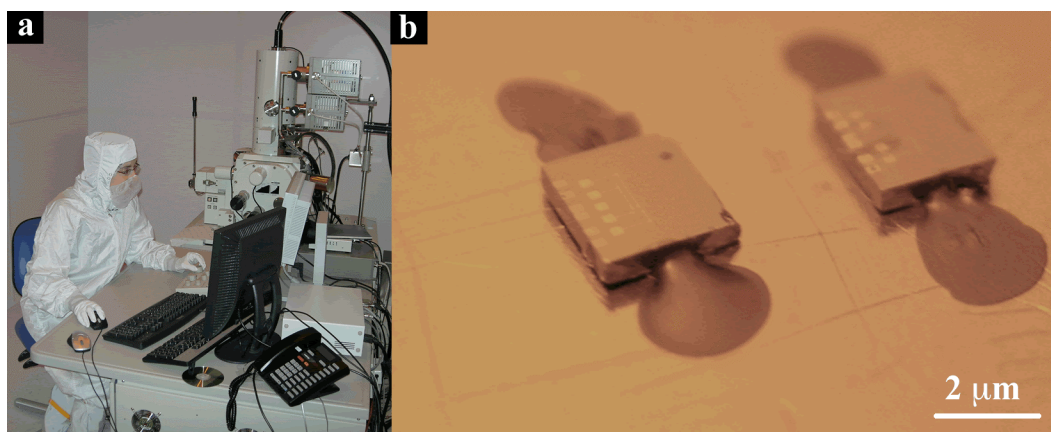


**Figure 3.3:** (a) Working at the JOEL-7000 EBL in the LISE cleanroom. (b) Shows how the carbon paint hugs the side of the sample to hold the sample on the EBL stage. The carbon paint is applied with the broken end of a wooden applicator.

scanning in topographical mode. However, a thickness of  $\sim 25$  nm is required to see the small alignment markers through the PPMA when writing the leads with the EBL.

After lift-off in acetone, I spin another layer of PMMA on the quarter of the wafer to protect the samples before using the cleaver or the dicing saw to cut out each individual sample. Approximately 30 samples are now ready to have nanowires deposited on them.

### 3.1.5 Nanowire deposition

The nanowires are deposited on the silicon substrate in one of the cleanroom fume hoods to prevent inhaling nanoparticles, since their effect on health is not well understood and could be detrimental. The instrument of choice for transferring the nanowires is a triangular piece of cleanroom wipe. To make the triangle, the wipe is cut along the grain of the paper. I hold the triangle with tweezers while cutting, so that it

does not touch the bench. Cutting along the grain helps to ensure that the triangle is clean with no small fibers at the end. I very lightly bring the side of the triangular tip to the forest of nanowires on the InAs wafer. A large number of nanowires become stuck to the cleanroom wipe. By gently touching the tip of the triangle to the number grid on the sample once or twice, nanowires are deposited on the grid. If the triangle repeatedly touches the grid, the wires that were deposited will be picked up again by the triangular tip and leave a mess of debris and broken wires on the grid.

In order to see how accurately the tip came into contact with the grid and if there are enough wires on the grid, I take the sample to a non-inverting reflectance optical microscope, which I operate in dark field mode. Once the nanowires are deposited, they are firmly bonded to the surface due to van der Waals forces and inhalation is not a concern. I use the highest magnification on the optical microscope and the dark field mode to clearly see the position of the wires on the grid. It usually takes a few tries of transferring the wires to get approximately 12 wires (about the number that we can connect with our bond pads) that are not kinked, are not touching other wires, and are approximately the correct length. After the nanowires are deposited, the sample CANNOT be sonicated as this will remove the nanowires, but soaking the sample in acetone and methanol and blow drying with nitrogen is not a problem. Once there is a satisfactory number of nanowires on the grid, I use the camera in the optical microscope to record the exact location of the usable nanowires with respect to the number grid. These images are taken with the dark field on the highest magnification (150x).

### 3.1.6 Electrically contacting nanowires

Using the software Design CAD, I align the optical images of the nanowires and number grid to the grid pattern. Figure 3.4 shows the optical images (black with gold numbers) overlaid on the number grid and the green 300 nm wide leads I designed to contact the most promising wires. The distance between the source and drain contacts is usually between 0.8 to 2.0  $\mu\text{m}$ . Before using the EBL I spin a single layer of 950K PMMA in 5% anisole in two steps: 5 sec at 100 rpm/sec at 500 rpm and 50 sec at 1,000 rpm/sec at 5,000rpm, and bake the sample for 2 min at 180  $^{\circ}\text{C}$ .

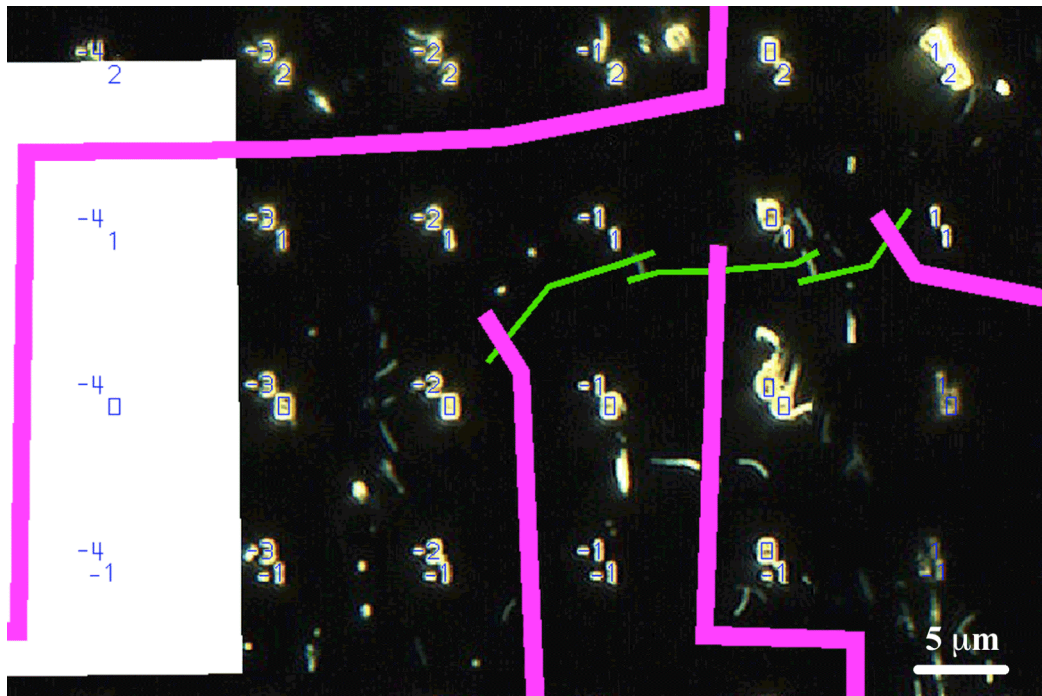


**Figure 3.4:** Shows optical microscope images (black with gold numbers) overlaid on the blue number grid design. The leads to the nanowires (pink and green) are designed to contact the most promising looking nanowires.

When writing the contacts to the nanowires, it is important to ensure there is minimal drift of the electron beam before starting to write. Before finding the EBL offsets for different currents and magnifications, I wait until the drift is at most 100 nm in 30 sec. I use the small current (at least 20 pA) on the EBL for the layers requiring the finest precision. The smaller the drift and the quicker the pattern writes, the more accurate the contacts will be with respect to the nanowires.

The next step is passivating the exposed regions of the nanowires and evaporating metal contacts. In order to remove the oxide on the InAs wires, so a high quality electrical contact can be made, the samples are dipped in an ammonium sulfide solution. The solution is made by mixing 1 part commercial Ammonium Poly-Sulfide solution 20-25% with 9 parts water and adding 15 mol/L of sulfur powder. The ammonium etches away the oxide, and the sulfur bonds to the sites the oxygen usually occupies. This gives a few minutes to transfer the sample to the vacuum chamber of the thermal evaporator.

The passivization and evaporation are performed at Lund. We have extensively experimented with performing the passivization step in the Harvard cleanroom using the same concentration ammonium sulfide solution with very poor yield of even low quality electrical contacts. I have traveled to Lund and observed their process of passivization and an expert in passivization from Lund has come to Harvard and watched my process. Both processes seem identical, but the passivization done in Lund has a much higher yield. Therefore the nanowire samples in this thesis were shipped to Lund after the EBL step. In Lund the nanowire samples are passivated using the ammonium sulfide solution

and immediately transferred to a thermal evaporator where 20 nm of Ni and 70 nm of Au are deposited for the contacts. After lift-off the samples are sent back to Harvard.

I have found that holders from Gel-Pak are the best way to ship the samples. The very small samples can be quite hard to remove from carbon tape, and the carbon tape leaves a thick residue on the backside of the sample, which must be cleaned. The Gel carriers firmly hold the sample in place for the transatlantic journey, but then samples can be easily lifted out of the carriers with tweezers. After the passivation it is essential to limit the samples' contact with air as much as possible. At both Harvard and Lund we have commercial food-storage-bag vacuum sealers that are used to seal the sample carriers in vacuum before shipping. When samples arrive at their destination, they are immediately placed in a scroll vacuum pump chamber.

### **3.1.7 Mounting sample**

The first step when the nanowire samples arrive back at Harvard is to test their conductivity at room temperature using our probe station. If the nanowire does not conduct at room temperature, it usually does not conduct at liquid-He temperatures. However, just because a nanowire conducts at room temperature, this does not guarantee conductance at liquid-He temperatures. When testing the nanowires' conductance at room temperature using the Westervelt probe station, I have found that nanowires with resistances greater than 10 M $\Omega$ , when 20 mV is applied across the source and the drain, do not exhibit the Coulomb blockade effect at liquid-He temperatures. Nanowires with resistances between 0.5 to 10 M $\Omega$  usually exhibit Coulomb blockade peaks at cold

temperatures. In the 0.5 to 10 M $\Omega$  range, a larger resistance usually means a slightly thinner wire, which for my case was favorable. (There is a small variance in diameter of the gold aerosol catalyst particles, which translates to the diameter of the nanowires.) I also found that the measured resistance of a given nanowire decreases when the bonding pad to the nanowire is contacted with a wirebond versus a probe station tip due to the higher quality contact.

In the current design there are 17 bond pads on the sample and only 12 pads on the sample holder. By testing the samples at room temperature before wirebonding, we can contact the most promising nanowires. Once the nanowires to contact have been selected, I take the sample to the optical microscope in the cleanroom and use the camera to record the features around each wire. These optical images will be indispensable when doing topographical imaging with the SGM to locate a device.

While still in the cleanroom, I mount the sample on a green PCB sample holder, which goes in the SGM, figure 3.5. In order to contact the backgate on the sample, I first use silver paint to adhere a piece of aluminum foil that is slightly larger than the sample to the PCB board sample holder. Once the silver paint dries, I use more silver paint to adhere the sample to the foil, so that the foil is connected to the backgate, as seen in figure 3.5.

Before wirebonding ensure that the user is grounded and all the leads to the sample holder are properly grounded. The wirebonder is located outside of the cleanroom. To contact the backgate, I wirebond from a sample holder pad to the foil, figure 3.5. To transport the sample once all wires' bonding pads are connected, I place

the sample in a small box covered in foil, un-ground the the sample, and place a foil lid on the box. This creates a Faraday cage to protect the sample from electric shock during transportation. The sample holder is now ready to mount on the microscope and prepare for imaging.

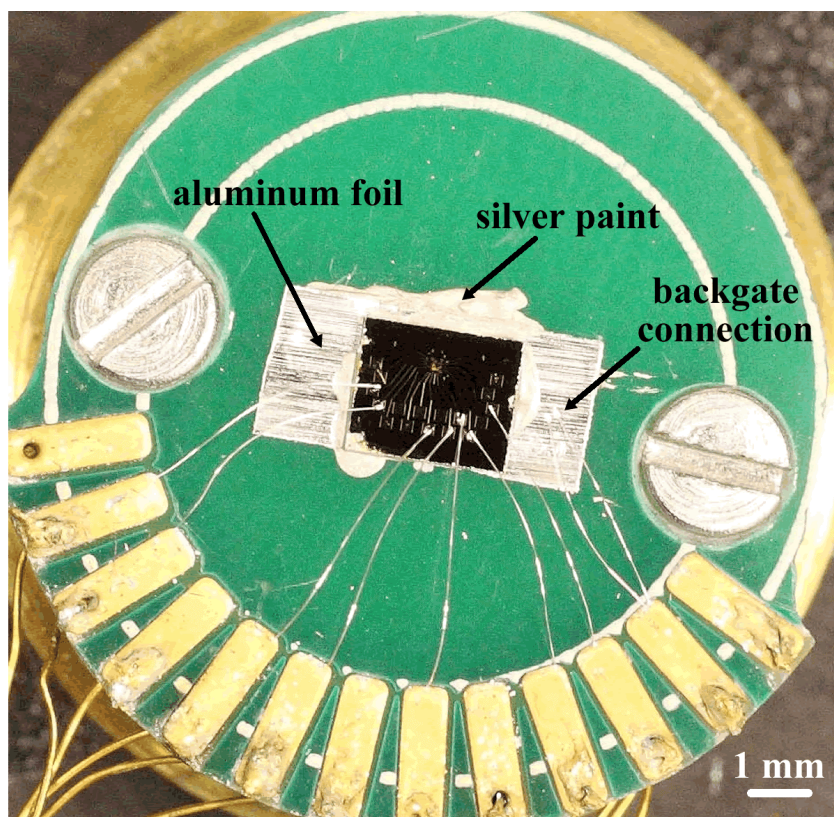


**Figure 3.5:** Shows the green PCB sample holder with gold bonding pads. The bonding pads on the holder are connected to the bonding pads on the sample with Al wirebonds. In order to mount the sample a piece of aluminum foil is first adhered to the sample holder with silver paint. The foil is longer than the sample so that there is leftover foil on the edges, but the foil does not touch the screws. The sample is then adhered to the aluminum foil with silver paint. This electrically connects the backgate to the aluminum foil. To contact the backgate a wirebond is made between the foil and a sample holder bonding pad.

## **3.2 Low-temperature scanning gate microscopy**

The microscope that I used for this work is the SGM built by a former Westervelt graduate student, Kathy Aidala. See her thesis for a comprehensive explanation of all aspects of the electronics and mechanical features [Aidala 2006]. Here I will give an overview of the SGM's design and operation and will explain in detail the modifications that have been made since the writing of Aidala's thesis. While the SGM has a 7 T magnet that generates a perpendicular magnetic field and the capability of cooling to He-3 temperatures, all my experiments were run at He-4 temperatures, either 4.2 K or 1.7 K (if the He was pumped on), with no applied magnetic field. In section 3.2.1, I discuss the microscope's design and mechanical components. Section 3.2.2 describes the electrical circuits that control the SGM, and section 3.2.3 outlines the procedure for taking conductance images at low temperatures.

### **3.2.1 Scanning gate microscope - mechanical**

There are two main components of the SGM: the cage and the head. The cage is a brass cylindrical case that houses the piezotube with the sample mounted on top, figure 3.6(a); the head holds the cantilever in place and provides the mechanisms for coarse and fine positioning at room temperature, figure 3.6(b). The head rests on three set screws and three springs are used to hold the head in place, figure 3.6(c). The set screws on either side of the cantilever are used to ensure that the cantilever is tilted slightly downward toward the sample, so the tip will be the first part of the cantilever to come

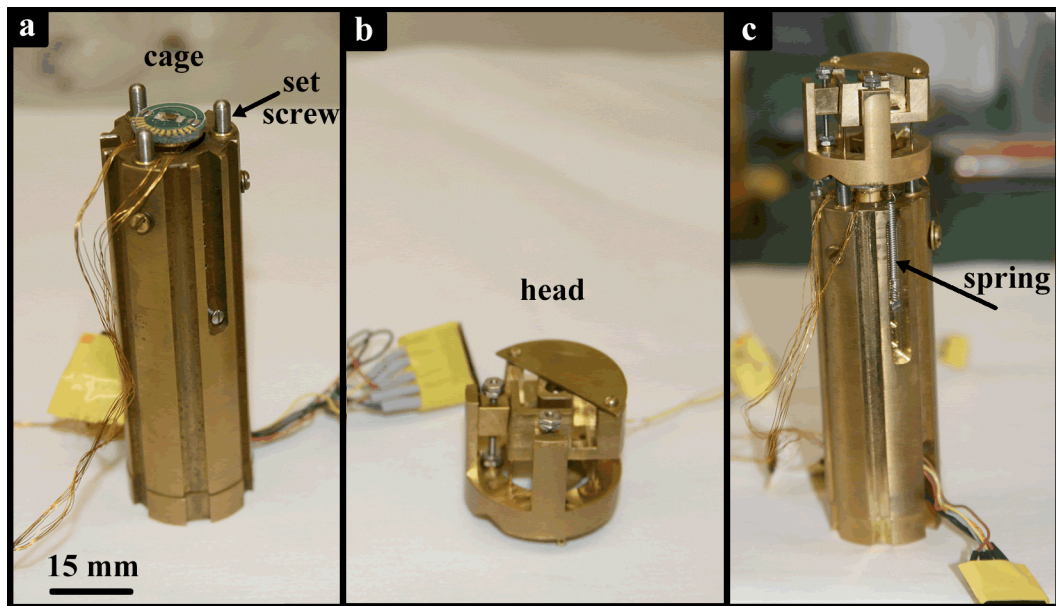


**Figure 3.6:** The SGM (a) Shows the brass cage which houses the 3" piezotube that provides the motion for scanning. The sample holder is screwed to the top of the piezotube. (b) Shows the head portion of the microscope. The tip and the mechanisms for coarse and fine positioning at room temperature are located in the head. (c) Shows the assembled microscope. The head rests on the three set screws on the top of the cage and is held in place by three springs.

into contact with the sample. The set screw in the front of the cantilever connects to the mechanical z feedthrough which changes the height of the tip.

The cage is the same design as in Aidala's thesis [Aidala 2006]. The sample holder is screwed into the top of the piezotube with the ground shield in-between and then the head and cage are assembled using the three springs. Care should be taken to never stress the piezotube mechanically or electrically as it is very fragile. For example, the sample holder must be screwed down lightly and the cage must be set down gently.

The head has undergone design changes to significantly improve both the coarse and fine positioning of the SGM tip at room temperature. I first designed the new coarse

positioning mechanism for the older IR dewar microscope [Topinka 2001]. Jesse Berezovsky, who was a post-doctoral fellow in the Westervelt lab, used the same ideas to design the coarse positioning for this microscope. The brass piece that holds the tip, the “slider”, rests on the upper portion of the fine positioning stage, which is connected by three thin phosphor bronze wires to the lower portion of the positioning stage, figure 3.7(a). The slider rests on the upper portion of the fine positioning stage and is secured using a thin brass sheet with two screws to clamp the slider in place, figure 3.7(a). Instead of gluing the cantilever chip to a macor piece, it is held in place by a piece of brass that can be screwed in to wedge the chip in place, figure 3.7(b). This facilitates easily and quickly replacing the tip compared to the older design. Figure 3.7(c) shows the cantilever chip from a view looking down into the head. To perform the coarse positioning, we view the microscope straight from the top with the stereoscope. The sample and the tip will be in view. We loosen the two screws in the clamp just enough so that we can firmly tap the slider with a small screwdriver, or similar tool, until the tip is close to the device to measure. The lateral drift of the tip over the sample upon cool-down must also be taken into consideration. Keeping a finger on top of the clamp and lightly applying downward pressure while moving the slider prevents the tip from tilting forward and into the sample. If the tip is within 200 to 300  $\mu\text{m}$  of the device, then it should be sufficient to reach the device using the fine positioning.

The fine positioning offers control of the tip position to within 2 to 3  $\mu\text{m}$ , which is a huge improvement over the previous design. The mechanism for the fine positioning was designed by Jesse Berezovsky. The three thin phosphor bronze wires that connect

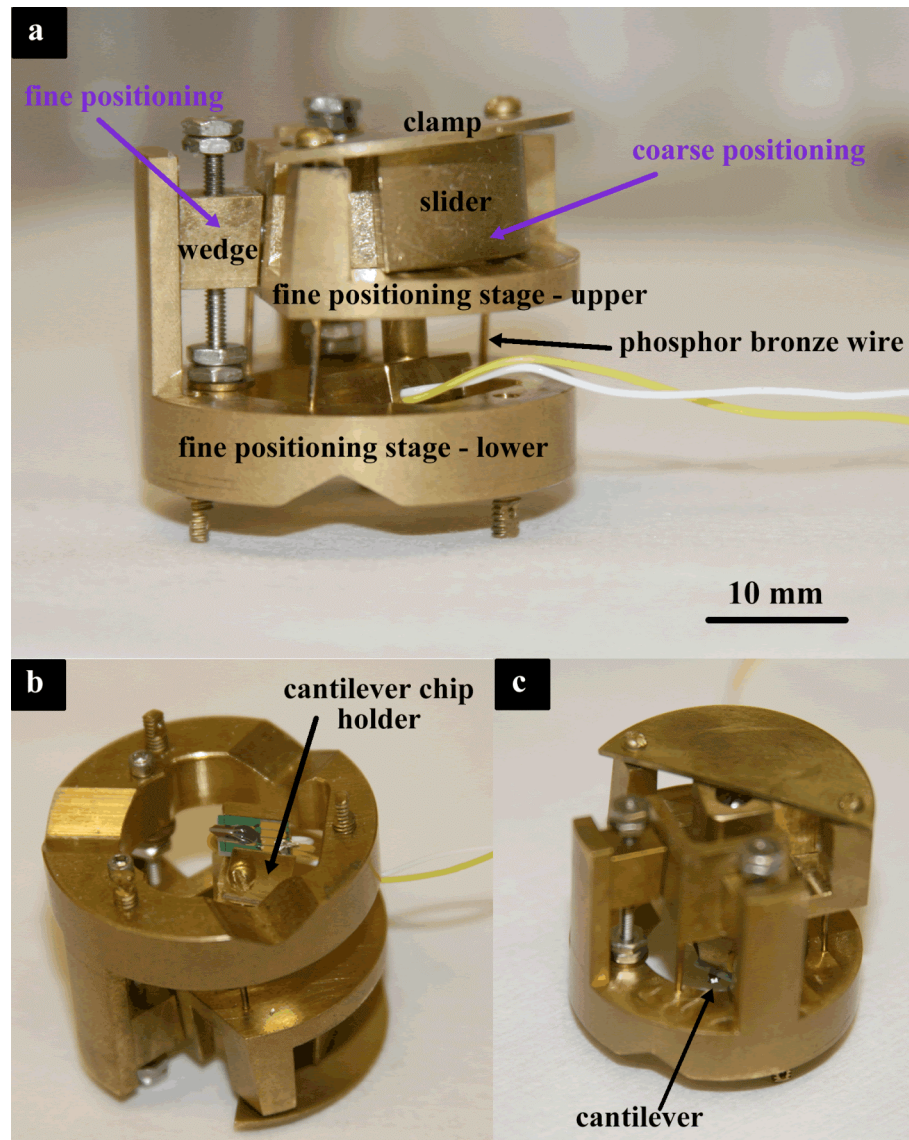


**Figure 3.7:** A close-up view of the head with the fine and coarse positioning. (a) To perform coarse positioning the clamp is loosened so the slider (to which the tip is connected) can be nudged over the number grid. The fine positioning is controlled by the stainless steel screws that move the wedge up and down. The wedge pushes into the upper fine positioning stage and moves the slider with great precision with respect to the lower fine positioning stage and the cage. The three phosphor bronze wires serve as very stiff springs to allow controlled movement between the upper and lower fine positioning stages. (b) Shows the underside of the head. The cantilever chip is held in place by the thin piece of brass that is screwed up against the cantilever chip to box the chip in place. (c) A top view of the head: looking down through the head, the cantilever is seen.

the upper and lower portions of the fine positioning stage act as very tight springs. While the slider remains clamped in place, pushing on the upper portion of the fine positioning stage causes the phosphor bronze wires to bend very slightly moving the slider by a few microns. There are two wedges that control how hard the screws push into the tip holder, figure 3.7(a). The wedges are perpendicular, so that by adjusting both wedges the tip can be made to move in any direction. One full turn of the screws connected to the wedges moves the tip by approximately 30  $\mu\text{m}$ . To get the best view of how close the tip is to the sample and a precise location when performing the fine positioning, we place the SGM under a long working distance binocular optical microscope as seen in figure 3.8. We adjust the tip position until it appears the tip is over the location needed to drift to the device. The closer the tip is, the less time it will take to do the alignment when scanning. Figure 3.9(a) shows the sample attached to the dunker stick and the electrical connections made (see section 2.2. for the electrical circuits). The sample should remain grounded as much as possible to avoid shocking the devices.

The final alignment step before closing up the microscope is to scan with the SGM in atomic force microscope (AFM) mode. A coarse approach rod with a hex key on the end is fed through the top of the dunker stick, down the length of the stick, and into the cage and set screw. This mechanical feedthrough changes the height of the tip at both room and cold temperatures. The coarse approach rod rotation is downscaled using a 1 to 16 gear conversion, which gives very fine control of the z positioning. From a topographical scan, we find how far way the ideal location is, come off the surface, and then with the microscope still connected to the stick adjust the fine positioning screws to



**Figure 3.8:** Setup to perform fine positioning of the tip over the device of interest. By viewing the tip and the sample on an angle, the tip's reflection is easier to see as the tip approaches the sample. A clear view of the tip's reflection makes it easier to tell when the tip is near the sample and to more accurately discern the lateral position of the tip over the number grid.

move to the ideal spot. We continue this process until the tip is over the correct location, so that when cooling down the drift will bring the tip over the device of interest. The excess wires around the microscope are tied against the stick, figure 3.9(b). Additionally, there is now a short metal tube that is placed over the microscope to prevent the wires from being bumped when lowered into the insert, figure 3.9(c). This tube has greatly improved the stability of the tip when cooling down. It is a wise idea at all steps in this

process to rerun a topographical scan to ensure that the tip has not been bumped out of range of the device before cooling down.

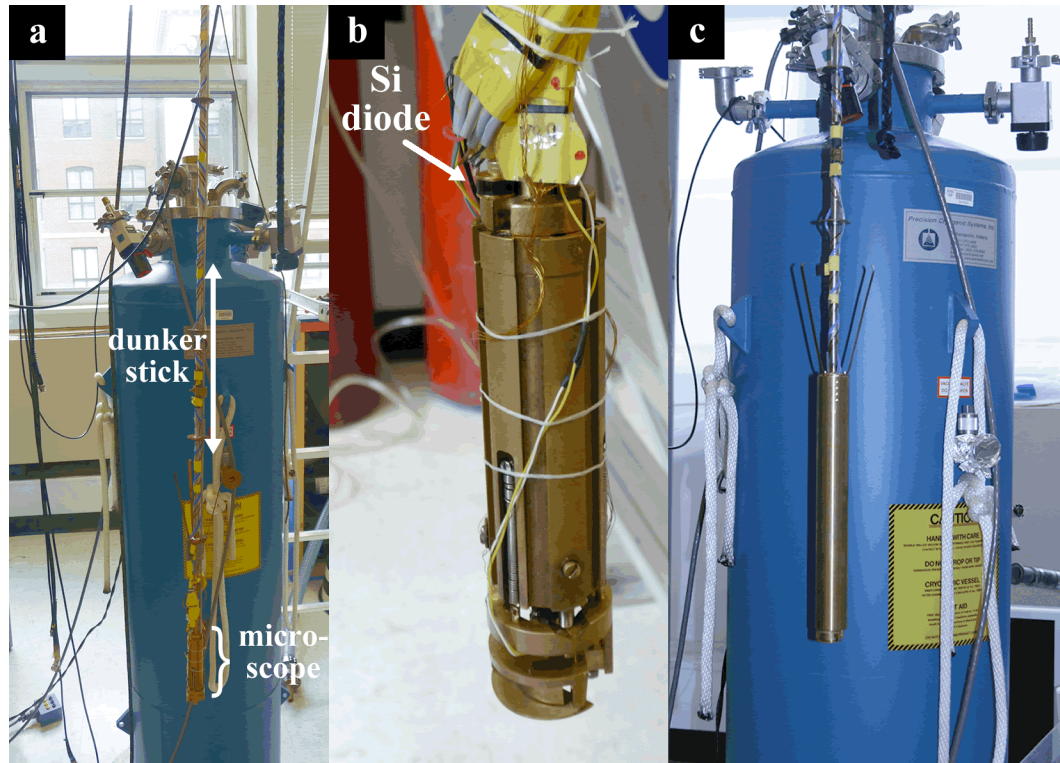


**Figure 3.9:** (a) Microscope attached to the dunker stick. (b) The wires for the electrical connections are held against the stick with dental floss to prevent the wires from becoming stuck or pulling when the metal cylinder is pulled over the cage. (c) The metal cylinder covers the microscope cage and the wires, so when the stick is placed in the insert there are fewer components to bump, which improves the tip's stability.

The final major change that has been made to the system is the insert that is used to cool down the microscope and stick. Previously, for He-4 temperatures an insert with an open bottom was placed around the stick and placed directly in the liquid He-4 bath in the blue Precision Cryogenics dewar. The sample was submersed in liquid-He, which resulted in some samples being speckled with debris after one cool-down. Now, the stick

is placed in a vacuum tight insert, which is pumped out and then filled with 3 mbar of He exchange gas. The He atoms are the thermal conductor that couples the sample and the liquid-He, allowing the sample to cool down and remain clean. Additionally, we have found that the drift of the piezotube is more consistent when the microscope is cooled down and warmed up slowly. The average time for cool-down is 6-7 hours. We first place the vacuum tight insert into the top of the dewar and wait 1.5 to 2 hours before beginning to lower the microscope a few inches at a time. When the drift of the cantilever signal and the temperature readout begin to stabilize (the temperature is still decreasing, but not as quickly), we lower the microscope a few inches farther into the dewar and repeat the process until the microscope is completely lowered. In addition to the thermal drift of the piezotube in x and y, the z drift must also be accounted for. By coming 90 half turns off the surface before cooling down, the z-direction thermal drift of the piezotube will not crash the tip.

### **3.2.2 Scanning gate microscope - electrical**

There are three sets of electrical feedthroughs to the microscope: the sample leads, the low voltages, and the high voltages. The sample lead voltages are provided by the digital-to-analog converter (DAC) to the blue 24-pin switcher box at the top of the dunker stick. Only 12 of these connections are wired down the length of the stick to the sample holder.

The cantilevers we use are piezoresistive cantilevers purchased from KLA Tencor, figure 3.10. I believe that KLA no longer produces these cantilevers, so when

our stockpile is depleted a new source must be found. At the end of the cantilever there is a tip and a resistor, which are electrically connected at room temperature to the four gold bonding pads. We wirebond the tip to the gold pads, figure 3.10, because the black blob in the middle of the chip breaks the electrical connection between the tip and the bonding pads at liquid-He temperatures. We do not use the resistor.

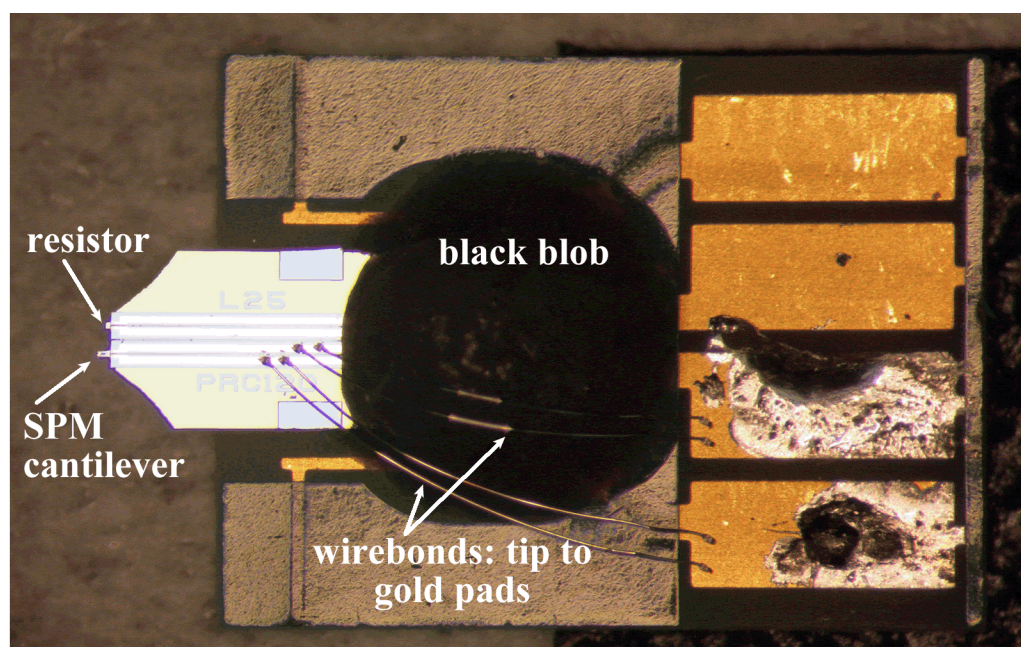


**Figure 3.10:** KLA Tencor piezoresistive cantilevers. The tip and a balance resistor are connected to the gold bonding pads at room temperature. The balance resistor on the chip is not used for the balance resistor in our circuit. At cold temperature the connections under the black blob are broken, and the tip must be wirebonded to the gold pads.

The low voltage circuits are for the temperature gauge and the cantilever. A LakeShore Model 211 Temperature Monitor is wired to a Lakeshore Si diode which is placed at the bottom of the microscope cage as seen in figure 3.9(b). The “cantilever circuit” is a Wheatstone bridge. Small changes in the resistance of the cantilever are

evident in the “cantilever signal,” which measures the deflection of the cantilever. For the Wheatstone bridge circuit’s balance resistor, we have found that matching the resistance of the tip using separate metal film resistors rather than using the resistor on the end of the cantilever produces more reliable results.

The high voltage circuit supplies the  $\pm x$ ,  $\pm y$ , and  $z$  voltages to the piezotube. The  $\pm x$  and  $\pm y$  voltages supply the relative motion of tip and sample when scanning. The  $z$  voltage causes the piezotube to either push-out or pull-back. The cantilever signal is used for feedback to specify the  $z$  voltage. In topographical scanning mode, when the piezoresistive cantilever hits a raised feature, the change in the cantilever’s resistance is feedback to the  $z$  voltage, causing the tube to change how much it is pushing-out or pulling-back. This in turn changes the cantilever’s deflection and the cycle continues.

### 3.2.3 Imaging procedure

After the sample has been cooled down, I recommend electrically testing the sample before scanning. I have experienced samples dying when cooling down without the tip ever touching the wire. Grounding the blue dewar and the He dewar when filling has helped to reduce this problem. Another situation I have encountered is the nanowire samples not conducting at cold temperatures for applied voltages up to  $V_{sd} = 0.1$  V and  $V_{bg} = 6$  V, but conducting again when cycled to room temperature. The lack of Coulomb blockade conductance at cold temperatures is usually caused by an issue with the contacts, and it is best to move on to the next sample, since the wire will not work at cold temperatures regardless of how many times the temperature is cycled.

If the wire of interest is conducting once cooled down, we topographically scan over a small area of the sample to find our location on the number grid. The scan range at liquid-He temperatures is  $20\ \mu\text{m} \times 20\ \mu\text{m}$ , and I suggest initially scanning a  $3\ \mu\text{m} \times 3\ \mu\text{m}$  range to avoid damaging the nanowire by inadvertently scanning over any leads or the nanowire. If the nanowire is not within the scan range, we can add extra voltage to one side of the piezotube to increase the scan range by  $\sim 5\ \mu\text{m}$  in one direction.

Once the location of the nanowire is identified, we move to a flat area near the nanowire to fit the plane. The sample will have been mounted with a tilt on the nanometer scale. By running the “flatteninside” command, the software will find the equation of the plane of the sample tilt and use that information to adjust the z voltage on the piezotube to keep the tip at the constant height above the surface as indicated by the user. See appendix A for the steps involved with flattening the plane. Knowing the location of the wire both laterally and vertically, conductance images can be taken by scanning the tip at a constant height above the nanowire while mapping the conductance through the wire vs. the tip position  $x_{tip}$  and  $y_{tip}$ .

# Chapter 4

## Imaging the amplitude of the wavefunction of a quantum state

### 4.1 Overview

Investigating the electronic wavefunctions of confined systems will improve the understanding of nanoscale systems and will assist in designing and creating nano-devices. Scanning probe technologies provide spatial information concerning electron behavior in nanostructures. The Coulomb blockade imaging technique, as explained in Chapter 2, allows a scanning gate microscope (SGM) to probe electrons that are enclosed in a structure, such as a quantum dot. Scanning tunneling microscopy (STM) has been used to image the electron waves on the surface of a metal. Electron waves confined to an elliptical resonator on a copper surface were imaged using an STM [Heller *et al.* 1994; Manoharan *et al.* 2000]. An STM was used to measure the

wavefunction of electrons in a metallic single-walled carbon nanotube [Lemay 2001]. Additionally, the internal quantum phase of an eigenstate was mapped with an STM, using the topological property of isospectrality, for electrons in enclosed regions on a copper surface [Moon 2008]. While STM is used to investigate electrons on the surface, we propose a technique to image the wavefunction of electrons that are beneath the sample surface [Fallahi 2006]. Electrons that are buried in a solid present additional hurdles to overcome for imaging, but information on buried electrons is particularly desirable since the electrons in future nanoelectronics and sensors will be located beneath the surface.

Tarucha *et al.* (1996) demonstrated energy level spectroscopy for few-electron dots using measurements of Coulomb blockade transport through a quantum dot. Theoretical work discussed using energy level spectroscopy to measure the wavefunction in a quantum dot [Mendoza 2003] and a quantum well [Nogueira 1998]. The imaging technique we propose combines Coulomb blockade transport measurements with a weakly perturbing SGM tip to perform energy level spectroscopy and wavefunction extraction with the same system. To demonstrate the imaging method we consider an idealized non-interacting one-dimensional (1D) electron gas with electron spin 1/2 within an InAs nanowire with only one occupied radial subband. In this thesis, wavefunction extraction refers to the amplitude of the wavefunction  $|\Psi|^2$  (the charge density probability). The extraction method does not measure the phase of the wavefunction.

In this chapter, we theoretically demonstrate the viability of our proposed wavefunction extraction method. In section 4.2 the effectively 1D nanowire device that

is used to illustrate extracting the electronic wavefunction is explained. The imaging technique that we propose for extracting the wavefunction is modeled in section 4.3. Section 4.4 discusses the various factors that contribute to the quality of the resolution of the extracted wavefunction and section 4.5 describes the experimental setup and data analysis for the extraction technique.

## **4.2 Model**

To demonstrate the imaging technique, we consider extracting information about the electron wavefunction in a long InAs quantum dot that is defined by two tunnel barriers in an otherwise uniform InAs nanowire. The scanning probe setup is sketched in figure 4.1. A conducting tip, with radius of curvature  $R_{tip} = 20$  nm, is scanned along a straight line above the length of the nanowire at a constant height  $H_{tip}$ . A constant voltage  $V_{tip}$  is applied between the SGM tip and the nanowire, and a backgate voltage  $V_{bg}$  is applied to the bottom of the substrate with respect to the nanowire. To illustrate the imaging technique, we utilize a model of a 1D idealized electron gas, enabling the system's dependence on the directions perpendicular to the wire length to be neglected. This imaging technique is valuable when the features of the wavefunction are greater than the height of the tip above the electron gas and the tip radius  $R_{tip}$  [Topinka 2002]. Additionally, the voltage on the tip  $V_{tip}$  must be weak in order that the tip potential creates a small dent in the wavefunction without noticeably changing the shape of the wavefunction [Fallahi 2006]. Due to nanowires' small diameters, they are attractive

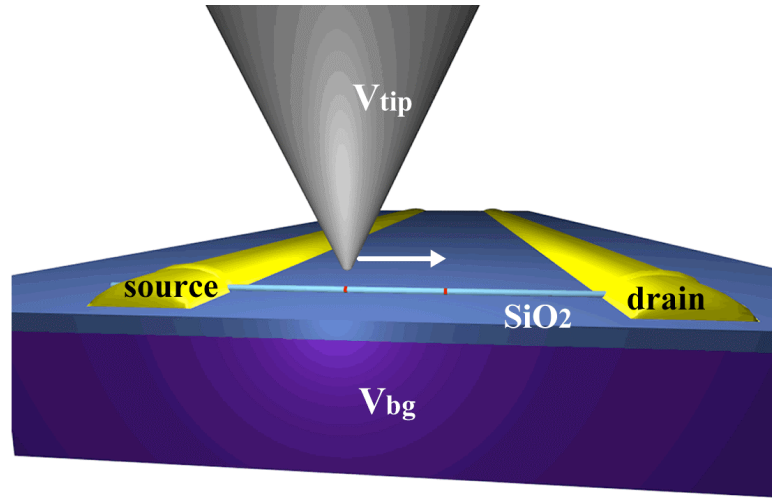


**Figure 4.1:** (a) Proposed experimental setup for extracting the electron's wavefunction. The charged SGM tip is scanned with a constant voltage  $V_{tip}$  with respect to the nanowire at a constant height  $H_{tip}$  in a straight line above the nanowire. The nanowire is deposited on a degenerately doped Si substrate that is topped with a  $\text{SiO}_2$  thermal oxide. A backgate voltage  $V_{bg}$  is applied to the underside of the Si substrate to manipulate the charge state of the dot. In this chapter, to demonstrate the extraction technique the quantum dot is approximated as a 1D quantum well with infinite sidewall potentials.

devices in which to image the electron wavefunction, because the tip can approach very close to the buried electrons. The proposed wavefunction extraction technique is also applicable for other electron gas systems.

A quantum dot with a large aspect ratio of length/diameter  $L_{dot}/d_{dot}$  increases the spatial separation of the features of  $|\Psi|^2$  for the lowest energy states and decreases the separation of the tip from the electrons, which increases the ease of imaging the wavefunction along the length of the nanowire. The width of the tip potential  $\Phi_{tip}$  must be less than or comparable to the width of the features in the amplitude of the wavefunction  $|\Psi|^2$ , in order to have sufficient resolution to image the wavefunction. All

the variables affecting imaging resolution will be discussed further in section 4.4. In a short quantum dot there is minimal spatial separation between the features of  $|\Psi|^2$  causing the wider tip potential ( $R_{tip} = 20$  nm) to blur any distinguishing features. Shorter dot lengths could potentially be explored if tips with metallic carbon nanotubes placed at the ends, or a similar geometry, are used. The quantum dots that are considered in this chapter have an aspect ratio of approximately 10, with  $d_{dot} = 30$  nm and  $L_{dot} = 300$ -500 nm. A long dot in an ultra-thin nanowire ( $d_{dot} \sim 20$  to 30 nm) is effectively 1D for moderate electron number, because only one radial state is occupied for moderate electron numbers at liquid He temperatures. Additionally, for  $R_{tip} = 20$  nm only the axis along the length of the quantum dot offers the possibility of fine enough resolution to extract information about  $|\Psi|^2$ . Therefore, the rest of this chapter will focus on the method to extract information about the 1D amplitude of the wavefunction  $|\Psi(x)|^2$  along the axis of the nanowire, denoted as the x-axis.

### 4.3 Extracting the wavefunction - imaging mechanism

If the shape of the tip potential  $\Phi_{tip}$  is well known and the value of the change in energy  $\Delta E_N$  of an electron state in a quantum dot as a function of tip position  $x_{tip}$  can be measured from experiment, information about the wavefunction can be extracted. Figure 4.2 demonstrates the principle of the extraction technique. The first column (figure 4.2(a)-(c)) shows the density profile of  $|\Psi|^2$  for a quantum well in a 1D wire, section 4.3.1. In the second column (figure 4.2(d)-(f)), the tip potential  $\Phi_{tip}$  used to probe

the wavefunction is plotted, section 4.3.2. The third column (figure 4.2(g)-(i)), illustrates the change in energy of the quantum dot state as the tip is scanned in a straight line above the wire, section 4.3.3. The final column (figure 4.2(j)-(l)), demonstrates that by measuring the change in energy  $\Delta E_N$  and deconvolving  $\Delta E_N$  with the tip potential  $\Phi_{tip}$  the extracted wavefunction  $|\Psi_{ext}|^2$  provides information about the original density profile  $|\Psi|^2$ , section 4.3.4.

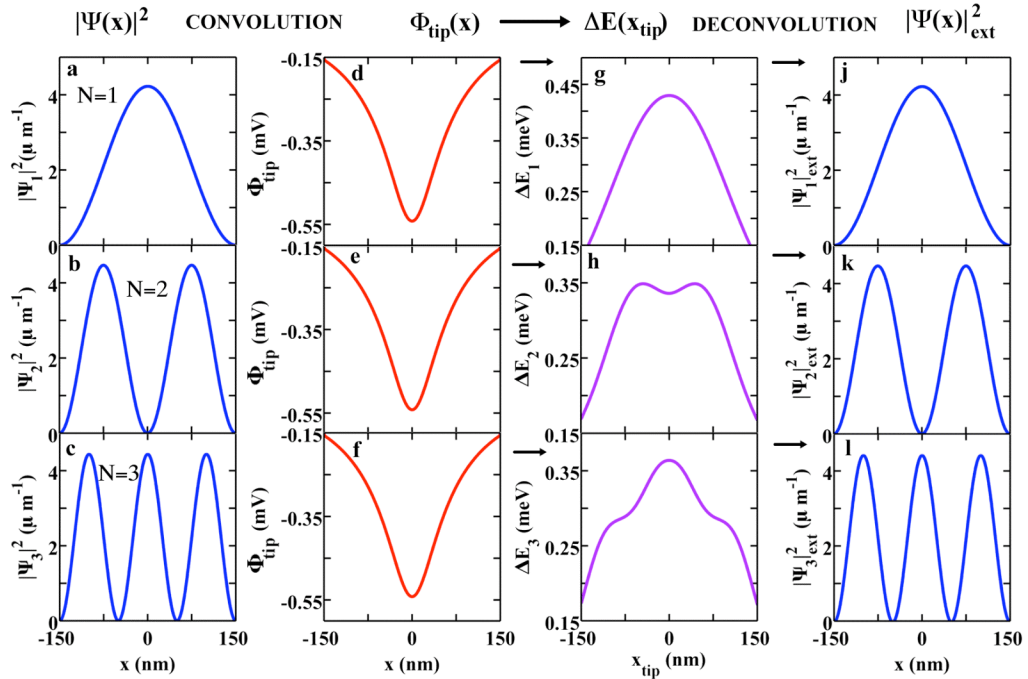


**Figure 4.2:** Demonstration of extracting the amplitude of the wavefunction  $|\Psi_{ext}(x)|^2$  for a nanowire with  $L_{dot} = 300$  nm,  $d_{dot} = 30$  nm ( $d_{dot}$  influences the width of the  $\Phi_{tip}$  the electrons see),  $V_{tip} = -10$  mV,  $H_{tip} = 10$  nm, and  $R_{tip} = 20$  nm. (a)-(c) The normalized single particle  $|\Psi_N|^2$  for the first three states of an electron in a quantum well. (d)-(f) The tip potential  $\Phi_{tip}$  modeled as a conducting sphere (equation 4.2). (g)-(i) Convoluting  $|\Psi_N|^2$  with  $\Phi_{tip}$  gives the change in energy of the dot  $\Delta E$  as a function of tip position. (j)-(l) If  $\Delta E$  is measured from experiment and the shape of  $\Phi_{tip}$  is well known,  $\Delta E$  can be deconvolved with  $\Phi_{tip}$  to extract the amplitude of the wavefunction  $|\Psi_{ext}|^2$ .

### 4.3.1 Density profile $|\Psi|^2$

The system is modeled as a non-interacting 1D electron gas with a quantum well with infinite potential side-walls. The values of  $|\Psi_N|^2$  in figures 4.2(a)-4.2(c) are calculated from the first three states of a normalized wavefunction of a particle in a 1D infinite potential well.

$$\Psi_N(x) = \sqrt{2/L_{dot}} \sin\left(\frac{N\pi x}{L_{dot}}\right) \quad (4.1)$$

While idealized wavefunctions are used to demonstrate the imaging technique, this method can operate as an experimental diagnostic tool to supply information about the amplitude of an unknown arbitrary wavefunction.

The proposed extraction technique is also applicable to quantum dots that contain multiple electrons. The amplitude of the wavefunction  $|\Psi_N|^2$  that would be extracted is the many-body ground state wavefunction. The amplitude of the many-body wavefunction can be calculated using density functional theory, a standard computational method, which utilizes the effective total density vs. position rather than the position of each individual particle. Qian *et al.* (2010) calculated the ground state many-body wavefunction for the transition from 3 to 4 electrons on a quantum dot and discussed manipulating the system with SGM imaging.

### 4.3.2 Tip potential $\Phi_{tip}$

The tip potential  $\Phi_{tip}$  is modeled as a charged metal sphere above a dielectric plane. Figures 4.2(d)-4.2(f) plot the first order term found from the method of image charges (an arrangement of multiple image charges is needed for this case) to calculate the electric potential from a charged metal sphere that is held above a dielectric slab [Topinka 2002]:

$$\Phi_{tip}(x) = \frac{2R_{tip}V_{tip}}{(\epsilon_1 + \epsilon_2)\sqrt{x^2 + (r_{dot} + H_{tip} + R_{tip})^2}} \quad (4.2)$$

where  $V_{tip}$  is the voltage applied to the tip with respect to ground,  $\epsilon_1$  and  $\epsilon_2$  are the relative permittivity of the nanowire ( $\epsilon_1 = 15.4$ ) and vacuum ( $\epsilon_2 = 1$ ),  $r_{dot}$  is the radius of the nanowire, and  $H_{tip}$  is the height of the bottom of the tip from the top of the wire ( $H_{tip} = 10$  nm). Topinka (2002) showed that the first term of the series is a good fit to the actual potential of a charged tip over a 2 dimensional electron gas (2DEG) structure. In figure 4.3 to prove that this approximation is valid for a charged metal sphere over a nanowire, we compare the tip potential  $\Phi_{tip}$  (red dashed line) from the method of image charges (equation 4.2) with the potential  $\Phi_{tip}$  (blue solid line) found with an electrostatic calculation over the length of the wire. To find  $\Phi_{tip}$  (blue solid line) we model the electrostatic setup, including the backgate, SiO<sub>2</sub> dielectric layer, InAs quantum dot, and metallic spherical tip, using finite-element modeling software (Maxwell 3D) and compute the potential from the tip in the center of the nanowire. With the tip held above the center of the quantum dot, the potentials agree well with minor divergence when nearing the

ends of the quantum dot showing that equation 4.2 is a suitable approximation for the potential  $\Phi_{tip}$  of a tip above a nanowire.

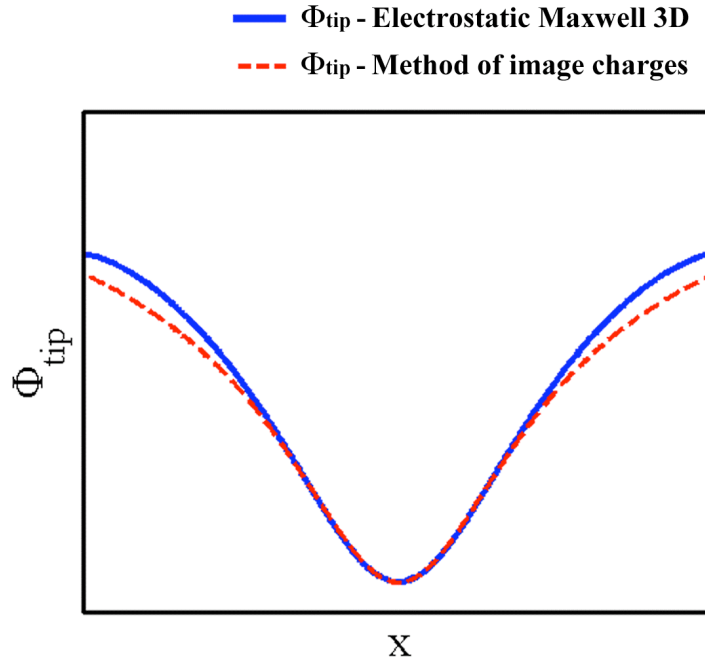


**Figure 4.3:** Comparison of two methods of calculating  $\Phi_{tip}$  ( $R_{tip} = 20$  nm) over the length of the dot. The solid blue line is the  $\Phi_{tip}$  found from an electrostatic calculation of the tip over the center of the dot using Maxwell 3D to include the conducting spherical tip, the InAs nanowire, the SiO<sub>2</sub> layer, and the metallic backgate. The red dashed line is  $\Phi_{tip}$  modeled from the first term of the method of image charges of a conducting sphere over a plane (equation 4.2). There is good agreement in the shape of  $\Phi_{tip}$  near the tip, with the potentials diverging slightly at positions moving away from the tip.

### 4.3.3 Convolution - change in energy $\Delta E_N(x_{tip})$

From first order perturbation theory the change in energy  $\Delta E_N$  of an electron state in a quantum dot as a function of tip position  $x_{tip}$  is given by the expectation value of the

perturbing potential  $\langle \Psi_N(x) | e\Phi_{tip}(x - x_{tip}) | \Psi_N(x) \rangle$ , which is the integral of the amplitude of the wavefunction  $|\Psi_N|^2$  of the unperturbed state with the tip potential  $\Phi_{tip}$ .

$$\Delta E_N(x_{tip}) = \langle \Psi_N(x) | e\Phi_{tip}(x - x_{tip}) | \Psi_N(x) \rangle = e \int_{-\infty}^{\infty} |\Psi_N(x)|^2 \Phi_{tip}(x - x_{tip}) dx \quad (4.3)$$

This approximation is valid as long as the strength of the tip perturbation is small compared to the potential of the dot [Fallahi 2006]. The integral in equation 4.3 is the convolution of  $|\Psi_N|^2$  with  $e\Phi_{tip}$ .

$$\Delta E_N(x_{tip}) = e \int_{-\infty}^{\infty} |\Psi_N(x)|^2 \Phi_{tip}(x - x_{tip}) dx = |\Psi_N(x)|^2 * (e\Phi_{tip}(x)) \quad (4.4)$$

where  $*$  denotes the convolution function. The convolution property states when [Oppenheim et al. 1997]:

$$y(x) = g(x) * h(x) \quad (4.5a)$$

then

$$Y(jk) = G(jk)H(jk) \quad (4.5b)$$

where  $Y(jk)$ ,  $G(jk)$ , and  $H(jk)$  are the Fourier transforms of  $y(x)$ ,  $g(x)$ , and  $h(x)$ , respectively. Therefore from equations 4.4 and 4.5:

$$\mathfrak{S}[\Delta E_N(x_{tip})] = \mathfrak{S}[|\Psi_N(x)|^2] \mathfrak{S}[e\Phi_{tip}(x)] \quad (4.6)$$

where  $\mathfrak{S}$  denotes taking the Fourier transform. Therefore, the change in energy of the dot  $\Delta E_N$  can be calculated by convolving  $|\Psi_N|^2$  with  $e\Phi_{tip}$  as shown in figure 4.2(a)-4.2(i).

### 4.3.4 Deconvolution - $|\Psi_{\text{ext}}|^2$

When  $\Delta E_N$  is measured and  $\Phi_{\text{tip}}$  is well-known,  $\Delta E_N$  can be deconvolved with  $\Phi_{\text{tip}}$  to return the amplitude of the wavefunction  $|\Psi_N|^2$ , figure 4.2(j)-4.2(l). Performing a deconvolution is the inverse of the convolution; from equation 4.6 it follows that the deconvolution of  $\Delta E_N$  with  $\Phi_{\text{tip}}$  is:

$$|\Psi_N(x)|^2 = \mathfrak{S}^{-1}\left(\mathfrak{S}[\Delta E_N(x_{\text{tip}})] / \mathfrak{S}[e\Phi_{\text{tip}}(x)]\right) \quad (4.7)$$

where  $\mathfrak{S}^{-1}$  denotes taking the inverse Fourier transform. This demonstrates that the amplitude of the wavefunction  $|\Psi_N|^2$  can be experimentally found if  $\Phi_{\text{tip}}$  is well-known and  $\Delta E_N$  can be measured.

## 4.4 Imaging resolution

When demonstrating the imaging technique in this chapter, we extract the wavefunction  $|\Psi_{\text{ext}}|^2$  exactly, because in order to establish the extraction technique as viable, a model with no noise and an exactly known tip potential  $\Phi_{\text{tip}}$  is used. When performing the extraction experiment on a device, the degree of accuracy with which the tip potential  $\Phi_{\text{tip}}$  and the change in energy  $\Delta E(x_{\text{tip}})$  of the dot are known when performing the deconvolution, the width of the tip potential  $\Phi_{\text{tip}}$ , and the width of the wavefunction's features  $|\Psi|^2$  will all influence the resolution of the extracted wavefunction  $|\Psi_{\text{ext}}|^2$ .

#### 4.4.1 Accuracy of $\Phi_{tip}$ and $\Delta E(x_{tip})$

When performing the experiment, how well-known the tip potential  $\Phi_{tip}$  is will influence the resolution of the extracted wavefunction  $|\Psi_{ext}|^2$ . If the tip potential  $\Phi_{tip}$  is very narrow relative to the features of the wavefunction  $|\Psi|^2$ , then the convolution of the two will produce a function that is very close in shape to the wavefunction  $|\Psi|^2$ . However, if the tip potential  $\Phi_{tip}$  is broad compared to the wavefunction  $|\Psi|^2$  then the wavefunction's features will be blurred and the convolution will look similar to the tip potential  $\Phi_{tip}$ . The greater the difference between the wavefunction  $|\Psi|^2$  and the convolution  $\Delta E$ , the more sensitive the wavefunction extraction will be to how precisely the tip potential  $\Phi_{tip}$  is known. Exploring narrower tips, such as a metallic carbon nanotube on the end of a  $R_{tip} = 20$  nm tip, is one way to increase the resolution. In an experimental setup, noise will reduce the accuracy with which  $\Delta E$  can be measured. It is important to consider the benefits of windowing the data before performing the deconvolution when dealing with a system that contains noise. Any error in  $\Delta E$  or  $\Phi_{tip}$ , when performing the deconvolution, will reduce the accuracy with which  $|\Psi_{ext}|^2$  can be extracted.

#### 4.4.2 Relative width of tip potential $\Phi_{tip}$ and wavefunction features

In addition to the physical size of the tip, the width of the tip potential  $\Phi_{tip}$  seen by the electrons is influenced by the separation between the electrons and the tip. Figure 4.4 shows the difference varying  $H_{tip}$  has on the measurement of the change in energy  $\Delta E_2(x_{tip})$  of the dot ( $N = 2$ ). Figure 4.4(a)-(c) plots  $\Delta E_2(x_{tip})$  for a dot with  $L_{dot} = 300$  nm and  $d_{dot} = 30$  nm and figure 4.4(d)-(f) plots  $\Delta E_2(x_{tip})$  for a dot with  $L_{dot} = 500$  nm and  $d_{dot} = 30$  nm, both at values of  $H_{tip} = 10$  nm, 20 nm, and 40 nm. As the distance  $H_{tip}$  between the tip and the nanowire increases, the splitting between the peaks of  $\Delta E_2(x_{tip})$  decreases until the two peaks are blurred together and only one large peak remains, figure 4.4(c). As expected, a smaller  $H_{tip}$  produces greater definition between the two peaks of  $\Delta E_2$ , which is related to resolving the two peaks in  $|\Psi_2|^2$ , figure 4.4(a). The greater the distance between the electrons and the tip the broader  $\Phi_{tip}$  becomes and the lower the resolution. This makes ultra-thin semiconductor nanowires a favorable system to perform wavefunction extraction compared to a 2DEG quantum dot, because the electrons are closer to the surface. The smaller the radius  $r_{dot}$  of the nanowire and the closer the tip is to the nanowire  $H_{tip}$ , the sharper the tip potential  $\Phi_{tip}$  will appear to the electrons. As explained in section 4.4.1, the sharper the tip potential the less sensitive the wavefunction extraction is to the precise form of  $\Phi_{tip}$ .

The relative width of the tip potential compared to the wavefunction features can also be controlled by changing the spatial extent of the wavefunction. Figure 4.7 shows

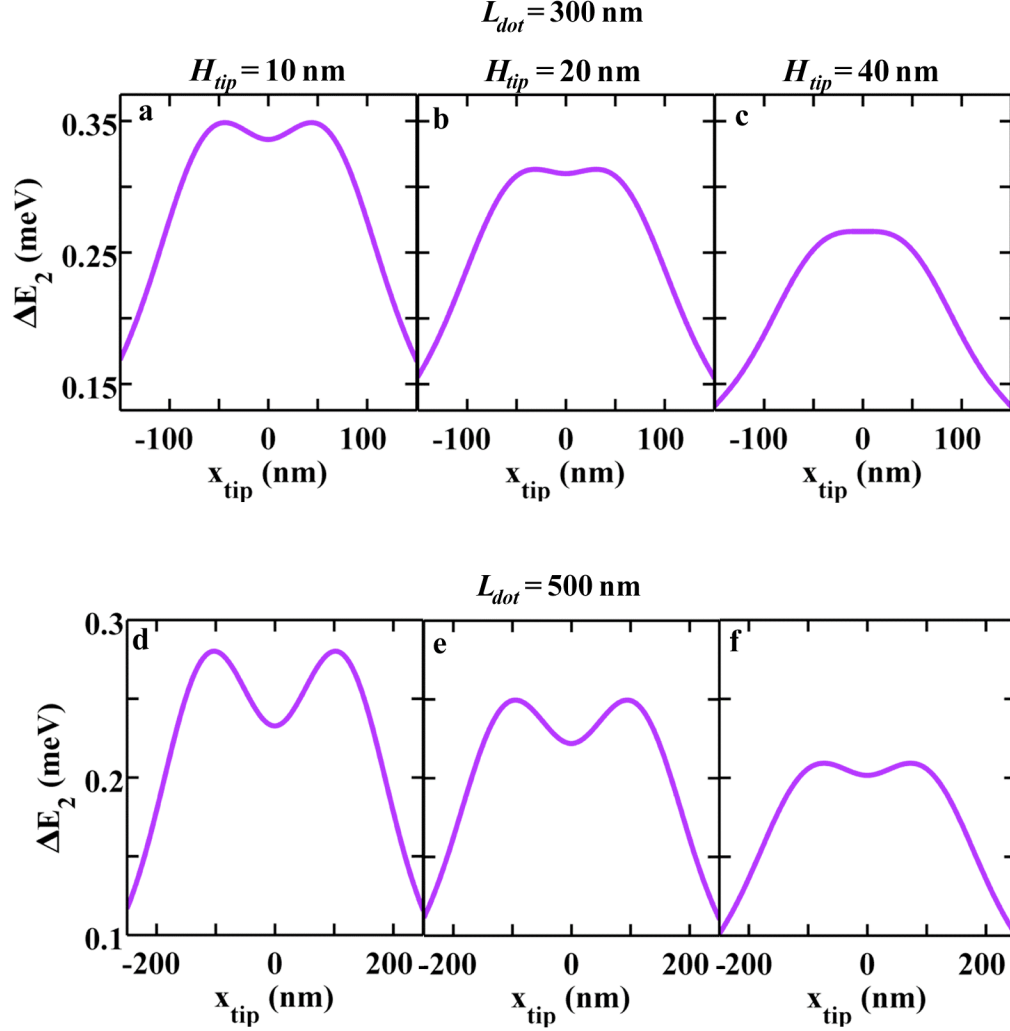


**Figure 4.4:** The change in  $\Delta E_2(x_{tip})$  for a variety of values of  $H_{tip}$  and  $L_{dot}$  ( $d_{dot} = 30$  nm). Decreasing the separation  $H_{tip}$  between the nanowire and the tip ( $R_{tip} = 20$  nm), (a)-(c) and (d)-(f), for a given  $L_{dot}$  gives a sharper tip potential, which increases the similarity of  $\Delta E_2(x_{tip})$  to  $|\Psi_2|^2$ . Likewise, increasing the dot length  $L_{dot}$  also improves the clarity of the features of  $|\Psi_2|^2$ .

That, with the same size tip and the same  $H_{tip}$ , increasing  $L_{dot}$  from 300 nm to 500 nm increases the resolution of  $\Delta E_2(x_{tip})$  of the dot. Comparing figure 4.4(a) where

$L_{dot} = 300$  nm and figure 4.4(d) where  $L_{dot} = 500$  nm, the resolution of the peak splitting is vastly improved with a longer dot, figure 4.4(d). When comparing  $\Delta E_2(x_{tip})$  at  $H_{tip} = 40$  nm for both dot lengths, figure 4.4(c) and figure 4.4(d), at  $L_{dot} = 300$  nm the peak splitting is nearly blurred out, but by increasing  $L_{dot}$  to 500 nm the peak separation becomes clearly visible. By elongating the quantum dot, the features of the wavefunction  $|\Psi|^2$  are widened, which improves the visibility of the features of  $|\Psi|^2$  in the images of  $\Delta E(x_{tip})$ .

## 4.5 Measuring the energy shift $\Delta E_N$ - experimental setup

In order to measure the change in energy of the dot  $\Delta E(x_{tip})$  by the tip, we propose using a SGM and a feedback loop between the nanowire current  $I_{sd}$  and the backgate voltage  $V_{bg}$ . Coulomb blockade energy level spectroscopy is an excellent method to measure the energy states in a quantum dot (Tarucha *et al.* 1996). The change in the energy states of the quantum dot  $\Delta E_N$  can be found by changing the tip position  $x_{tip}$ , which alters the  $V_{bg}$  at which a Coulomb blockade conductance peak occurs. The change in backgate voltage  $V_{bg}$  needed to remain at the same point of a Coulomb blockade peak is proportional to  $\Delta E$  as the tip is scanned in a straight line above the quantum dot.

Figure 4.5(a) is a graphical representation of the effect that the location of the tip has on the charge stability diagram. The dotted parabolas, in figure 4.5(a), are the electrostatic energy of the quantum dot when the charging energy is much larger than the

single particle energy spacing and no tip is present. See Chapter 2 for an in-depth explanation of Coulomb blockade. When scanning a dot, where the single particle energy spacings can be neglected compared to the charging energy, the change in energy of the dot due to the tip  $\Delta E_N(x_{tip})$  must be accounted for, which causes the parabolas to shift upward by  $\Delta E_N(x_{tip})$  as shown by the solid parabolas in figure 4.4(a). The size of each parabola's shifts varies depending on the amplitude of that state's wavefunction at  $x_{tip}$ . The parabolas' relative shifts in energy:

$$\Delta E_{SN} = \Delta E_N(x_{tip}) - \Delta E_{N-1}(x_{tip}) \quad (4.8)$$

changes the  $V_{bg}$  at which the parabolas intersect, and therefore where  $eN$  and  $e(N-1)$  are degenerate charge states of the quantum dot and the Coulomb blockade is lifted.

When collecting data with the SGM, we measure the Coulomb blockade conductance peaks as a function of backgate voltage  $V_{bg}$  as discussed in Chapter 2. Figure 4.5(b) is a schematic of the first three Coulomb blockade peaks of a quantum dot. The red dotted trace corresponds to the location of the Coulomb blockade peaks with no tip present. As the tip is scanned along the dot, the peak shifts to the blue solid trace by an amount  $\Delta V_{SN}$ :

$$V_{SN}(x_{tip}) = \frac{C_{\Sigma}}{eC_{dot-bg}} (\Delta E_N(x_{tip}) - \Delta E_{N-1}(x_{tip})) \quad (4.9)$$

where  $C_{\Sigma}$  is the total capacitance of the dot,  $C_{dot-bg}$  is the capacitance of the dot to the backgate, and  $E_N$  is the energy of the dot with N electrons. The most relevant aspect of equation 4.9 to imaging the wavefunction is that:

$$\Delta V_{SN}(x_{tip}) \propto \Delta E_N(x_{tip}) - \Delta E_{N-1}(x_{tip}) \quad (4.10)$$

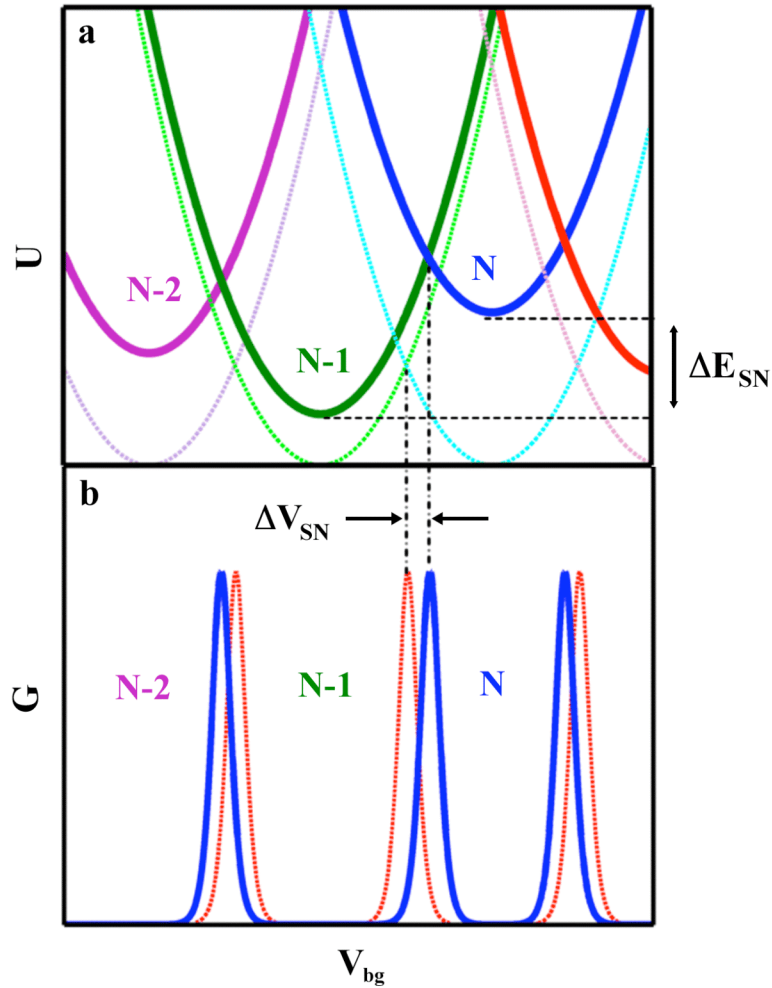


**Figure 4.5:** (a) Free energy  $U$  vs. backgate voltage  $V_{bg}$ . The dotted parabolas are the electrostatic energy when the single particle energy levels can be neglected and no tip is present. The number of electrons on the dot changes by one when the dashed parabolas intersect.  $N$ ,  $N-1$ ,  $N-2$  represent the number of electrons on the dot. The solid parabolas are the free energy of the dot, when the tip changes the energy of the dot by  $\Delta E_N(x_{tip})$ . This interaction shifts the parabolas up in  $U$  by  $\Delta E_N(x_{tip})$  and shifts the intersection of the parabolas along the  $V_{bg}$  axis. (b) The shift changes the location of the Coulomb blockade conductance peaks as shown in equation 4.9. The red dotted Coulomb blockade peaks correspond to the intersections of the dotted energy parabolas when no tip is present. The blue solid Coulomb blockade peaks show the shift in  $V_{bg}$  of the Coulomb blockade peaks with the tip present. The change in Coulomb blockade peak spacing  $\Delta V_{SN}$  due to the tip is proportional to the difference in the change in energy of two states due to the tip position:  $\Delta V_{SN}(x_{tip}) \propto \Delta E_N(x_{tip}) - \Delta E_{N-1}(x_{tip})$ .

Therefore, our SGM measurements would yield  $\Delta E_N(x_{tip}) - \Delta E_{N-1}(x_{tip})$ , which after some analysis can be deconvolved with the tip potential (equation 4.7) to produce information about the wavefunction.

A negative feedback loop controlled by the computer is proposed to fix the value of the conductance  $G_{sd}$  through the nanowire by changing the applied  $V_{bg}$  as the SGM tip is scanned at a constant height along the length of the nanowire. The experimental setup we propose to extract the wavefunction is shown in figure 4.1. Figure 4.6 demonstrates the feedback loop and shows that  $V_{bg}(x_{tip})$  is varied in order to keep  $G_{sd} = \text{constant}$ . In figure 4.6 the tip is aligned over the nanowire using the method detailed in section 3.2.3. The tip voltage  $V_{tip}$  and the backgate voltage  $V_{bg}$  are adjusted in order that the conductance through the nanowire is at half the Coulomb blockade peak height, marked by the red dots in figure 4.6. The tip is then swept in a straight line at constant  $H_{tip}$  above the nanowire along the  $x_{tip}$  axis. Without a feedback loop, the Coulomb blockade conductance peak will shift along the  $V_{bg}$  axis as the tip is scanned in a straight line above the dot, figure 4.6. By using a feedback loop to the computer, the software can add or subtract a quantity to  $V_{bg}$  at each value of  $x_{tip}$  to keep  $G_{sd}$  constant. In figure 4.6 as the tip is moved along the length of the nanowire,  $V_{bg}$  is varied by an amount  $\Delta V_{SN}$  (purple line) to keep the nanowire conductance fixed. By measuring the output  $\Delta V_{SN}$  we can find the difference in  $\Delta E$  from equation 4.9.

From equation 4.7, the change in energy of a single state  $\Delta E_N(x_{tip})$  is needed to extract the wavefunction of that state  $|\Psi_N|^2$ . Equation 4.10 shows that  $\Delta V_{SN}(x_{tip})$  measured from the feedback loop is proportional to the difference in the change in energy

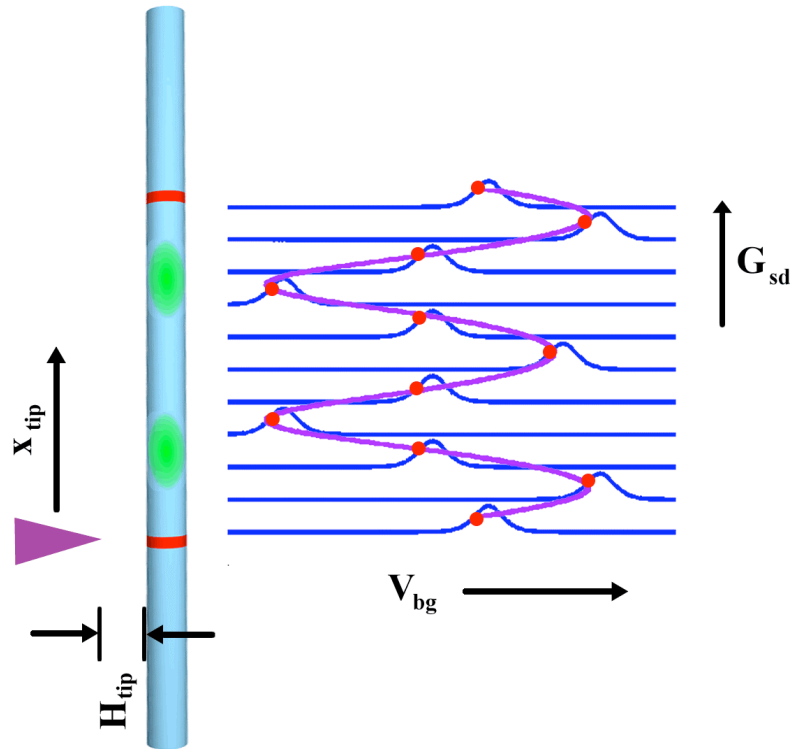


**Figure 4.6:** Illustration of the transition between  $N = 2$  and  $N = 3$  wavefunction on the quantum dot  $x_{tip}$ , which is in the  $N = 2$  state. The green regions in the dot represent the charge distribution of the electrons. For an idealized non-interacting 1D electron gas with spin  $1/2$ , this transition from wavenumber  $N = 2$  to  $N = 3$  corresponds to adding the fifth electron to the dot. The blue traces to the right show the Coulomb blockade conductance peak where it is equally energetically favorable for the dot to hold either 4 or 5 electrons. As the tip changes its location  $x_{tip}$ , the backgate voltage  $V_{bg}$  the peak occurs at shifts. The red dots mark the same value of conductance for each tip position  $x_{tip}$ . The purple line traces how  $V_{bg}$  must vary in order to keep the conductance  $G_{sd}$  of the nanowire constant. The change in  $V_{bg}$ , purple line, is proportional to  $\Delta E_3(x_{tip}) - \Delta E_2(x_{tip})$ .

of two states  $\Delta E_N(x_{tip}) - \Delta E_{N-1}(x_{tip})$ . Figure 4.7(a)-4.7(c) shows the difference in energies  $\Delta E_N(x_{tip}) - \Delta E_{N-1}(x_{tip})$  from the first three Coulomb blockade peaks. By assuming that  $\Delta E_0(x_{tip})=0$  and performing simple addition, the change in energy  $\Delta E_N(x_{tip})$  of the first three states of the dot are found as seen in figure 4.7(d)-4.7(f).

The changes in energy  $\Delta E_N$  can be deconvolved (equation 4.7) with the known tip potential  $\Phi_{tip}$  to extract  $|\Psi_{ext}(x_{tip})|^2$ , as shown in figure 4.2. This method is unique because it allows a single system to measure both the individual energy of electrons in an electron gas and to measure the amplitude of the electron wavefunction  $|\Psi_N|^2$ . Having knowledge of the energy states and  $|\Psi_N|^2$  of electrons buried in confined systems is extremely beneficial when designing future nanoelectronics or quantum information processing devices.

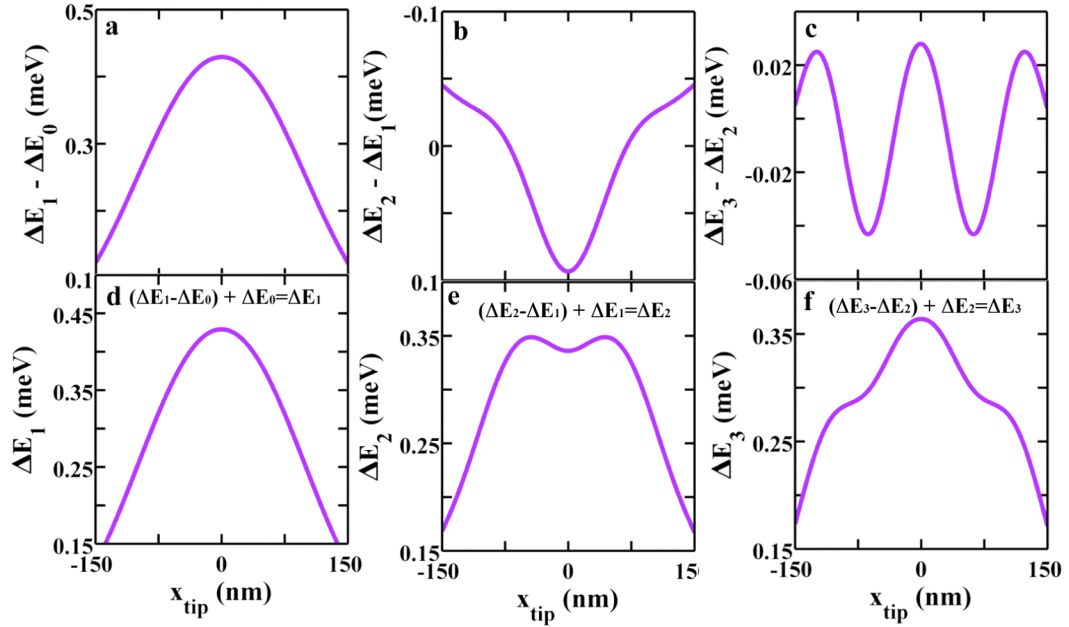


**Figure 4.7:** (a)-(c) Shows the difference in the change of energy  $\Delta E_N(x_{tip}) - \Delta E_{N-1}(x_{tip})$  of quantum states of a dot for  $N = 1$  to  $3$ , which is proportional to change in backgate voltage  $V_{bg}$  needed to keep the current  $I_{sd}$  through the nanowire constant. This model has a nanowire and a tip with  $L_{dot} = 300$  nm,  $d_{dot} = 30$  nm,  $V_{tip} = -10$  mV,  $H_{tip} = 10$  nm, and  $R_{tip} = 20$  nm. (d)-(f) Assuming that  $\Delta E_0(x_{tip}) = 0$ , gives  $\Delta E_1(x_{tip}) - \Delta E_0(x_{tip}) = \Delta E_1(x_{tip})$  as seen in (d). Likewise, using simple addition  $\Delta E_2(x_{tip})$  and  $\Delta E_3(x_{tip})$  are also found in (e) and (f). The  $\Delta E$  in (d)-(f) can be deconvolved with  $\Phi_{tip}$  to extract the amplitude of the wavefunction  $|\Psi_{ext}|^2$  as shown in figure 4.2.

# Chapter 5

## Imaging quantum dots in 1D ultra-thin InAs/InP nanowires

### 5.1 Overview

One-dimensional (1D) semiconductor nanostructures, such as nanowires [Hiruma *et al.* 1993; Hiruma *et al.* 1996; Ohlsson *et al.* 2001; Björk *et al.* 2002a; Björk *et al.* 2002b; Lieber 2003, Fuhrer *et al.* 2007], carbon nanotubes [Iijima 1991; Dai *et al.* 1996; Tans *et al.* 1997; Deshpande and Bockrath 2008], and cleaved-edge overgrowth wires [Goni *et al.* 1992; Yoshita *et al.* 2002; Auslaender *et al.* 2005], offer the opportunity to investigate interesting electronic phenomena in 1D. Select quantum mechanical effects that are not present or vastly more complicated in higher dimensional systems can be explored. Examples of effects that could be studied in 1D systems include the longitudinal wavefunction of a one-electron system which is discussed in chapter 4 of

this thesis [Fallahi 2006], spin-charge separation of charge carriers [Auslaender *et al.* 2005], and transition from a Luttinger Liquid to a Wigner Crystal state [Matveev 2004; Deshpande and Bockrath 2008; Qian *et al.* 2010]. For all of these materials, a very high quality sample with little disorder is needed to create a system where 1D physics can be accessed and studied.

There is widespread interest in designing electronic devices which operate on the basis of quantum mechanical principles, as demonstrated by the recent program solicitation “Nanoelectronics for 2020 and Beyond” issued jointly by the National Science Foundation and the semiconductor industry’s Nanoelectronic Research Initiative. A fundamental understanding of low-dimensional systems is essential to achieving nanoelectronic circuits. Significant attention and research has been focused on the concept of nanoelectronic components with control over individual electrons and the information in the system is represented by electron location or electron spin. However, determining the spatial behavior of electrons in experimental systems is quite difficult. Scanning gate microscopy is especially suited for probing the spatial and electrical properties of electrons in nanostructures in order to assist in expanding our knowledge of how to design nanoelectronics.

Liquid-He cooled scanning gate microscopes (SGMs) have been recognized as valuable tools for increasing the understanding of nanoscale systems, such as two-dimensional electron gases [Tessmer *et al.* 1998; Topinka *et al.* 2000; Topinka *et al.* 2001; Fallahi *et al.* 2005; Gildemeister *et al.* 2007; Jura *et al.* 2007], carbon nanotubes [Woodside and McEuen 2002], and graphene [Berezovsky *et al.* 2010a; Berezovsky *et al.*

2010b; Schnez *et al.* 2010]. As discussed in chapter 4, liquid-He cooled scanning tunneling microscopes (STMs) deliver detailed images of electron waves on the surface of materials [Heller *et al.* 1994; Manoharan *et al.* 2000], but STMs cannot access electrons that are inside of a nanostructure. SGMs access electrons under the surface of a nanostructure by capacitive coupling, which supplies images of electrons in the interior of the device, which will be important for designing future nanoelectronics. An SGM provides high spatial resolution images of conductance, which is beyond the capabilities of typical transport measurements alone. Scanning gate microscopy is well suited to probe 1D systems, because it can locate the position of quantum dots, and it offers the ability to perform spatially resolved energy-level spectroscopy on individual dots. A conductance image is made by displaying the conductance through the nanowire vs. tip position as the conducting SGM tip is raster scanned at a constant height above the surface. In previous SGM studies, larger diameter wires were used for which multiple radial modes were always occupied [Bleszynski *et al.* 2007; Bleszynski-Jayich *et al.* 2008]. Scanning gate microscopy provides information beyond that of optical microscopy or traditional transport measurements to assist in the development of very high quality 1D devices.

As described in section 2.1, InAs/InP heterostructure nanowires are a particularly favorable system to probe 1D semiconductor physics. There is great interest in developing very clean, high quality 1D systems. It is necessary for nanowires to be ultra-thin (diameter,  $d_{NW} \sim 20$  to 30 nm) for the system to be quantum mechanically 1D with only one occupied radial state for moderate electron number at liquid-He

temperatures. A thorough understanding and control of the transport properties, growth, and structure of semiconductor nanowires is essential for their promised potential to be realized as laboratories for 1D physics.

In this chapter, we characterize a 1D ultra-thin ( $d_{NW} \sim 30$  nm) InAs/InP heterostructure nanowire that contains a grown-in epitaxial InAs quantum dot defined by InP tunneling barriers, using spatially resolved energy-level spectroscopy. A conducting tip in our home-built liquid-He-cooled SGM serves as a movable gate to locally gate an InAs/InP nanowire. We spatially map the conductance  $G$  through the nanowire vs. the tip position  $x_{tip}$  and  $y_{tip}$ . In section 5.2, we introduce the experimental setup and the ultra-thin nanowire devices. Section 5.3 presents a Coulomb blockade diamond transport measurement of an ultra-thin InAs/InP nanowire. The complexity of the Coulomb blockade diamond plot illustrates the difficulty of understanding ultra-thin heterostructure nanowires from traditional transport measurements alone. In section 5.4, we show the experimental results from the SGM images. In section 5.4.1, elliptical rings of high conductance, corresponding to Coulomb blockade conductance peaks, are found to be centered on the epitaxially grown InAs quantum dot. Two additional quantum dots are also apparent in the conductance images. These additional quantum dots are formed near the metal/semiconductor contacts at the ends of the nanowire. In section 5.4.2, we find the length of the epitaxially grown quantum dot  $l_{ep}$  to be approximately 310 nm, in good agreement with growth specifications. By comparing the ring spacings with that of the center dot, we estimate the sizes of the additional dots. In section 5.4.3, we describe the method to obtain information about certain system capacitances and the strength of

coupling from the spatial conductance images. Finally, in section 5.5 we discuss future directions related to changes in the nanowires' parameters and the contacts.

## 5.2 Ultra-thin InAs/InP nanowire devices

InAs nanowires containing an InAs quantum dot defined by InP tunnel barriers were epitaxially grown on InAs <111>B substrates using chemical beam epitaxy [Jensen *et al.* 2004]. The top layer on an InAs <111>B substrate is As. The nanowires were grown by Kristian Storm from the Samuelson Group at Lund University as part of our groups' collaboration. Size selected gold aerosol particles were chosen as growth catalysts to produce ultra-thin nanowires with diameter  $d_{NW} \sim 30$  nm and length  $l_{NW} \sim 2$  to 3  $\mu\text{m}$ . InAs sections and InP barriers are grown by switching gas precursors during growth. A long epitaxially grown InAs quantum dot with nominal length  $l_{ep} = 300$  nm was formed by two 2-nm-long InP tunnel barriers. A long epitaxial quantum dot, one of length much longer than its diameter, was chosen to allow us to probe the electron density profile along the nanowire in order to study the 1D physics of the electron. The physical state of the 1D electron gas changes between a Wigner Crystal and a Luttinger Liquid based on the density of the electrons in the quantum dot. At low densities the electrons behave semi-classically and the electrostatic repulsion creates a row of electrons, a Wigner Crystal, in the quantum dot along the nanowire axis [Matveev 2004b]. At higher densities in one dimension a Luttinger Liquid is formed. The electrons behave as bosons and spin-charge separation of the electrons occurs [Fiete 2007].

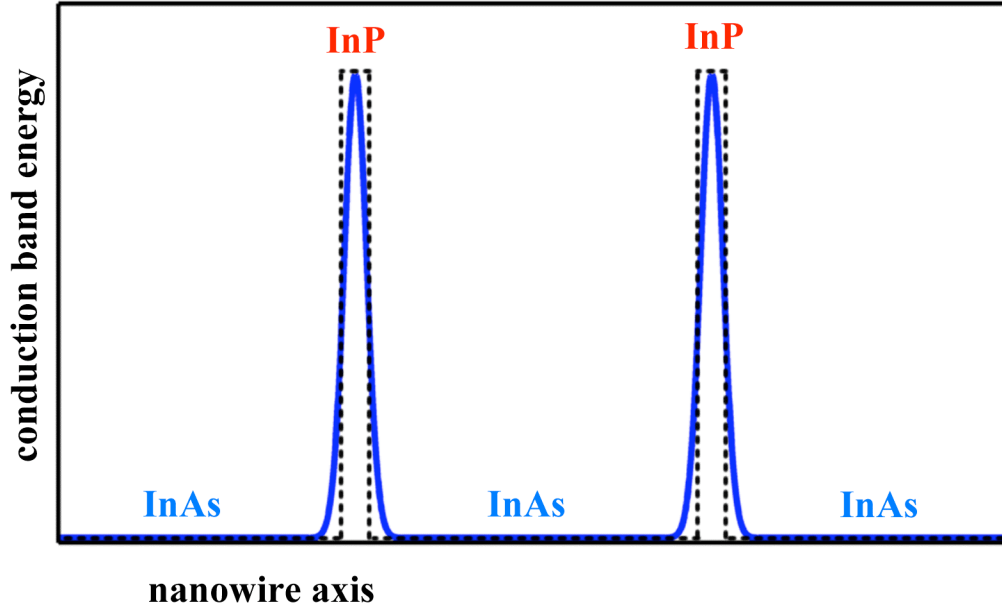


**Figure 5.1:** Energy profile of the conduction band edge of an InAs/InP heterostructure nanowire. The approximately 0.6 eV conduction band offset between InAs and InP forms a quantum dot with strong electronic confinement. The black dashed line shows the conduction band edge with no strain present. The strain at the interface of InAs and InP creates conduction band bending. The solid blue line sketches a probable shape of the conduction band accounting for strain. The tunnel barriers become thicker at lower energies. The first few electrons on the dot will have lower energies and must tunnel through the thicker barrier in order for the nanowire to conduct.

The length of the InP tunnel barriers was chosen to be 2 nm because the strain between InAs and InP causes bending of the conduction band at the interface [Larsson *et al.* 2007]. Figure 5.1 compares a sketch of the ideal conduction band of an InAs/InP nanowire (black dashed line) with a sketch of the conduction band that accounts for strain (blue solid line). Rather than the tunnel barrier being a square well potential as in the ideal case, the strain produces a Gaussian-like barrier that is thicker at the base. The first few electrons on the dot will have lower energy and will encounter the thicker base of the

tunnel barrier. If a 2 nm barrier is grown in an ultra-thin nanowire, the base of the barrier is 5-7 nm thick, and in order for electrons to tunnel the barrier cannot be much thicker. The  $\sim 0.6$  eV conduction band offset between InAs and InP in figure 5.1 forms a potential well with strong electronic confinement. The In growth source used for the InAs quantum dot was triethylindium (TEIn) and the growth source for the InAs nanowire leads was trimethylindium (TMIn) to enhance carbon doping in the nanowire leads. The carbon n-dopes the nanowire leads relative to the dot, allowing us to lower the electron number on the epitaxially grown quantum dot without first depleting the nanowire leads.

Figure 5.2(a)-(b) sketches an InAs/InP heterostructure nanowire with  $d_{NW} = 30$  nm, which was deposited on a degenerately doped Si substrate with 100 nm cap of thermal oxide. The blue sections of the wire represent the InAs sections and the red sections represent the InP tunnel barriers. The InP tunnel barriers form a 300 nm long InAs quantum dot. The nanowires are electrically contacted with Ni/Au electrodes (yellow leads in figure 5.2(a)-(b)) defined using electron-beam lithography. Not shown in figure 5.2 is the doped substrate, which is used as a backgate by applying a gate voltage  $V_{bg}$  between the backgate and the nanowire. The SGM tip, figure 5.2(a)-(b), has a radius  $R_{tip} = 20$  nm and a voltage  $V_{tip}$  applied between the tip and the nanowire. In order to obtain a conductance image the tip is raster scanned with a constant applied  $V_{tip}$  and at a constant height above the nanowire. The conductance through the wire  $G$  is mapped vs. tip position  $x_{tip}$  and  $y_{tip}$ . Figure 5.2(c) is a scanning electron microscope (SEM) image of a contacted ultra-thin InAs/InP nanowire. Also visible in figure 5.2(c) are additional nanowires that were deposited but not contacted and a part of the number grid. The

nanowire sample is cooled in a home-built SGM [Topinka *et al.* 2000; Aidala *et al.* 2006] by He exchange gas in thermal contact with a liquid He bath at  $T=4.2$  K, which is covered in detail in section 3.2.

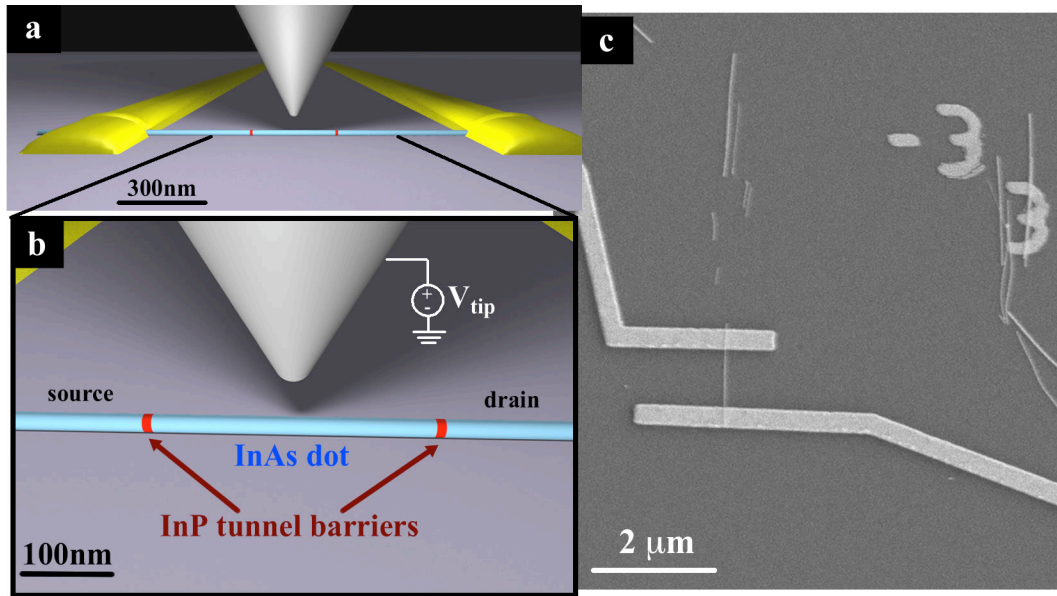


**Figure 5.2:** (a) Illustration of our scanning gate microscope (SGM) setup. (b) Two 2-nm-thick InP barriers form a  $\sim 300$ -nm-long quantum dot in an ultra-thin (30 nm diameter) epitaxially grown InAs nanowire. The nanowire is deposited onto a Si substrate with a capping layer of 100 nm of thermal oxide and is electrically contacted with Ni/Au leads. A backgate (not shown) globally tunes the electron density of the wire. The conducting tip acts as a moveable gate and has a radius of  $\sim 20$  nm. The applied tip voltage  $V_{tip}$  and the height above the nanowire are independently tuned. The moveable gate is held at a constant height and raster scanned. The quantum dot is much longer than it is wide, with a length-to-diameter ratio of  $\sim 10$ . All features are represented to scale, except the InP barriers, which are enlarged for ease of viewing. (c) A scanning electron microscope image of an electrically contacted ultra-thin InAs/InP heterostructure nanowire.

## 5.3 Experimental results - traditional transport

### measurements

Transport measurements of the ultra-thin nanowires with long epitaxially grown quantum dots described in section 5.2 yield Coulomb blockade diamonds with complex behavior as shown in figure 5.3, which plots the current  $I_{sd-offset}$  ( $I_{sd-offset} = |I_{sd}| + 10$  pA) vs. backgate voltage  $V_{bg}$  and source-drain bias  $V_{sd}$ , where  $I_{sd}$  is the current through the nanowire. The darker areas of figure 5.3 correspond to regions where the current is blocked by the Coulomb blockade. The many overlapping diamonds in the Coulomb blockade plot indicate that multiple quantum dots were formed along the ultra-thin nanowire. The location and origin of these confined electronic states is not apparent from traditional transport measurements alone, making it difficult to understand their source. The magnitude of the current in the Coulomb blockade plot is plotted on a log scale to accentuate the conductance change at small  $V_{sd}$ . At zero  $V_{sd}$  the current becomes very small or zero, even at the points where the Coulomb blockade diamonds are expected to close. The small current may be due to the tunnel barrier thickness at low electron energies or to Schottky barriers at the metal/semiconductor contacts.

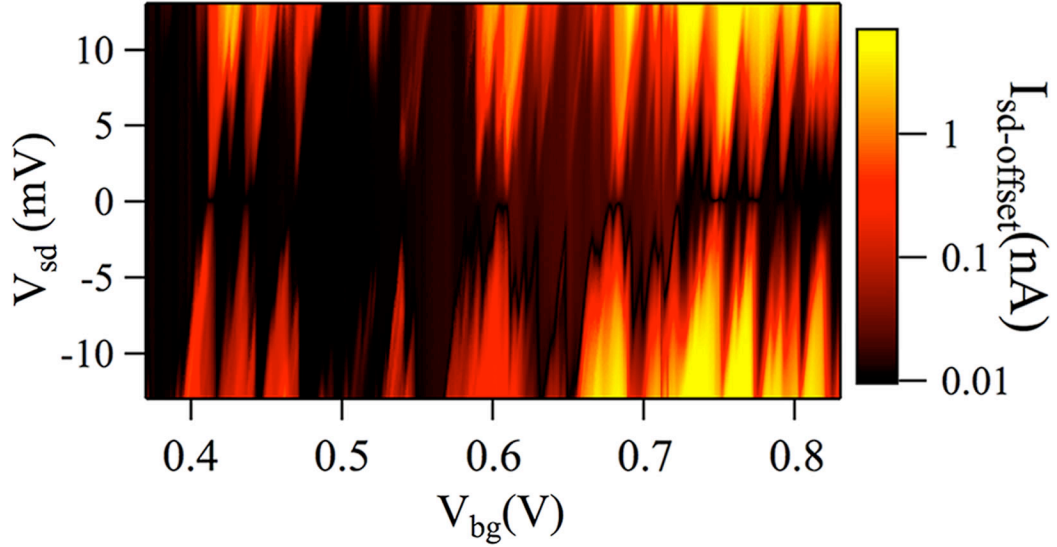


**Figure 5.3:** Transport measurements of the ultra-thin nanowire without the tip present at  $T = 4.2$  K. Coulomb blockade diamond plot where the offset current  $I_{sd\text{-offset}} = |I_{sd}| + 10$  pA is plotted vs. the backgate voltage  $V_{bg}$  and the source-drain bias  $V_{sd}$ . An offset of 10 pA is added to  $|I_{sd}|$  to be able to see the behavior at low source-drain bias. Complex Coulomb blockade diamonds are seen which would be very difficult to understand without scanning gate measurements.

## 5.4 Experimental results - SGM images of ultra-thin

### InAs/InP nanowires

#### 5.4.1 Quantum dot number and location

Using the SGM tip as a movable gate, we show that the Coulomb blockade diamond pattern in figure 5.3 was created by three individual quantum dots located in series along the nanowire. Figure 5.4(a) shows a conductance image for an ultra-thin nanowire with a long epitaxially grown dot vs. tip position  $x_{tip}$  and  $y_{tip}$ . The presence of

three sets of concentric overlapping rings in figure 5.4(a) indicates that there are three quantum dots in series along the length of the wire. The blue line shown in figure 5.4(b) marks the location of the nanowire, and the two red blocks denote the approximate positions of the two InP tunnel barriers. The shape of the conductance rings for the quantum dots are well fit by a series of ellipses, shown as the white dotted lines in figure 5.4(b). Each small solid dark blue circle represents the center for a quantum dot located at the center of the Coulomb blockade rings. For clarity, figure 5.4(c) illustrates the nanowire, barriers, center of the quantum dots, and conductance ring fits without the conductance image.

From the shape and spacing of the conductance rings, we determine that the center dot in figure 5.4 is the epitaxially grown quantum dot, and we find its length  $l_{ep} \approx 310$  nm (section 5.4.2), in good agreement with the growth parameters. The spatial separation of Coulomb blockade rings  $\Delta r$  is proportional to the inverse of the dot length for a particular dot  $\Delta r \propto 1/l_{dot}$ , because  $\Delta r \propto 1/E_C \propto 1/C_\Sigma$  and  $C_\Sigma \propto l_{dot}$ , where  $E_c$  is the charging energy of the dot,  $C_\Sigma$  is the total capacitance of the quantum dot, and  $l_{dot}$  is the length of the particular dot [Bleszynski *et al.* 2007]. In figure 5.4, the center epitaxial quantum dot has the closest spaced conductance rings, indicating that it is the longest dot. The large eccentricity of the conductance rings shows that the aspect ratio length/diameter  $l_{ep}/d_{dot}$  for the epitaxially grown dot is substantial. (See section 5.4.2 for a full description of the method used to find the length of the center dot.)

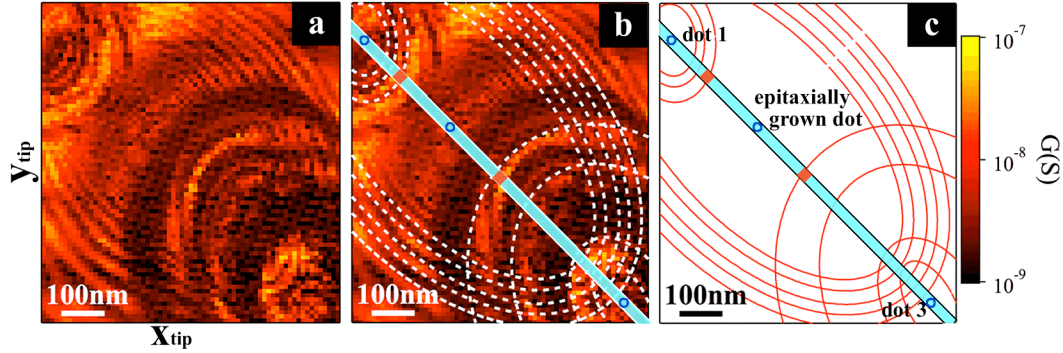


**Figure 5.4:** (a) Conductance image of an ultra-thin InAs/InP nanowire at  $T = 4.2$  K. The conductance  $G$  is plotted on a logarithmic color scale vs.  $x_{tip}$  and  $y_{tip}$ . The tip is scanned in a plane 60 nm above the nanowire and relative to the Ni/Au contacts as shown in figure 5.8(g). We found three quantum dots in series along the length of the nanowire. The center dot is the epitaxially grown dot, and dots 1 and 3 on either side are likely formed by Schottky barriers at the metal/semiconductor interface. (b) The blue line represents the location of the InAs nanowire and the red regions represent the approximate location of the two InP barriers (barriers are enlarged for ease of viewing). The small blue circles mark the centers of the quantum dots. The dashed white ellipses trace several of the Coulomb blockade conductance rings for each dot. The voltages are  $V_{tip} = -0.7$  V,  $V_{sd} = 2.5$  mV, and  $V_{bg} = 0.724$  V. (c) The conductance data is removed and only the nanowire, the InP barriers, the center markers, and the conductance ring fits are sketched.

In addition to the epitaxially grown quantum dot, the SGM images reveal two quantum dots, labeled dot 1 and dot 3, on either side of the epitaxial dot as shown in figure 5.4. The Coulomb blockade rings show that the center of the two additional quantum dots occurs between the epitaxially grown dot and the two metal/semiconductor contacts, suggesting that they are created by Schottky barriers at the interfaces. SGM conductance images disentangle the transport information for the three dots by spatially resolving the Coulomb blockade rings for each dot.

### 5.4.2 Quantum dot size

We find the length  $l_{ep}$  of the epitaxial dot by first measuring the minimum spacing  $\Delta V_{peak}$  between Coulomb blockade peaks in backgate voltage, and then putting this value into a theoretical expression for the backgate-to-dot capacitance  $C_{bg-d}$ . Ruzin *et al.* (1992) predicted quasi-periodicity of Coulomb blockade conductance peaks in systems with multiple quantum dots of varying sizes in series. Waugh *et al.* (1995) found experimental evidence supporting these predictions when measuring the conductance through three quantum dots in series with different gate voltages in a GaAs/AlGaAs 2DEG system. Knowing that there are three dots in series along the nanowire and the relative sizes of the dots based on the spacing between conductance rings, I created a simple model using Matlab of three dots in series with no coupling. Figure 5.5(a)-(c) shows the conductance  $G$  through each dot in the model *vs.*  $V_{bg}$ , assuming all the dots are isolated. The line shape of the Coulomb blockade peaks is calculated from equation 2.8. In figure 5.5(d) the individual conductance from each dot is plotted on the same graph.

The current through the nanowire in the model will be non-zero only at backgate voltages where peaks from every dot overlap. Figure 5.6(a) zooms into a region of figure 5.5(d) in order to illustrate where the conductance peaks from all three dots overlap. In figure 5.6(a), a heuristic picture to visualize where the conductance is nonzero is formed by shading in the area under each set of peaks. The darkest shaded areas correspond to the backgate voltages where all three sets of Coulomb blockade peaks overlap. Note: Figure 5.6(a) is a heuristic picture to identify the number of conductance peaks and their

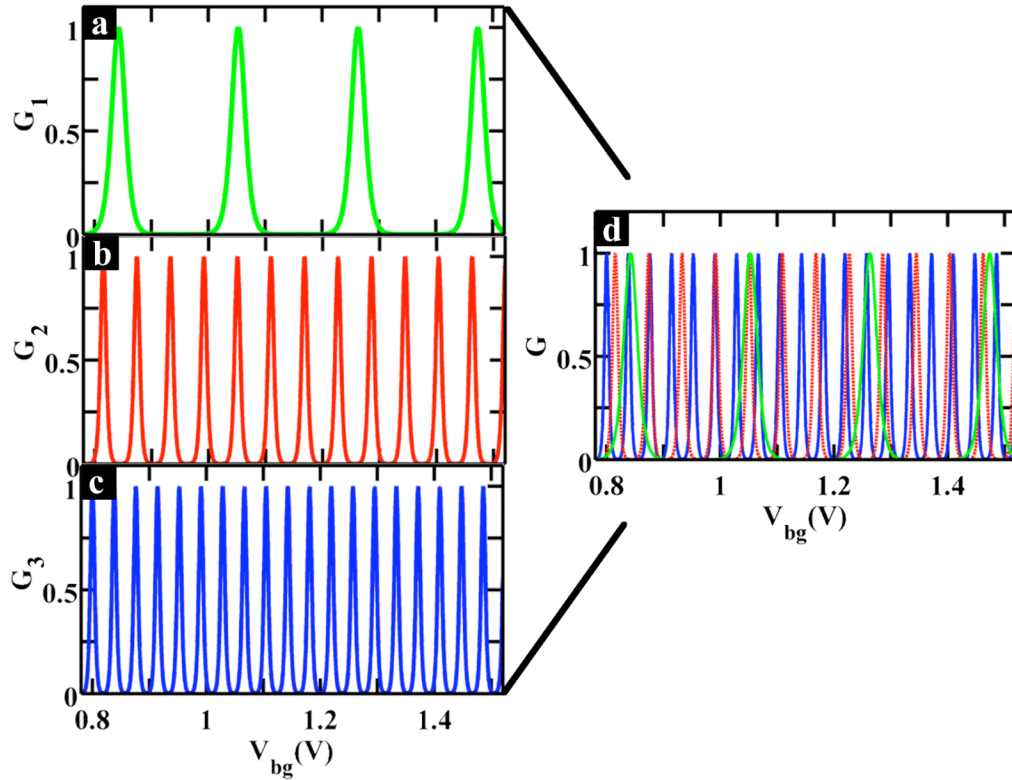


**Figure 5.5:** Simple theoretical model of three quantum dots with no coupling. (a)-(c) Plots the conductance  $G$  vs.  $V_{bg}$  for each dot, assuming that each dot is isolated. The dot in (a) is the smallest and has the largest  $E_c$ . The quantum dots in (b) and (c) are larger and similar in size to each other, with (c) being a little larger and having a smaller  $E_c$ . If the dots in (a)-(c) were in series in a nanowire, current would flow only at values of  $V_{bg}$  where all three sets of Coulomb blockade peaks overlap. (d) Plots the conductance from each dot on the same graph.

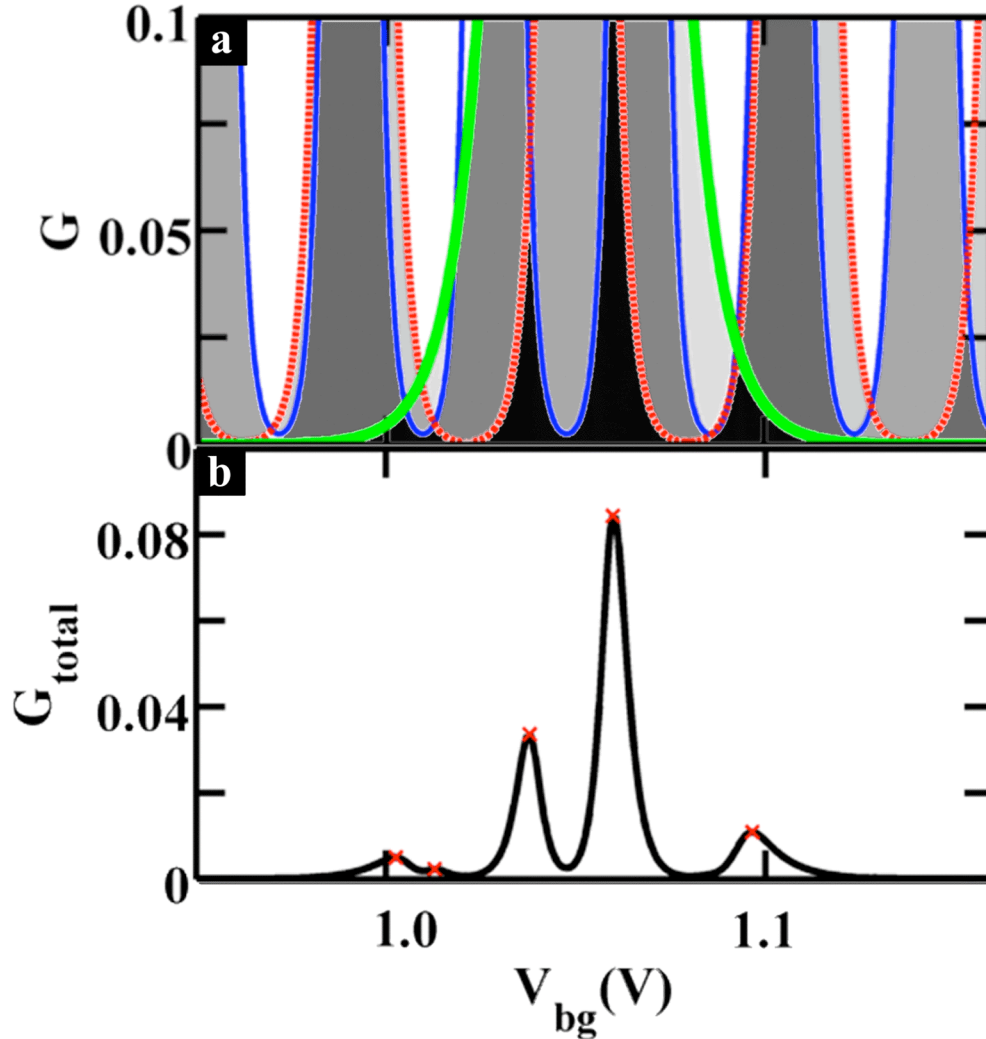


**Figure 5.6:** Simple theoretical model of three quantum dots with no coupling. (a) Zooms in on a region of 5.5(d) to more clearly demonstrate the regions of non-zero overlap. The area under each set of peaks is shaded in to illustrate that all three sets of Coulomb blockade peaks overlap at the black shaded backgate voltages (a) A plot of the total conductance  $G_{total}$  vs.  $V_{bg}$  through the three dots from 5.5(a)-(c) in series. If the dots are in series in a nanowire, current would flow only when the total conductance  $G_{total} = G_1 G_2 G_3 / (G_1 G_2 + G_2 G_3 + G_3 G_1)$  is non-zero. (a) Provides a heuristic picture of the number of Coulomb blockade peaks in  $G_{total}$  and an approximate idea of the peaks location in backgate voltage.

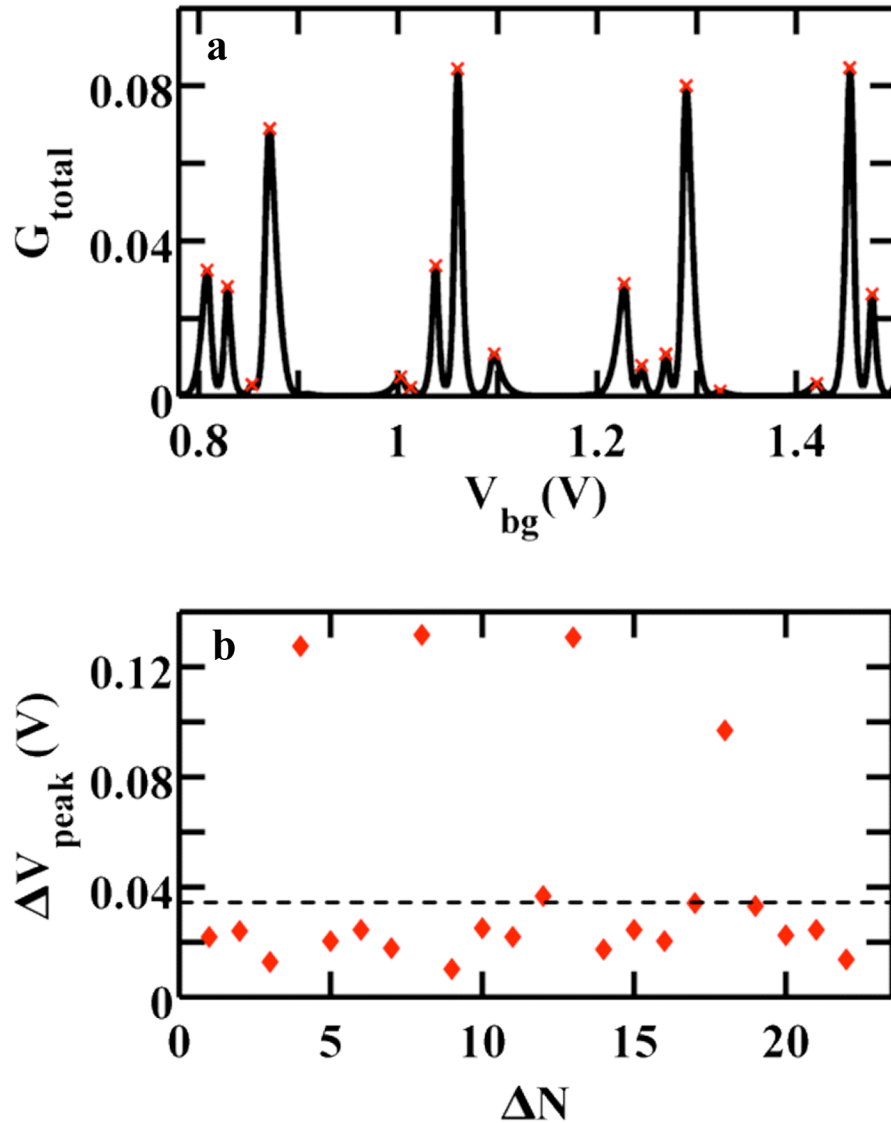


**Figure 5.7:** Demonstration of finding the minimum voltage difference  $\Delta V_{peak}$  between Coulomb blockade peaks for the simple theoretical model of three dots in series from figure 5.4. (a) A plot of the total conductance  $G_{total}$  vs.  $V_{bg}$  through the three dots in series. The apex of each Coulomb blockade peak is marked with a red x. In (b) the voltage difference  $\Delta V_{peak}$  between peaks in (a) is plotted vs. the difference in peak number  $\Delta N$ . The  $\Delta V_{peak}$  from the largest dot with the smallest energy, figure 5.4(c), is the same as the minimum average peak spacing  $\Delta V_{peak} \approx 0.04$  V, marked with the dashed line in (b). This method allows the extraction of the length of the largest dot of three dots in series in a nanowire.

approximate location, not the total conductance. Figure 5.6(b) shows for the zoomed-in range of  $V_{bg}$  the theoretical conductance  $G_{total}$  vs.  $V_{bg}$  for a nanowire with the three dots from figure 5.5 in series. The total conductance  $G_{total}$  in the model is  $G_{total} = G_1 G_2 G_3 / (G_1 G_2 + G_2 G_3 + G_3 G_1)$ . Figure 5.6(b) shows that the number of peaks in  $G_{total}$  corresponds to the number of times the Coulomb blockade peaks of the isolated dots overlap.

Figure 5.7(a) plots  $G_{total}$  vs.  $V_{bg}$  for the entire zoomed-out range of  $V_{bg}$ . Figure 5.7(a) is qualitatively similar to a sweep of  $|I_{sd}|$  vs.  $V_{bg}$  from the Coulomb blockade diamond plot in figure 5.3. The similarities between the theory and the data include variations in spacing between adjacent Coulomb blockade peaks and differences in peak amplitudes. In figure 5.7(b) the calculated voltage differences  $\Delta V_{peak}$  between Coulomb blockade peaks from the model in figure 5.7(a) is plotted vs. the difference  $\Delta N$  in the peak number. The average of the minimum peak spacing  $\Delta V_{peak} \approx 0.04$  V, which is marked with a dashed line in figure 5.7(b), corresponds to the  $\Delta V_{peak}$  spacing from the largest dot in the model with the smallest charging energy  $E_c$ , figure 5.5(c).

Using the method demonstrated by the simple model of three dots in series, we find the length  $l_{ep}$  of the epitaxially grown dot. Figure 5.8(a) is a trace of  $I_{sd-offset}$  vs.  $V_{bg}$  taken from a line cut of the Coulomb blockade diamond plot in figure 5.3 at  $V_{sd} = 5$  mV with no tip present. Knowing from conductance images that there are three dots in series along the nanowire, the voltage difference  $\Delta V_{peak}$  between Coulomb blockade peaks due to the longest dot is the average of the closest spaced Coulomb blockade peaks in figure 5.8(a). In figure 5.8(b) the spacing  $\Delta V_{peak}$  between adjacent Coulomb blockade

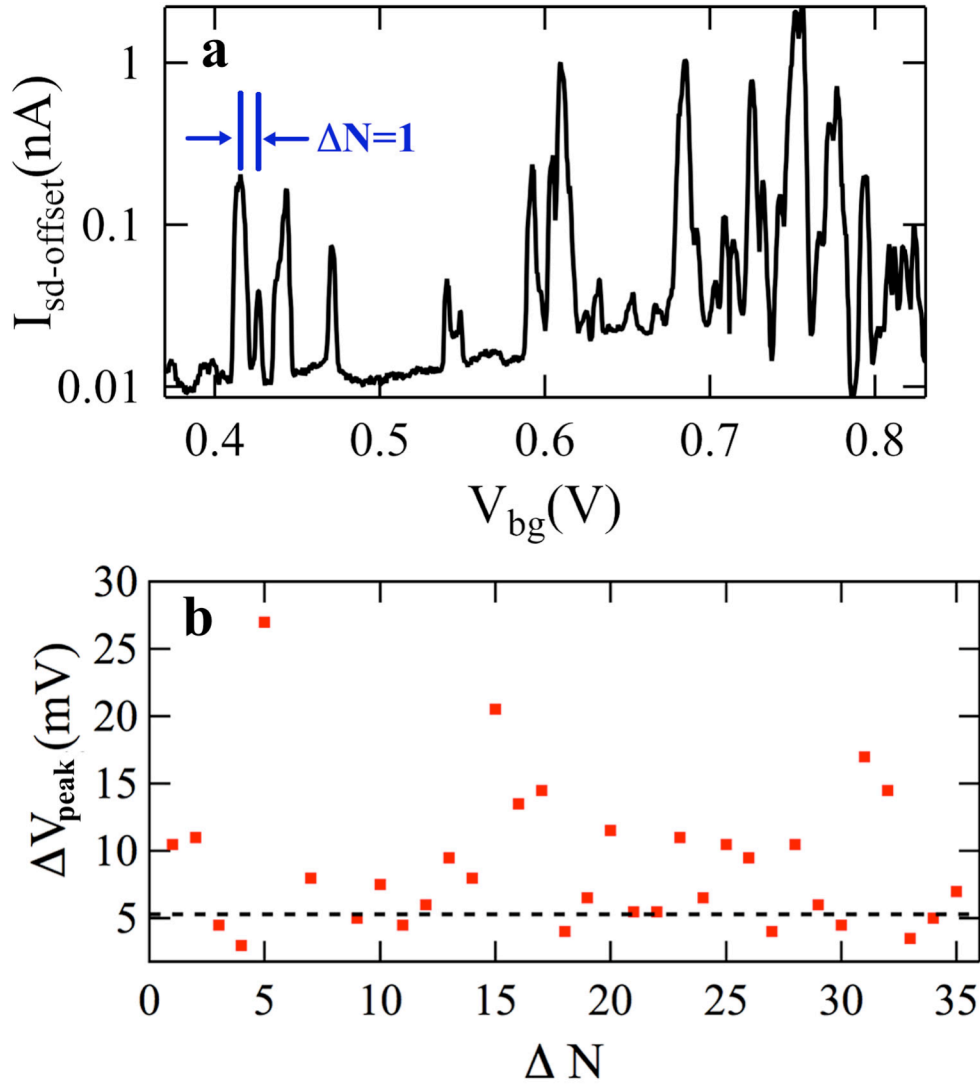


**Figure 5.8:** Experimental transport measurements of the ultra-thin nanowire without the tip present at  $T = 4.2$  K. (a)  $I_{sd\text{-offset}}$  vs.  $V_{bg}$  from the Coulomb blockade diamond plot in figure 5.2 at  $V_{sd} = 5$  mV. Coulomb blockade peaks of varying height and spacing are seen. (b) Plot of the measured voltage differences  $\Delta V_{peak}$  between adjacent Coulomb blockade peaks from (a) vs. the difference  $\Delta N$  in the number of electrons in the quantum dot. The dashed line marks the average  $\Delta V_{peak} = 5.5$  mV of the closest peak spacings, which corresponds to the voltage difference between peaks due to the longest dot in the system.

peaks from figure 5.8(a) is plotted vs.  $\Delta N$  the change in the number of the Coulomb blockade peaks in figure 5.8(a). A well-defined minimum spacing  $\Delta V_{peak} = 5.5$  mV is clearly visible in figure 5.8(b), indicated by the dashed line. To find  $l_{ep}$  we use the equation for the capacitance per unit length of a cylinder above a conducting plane [Yao *et al.* 2001]:

$$C_{bg-d} = \frac{2\pi\epsilon_r\epsilon_o l_{dot}}{\ln(2z/r_{dot})} \quad (5.1)$$

where  $\epsilon_r = 4.4$  is the dielectric constant of SiO<sub>2</sub>,  $\epsilon_o$  is the permittivity of free space,  $z = 100$  nm is the thickness of the SiO<sub>2</sub> layer, and  $r_{dot} = 15$  nm is the radius of the nanowire. The measured capacitance  $C_{bg-d}$  between the backgate and the epitaxially grown dot can also be approximated using equation 2.7 and neglecting the effect of the discrete energy spectrum to find  $C_{bg-d} \approx e/\Delta V_{peak} \approx 30$  aF. Inserting  $C_{bg-d}$  into equation 5.1 we find  $l_{ep} \approx 310$  nm. The measured length of the epitaxially grown InAs dot agrees with the nominal length 300 nm predicted by the growth conditions.

The relative sizes of the three dots are determined by comparing the spacing  $\Delta r$  between the rings in a conductance image for a particular dot with fixed  $V_{tip}$  and  $V_{bg}$  [Bleszynski *et al.* 2007], such as in figure 5.4. The spacing  $\Delta r$  is inversely proportional to the capacitance  $C_{l-d}$  between the SGM tip and that quantum dot. For the epitaxial dot in figure 5.4 there is a spacing of approximately 26 nm between rings giving  $\Delta r_{ep} \approx 26$  nm. We find the length of the additional dots by comparing the ratios of their ring spacing  $\Delta r_{dot1}$  and  $\Delta r_{dot3}$  with  $\Delta r_{ep}$ . We find for dot 1 the length  $l_{dot1} \approx 300$  nm,

comparable to the distance between the InP barrier and the metal contact. The length  $l_{dot3} \approx 50$  nm of dot 3 is shorter, suggesting that it is defined in part by disorder.

### 5.4.3 Capacitances of epitaxial dot

Conductance images contain spatial information useful for measuring other dot parameters such as the tip-to-dot capacitance  $C_{t-d}$  and the backgate-to-dot capacitance  $C_{bg-d}$ , which are useful to qualitatively determine the strength of the coupling. We find the ratio  $C_{t-d}/C_{bg-d}$  by comparing the change in tip voltage  $\Delta V_{ele-tip}$  and the change in backgate voltage  $\Delta V_{ele-bg}$  needed to add an electron to the epitaxial dot. Figure 5.9 shows a series of conductance images taken as the tip voltage is changed from  $V_{tip} = -0.6$  V to  $-1.0$  V. The scan location is chosen to image the epitaxially grown dot. The conductance rings move outwards in figure 5.9(a)-(e) as  $V_{tip}$  is made more negative, as indicated by the solid white ring. The change  $\Delta V_{ele-tip}$  needed to add an electron to the epitaxial dot, without moving the tip, was found by sweeping  $V_{tip}$  until a conductance ring moves outward by the ring spacing  $\Delta r_{ep}$ . We find that the change needed to add an electron to the epitaxial dot is  $\Delta V_{ele-tip} \approx 0.23$  V when the tip is a distance  $r_{tip} \approx 200$  nm from the dot.

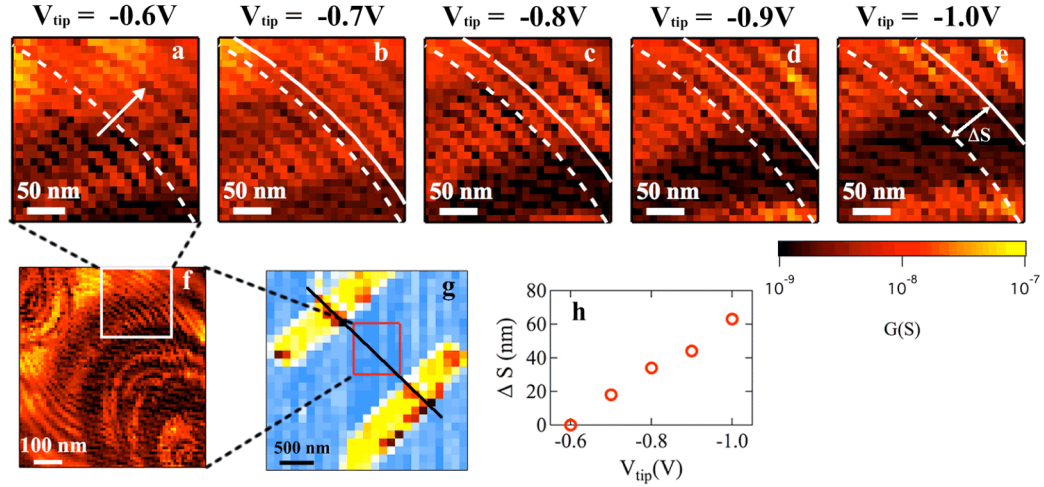


**Figure 5.9:** SPM spatial conductance images of an ultra-thin InAs/InP nanowire at  $T = 4.2$  K. A change in the tip voltage or tip position alters the induced charge on the dots:  $q = C_{t-d}(r_{tip}) V_{tip}$ . Figure 5.9(a)-(e) tracks the spatial progression of a specific conductance ring of the epitaxially grown dot, as the tip voltage is made more negative. (a)-(e) The dotted white curve marks the location of the specific conductance ring at  $V_{tip} = -0.6$  V. The solid white curves in (b)-(e) track the outward advancement of the same conductance ring as the tip voltage is made more negative. Figure 5.9(f) shows the region of interest in (a)-(e). (g) The location of the larger scan area, red box, relative to the Ni/Au leads (yellow) and the nanowire axis (black line). (h) Plot of the outward movement of the conductance ring marked with the dashed white line in (a) as the tip voltage is made more negative.  $\Delta S$  is the separation between the location of the conductance ring at the reference voltage,  $V_{tip} = -0.6$  V, and the current value of  $V_{tip}$ .

The change in backgate voltage  $\Delta V_{ele-bg}$  needed to add an electron is found from figure 5.10, which shows a series of conductance images recorded with a fixed  $V_{tip}$  as the backgate voltage  $V_{bg}$  is varied from 0.722 V to 0.714 V. The solid white ring tracks the motion of one conductance ring as  $V_{bg}$  is decreased. We use a procedure analogous to that in the previous paragraph to find the change  $\Delta V_{ele-bg} \approx 0.08$  V needed to add an electron to the dot without moving the tip.

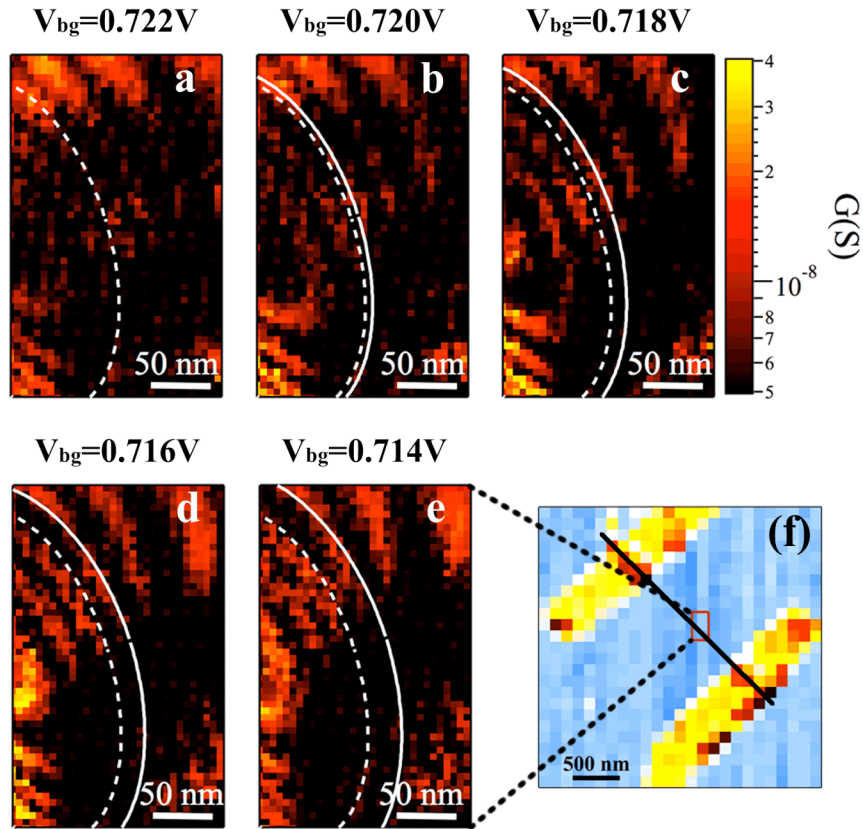


**Figure 5.10:** SPM spatial conductance images of an ultra-thin InAs/InP nanowire at  $T = 4.2$  K. Changing the backgate voltage and tip position can also alter the charge state of a quantum dot. Figure 5.10(a)-(e) tracks the spatial progression of a specific conductance ring of the epitaxially grown dot as the backgate voltage is made more negative. The dotted white curve marks the location of the specific conductance ring at  $V_{bg} = 0.722$  V. The solid white curves in (b)-(e) track the outward advancement of the same conductance ring as the backgate voltage is decreased. (f) The location of the scan area, red box, relative to the Ni/Au leads (yellow) and the nanowire axis (black line).

Using data from figures 5.9 and 5.10, we find the tip-to-dot capacitance  $C_{t-d}$  for the epitaxially grown dot. The ratio  $C_{t-d}/C_{bg-d}$  of the tip-to-dot capacitance and the backgate-to-dot capacitance is found from:

$$e = C_{t-d}\Delta V_{ele-tip} = C_{bg-d}\Delta V_{ele-bg} \quad (5.2)$$

The capacitance  $C_{bg-d}$  between the backgate and the epitaxially grown dot is found from  $C_{bg-d} = e/\Delta V_{peak}$  using  $\Delta V_{peak} = 5.5$  mV from figure 5.8(b). We find  $C_{t-d} \sim 10$  aF when  $r_{tip} \approx 200$  nm from the epitaxially grown dot. This value is much smaller than  $C_{\Sigma}$  showing that the tip is effective as a weakly coupled probe of the system.

## 5.5 Metal/semiconductor contacts

In future experiments we hope to optimize the metal contacts to the nanowires to form ohmic contacts. As mentioned in section 5.4.1 the quantum dots to either side of the epitaxially grown dot are likely formed by Schottky barriers at the metal/semiconductor interface. The recipe used for the Ni/Au metal contacts, chapter 3, has produced high quality contacts for nanowires with wider diameters ( $d_{dot} \approx 50 - 60$  nm). An ultra-thin nanowire has fewer available states due to its width, which may increase the likelihood of forming Schottky barriers. For future experiments we plan to grow n-doped portions of the nanowire leads, where the metal makes contact, in order to increase the number of available states and avoid a Schottky barrier.

# Chapter 6

## Summary and future directions

In this work we demonstrated that a scanning gate microscope is a powerful instrument to use to explore nanoscale systems. Imaging the motion of electrons provides spatial information regarding the electrical properties of nanostructures on a local scale. The scanning gate microscope (SGM) tip is capacitively coupled to the electron gas, which allows electrons under the surface of a nanostructure to be studied. Ultra-thin InAs/InP heterostructure nanowires are of special interest because they offer the opportunity to study interesting physical phenomena in 1D systems and for their potential as building blocks for future nanoelectronics or quantum information processing.

In chapter 4 we proposed and demonstrated via simulations an imaging technique to extract information about the amplitude of the 1D electron wavefunction in a quantum dot defined in an ultra-thin nanowire. Using first-order perturbation theory, the amplitude of the wavefunction can be found by taking deconvolving the tip potential with

the change in energy of the dot as a function of tip position. We then showed that the change in energy of the dot can be measured using the SGM. The SGM tip is scanned in a straight line above the nanowire while the backgate voltage is changed to maintain a constant nanowire conductance. The change in backgate voltage as a function of tip position is used to find the change in energy of the dot as a function of tip position.

By obtaining the change in energy from measurements and using a SGM tip with a known tip potential, the amplitude of the wavefunction can be extracted. The extraction technique combines a weakly perturbing scanning SGM tip with Coulomb blockade spectroscopy to extract the energy of the quantum states and the amplitude of the wavefunction with the same experimental tool. The knowledge gained from this technique will be valuable in designing and implementing future nanostructure devices.

In chapter 5 we imaged ultra-thin InAs nanowires with two epitaxially defined InP barriers using our home-built liquid-He cooled SGM. We identified and spatially located three individual quantum dots in series along the length of the nanowire. Without a SGM the location of these dots and their characteristics would have been difficult to discern. SGM conductance images disentangle the transport information for the three dots by spatially resolving the Coulomb blockade rings for each dot. The center quantum dot is the epitaxially grown dot, which is defined by two InP barriers. Additional quantum dots, one to either side of the epitaxially defined dot, were discovered in the conductance images. The location of the additional dots suggests that they were formed by Schottky barriers and disorder at the metal/semiconductor interfaces. The length of the epitaxially grown quantum dot was found by knowing the number of dots along the

nanowire from SGM images and from the Coulomb blockade peaks from transport data. Using the spacing between Coulomb blockade conductance rings for each dot, we determined the length of the other quantum dots in the system. The change in tip position and voltage needed to change the electron number on the quantum dot was found, and the relative coupling strengths of the dots were determined.

With this information, we can now optimize the growth process of the ultra-thin InAs/InP nanowires to reduce the disorder at the interfaces and to control the electron number to produce a simplified system conducive to imaging and probing 1D physical phenomena. Simplified high quality ultra-thin nanowire quantum dots will be exciting systems to test the wavefunction extraction technique proposed and demonstrated via simulations in this work.

# Bibliography

Aidala, K.E. (2006). “Imaging magnetic focusing in a two-dimensional electron gas,” Ph.D. Thesis, Harvard University.

Aidala, K.E., R.E. Parrott, T. Kramer, E.J. Heller, R.M. Westervelt, M.P. Hanson, and A.C. Gossard (2007). “Imaging magnetic focusing of coherent electron waves,” *Nature Phys.* **3**, 464.

Auslaender, O.M., H. Steinberg, A. Yacoby, Y. Tserkovnyak, B.I. Halperin, K.W. Baldwin, L. N. Pfeiffer, and K.W. West (2005). “Spin-charge separation and localization in one dimension,” *Science* **308**, 88.

Beenakker, C.W.J. (1991). “Theory of Coulomb-blockade oscillations in the conductance of a quantum dot,” *Phys. Rev. B* **44**, 1646.

Berezovsky, J., M.F. Borunda, E.J. Heller, and R.M. Westervelt (2010). “Imaging coherent transport in graphene (part I): mapping universal conductance fluctuations,” *Nanotechnology* **21**, 274013.

Berezovsky, J. and R.M. Westervelt (2010). “Imaging coherent transport in graphene (part II): probing weak localization,” *Nanotechnology* **21**, 274014.

Björk, M.T., B.J. Ohlsson, T. Sass, A.I. Persson, C. Thelander, M.H. Magnusson, K. Deppert, L.R. Wallenberg, and L. Samuelson (2002). “One-dimensional heterostructures in semiconductor nanowhiskers,” *Appl. Phys. Lett.* **80**, 1058.

Björk, M.T., B.J. Ohlsson, T. Sass, A.I. Persson, C. Thelander, M.H. Magnusson, K. Deppert, L.R. Wallenberg, and L. Samuelson (2002). “One-dimensional steeplechase for electrons realized,” *Nano Lett.* **2**, 87.

Björk, M.T., C. Thelander, A.E. Hansen, L.E. Jensen, M.W. Larsson, L.R. Wallenberg, and L. Samuelson (2004). “Few-electron quantum dots in nanowires,” *Nano Lett.* **4**, 1621.

- Björk, M.T., A. Fuhrer, A.E. Hansen, M.W. Larsson, L.E. Fröberg, and L. Samuelson (2005). "Tunable effective  $g$  factor in InAs nanowire quantum dots," *Phys. Rev. B* **72**, 201307(R).
- Björk, M.T., J. Knoch, H. Schmid, H. Riel, and W. Riess (2008). "Silicon nanowire tunneling field-effect transistors," *Appl. Phys. Lett.* **92**, 193504.
- Bleszynski, A. (2006). "Imaging electrons in semiconductor nanostructures," Ph.D. Thesis, Harvard University.
- Bleszynski-Jayich, A.C., L.E. Fröberg, M.T. Björk, H.J. Trodahl, L. Samuelson, and R.M. Westervelt (2008). "Imaging a one-electron InAs quantum dot in an InAs/InP nanowire," *Phys. Rev. B* **77**, 245327.
- Blick, R.H., R.J. Haug, J. Weis, D. Pfannkuche, K.v. Klitzing, and K. Eberl (1996). "Single-electron tunneling through a double quantum dot: The artificial molecule," *Phys. Rev. B* **53**, 7899.
- Bryllert T., L. Wernersson, L.E. Fröberg, and L. Samuelson (2006). "Vertical high-mobility wrap-gated InAs nanowire transistor," *IEEE Electron Device Letters* **27**, 323.
- Chan I.H., P. Fallahi, A. Vidan, R.M. Westervelt, M. Hanson and A.C. Gossard (2004). "Few-electron double quantum dots," *Nanotechnology* **15**, 609.
- Dai, H., E.W. Wong, and C.M. Lieber (1996). "Probing electrical transport in nanomaterials: conductivity of individual carbon nanotubes," *Science* **272**, 523.
- De Picciotto, R., K.W. Baldwin, L.N. Pfeiffer, and K.W. West (2008). "The 0.7 structure in cleaved edge overgrowth wires," *J. Phys.: Condens. Matter* **20**, 164204.
- Deshpande, V.V. and M. Bockrath (2008). "The one-dimensional Wigner crystal in carbon nanotubes," *Nature* **4**, 314.
- Fallahi, P., A.C. Bleszynski, R.M. Westervelt, J. Huang, J.D. Walls, E.J. Heller, M. Hanson, and A.C. Gossard (2005). "Imaging a single-electron quantum dot," *Nano Lett.* **5**, 223.
- Fallahi, P. (2006). "Imaging electrons in few-electron quantum dots," Ph.D. Thesis, Harvard University.
- Fiete, G.A. (2007). "Colloquium: The spin-incoherent Luttinger liquid," *Rev. Mod. Phys.* **79**, 801.

- Fuhrer A., L.E. Fröberg, J.N. Pedersen, M.W. Larsson, A. Wacker, M. Pistol, and L. Samuelson (2007). "Few electron double quantum dots in InAs/InP nanowire heterostructures," *Nano Lett.* **7**, 243.
- Gildemeister, A.E., T. Ihn, R. Schleser, K. Ensslin, D.C. Driscoll, and A.C. Gossard (2007). "Imaging a coupled quantum dot-quantum point contact system," *J. Appl. Phys.* **102**, 083703.
- Goni, A.R., L.N. Pfeiffer, K.W. West, A. Pinczuk, H.U. Baranger, and H.L. Stormer (1992). "Observation of quantum wire formation at intersecting quantum wells," *Appl. Phys. Lett.* **61**, 1956.
- Hanson, R., L.P. Kouwenhoven, J.R. Petta, S. Tarucha, and L.M.K. Vandersypen (2007). "Spins in few-electron quantum dots," *Rev. Mod. Phys.* **79**, 1217.
- Heller E.J., M.F. Crommie, C.P. Lutz, and D.M. Eigler (1994). "Scattering and absorption of surface electron waves in quantum corrals," *Nature* **369**, 464.
- Hiruma, K., M. Yazawa, K. Haraguchi, K. Ogawa, T. Katsuyama, M. Koguchi, and H. Kakibayashi (1993). "GaAs free-standing quantum-size wires," *J. Appl. Phys.* **74**, 3162.
- Hiruma, K., H. Murakoshi, M. Yazawa, and T. Katsuyama (1996). "Self-organized growth of GaAs/InAs heterostructure nanocylinders by organometallic vapor phase epitaxy," *J. Crystal Growth* **163**, 226.
- Iijima, S. (1991). "Helical microtubules of graphitic carbon," *Nature* **354**, 56.
- Jensen, L.E., M.T. Björk, S. Jeppesen, A.I. Persson, B.J. Ohlsson, and L. Samuelson (2004). "Role of surface diffusion in chemical beam epitaxy of InAs nanowires," *Nano Lett.* **4**, 1961.
- Jura, M.P., M.A. Topinka, L. Urban, A. Yazdani, H. Shtrikman, L.N. Pfeiffer, K.W. West, and D. Goldhaber-Gordon (2007). "Unexpected features of branched flow through high-mobility two-dimensional electron gases," *Nature Phys.* **3**, 841.
- Kouwenhoven, L.P., N.C. van der Vaart, A.T. Johnson, W. Kool, C.J.P.M. Harmans, J.G. Williamson, A.A.M. Staring, and C.T. Foxon (1991). "Single electron charging effects in semiconductor quantum dots," *Z. Phys. B* **85**, 367.
- Kouwenhoven, L.P., D.G. Austing, and S. Tarucha (2001). "Few-electron quantum dots," *Rep. Prog. Phys.* **64**, 701.

- Larsson, M.W., J.B. Wagner, M. Wallin, P. Hakansson, L.E. Fröberg, L. Samuelson, and L.R. Wallenberg (2007). "Strain mapping in free-standing heterostructured wurtzite InAs/InP nanowires," *Nanotechnology* **18**, 015504.
- Lemay, S.G., J.W. Janssen, M. van den Hout, M. Mooij, M.J. Bronikowski, P.A. Willis, R.E. Smalley, L.P. Kouwenhoven, and C. Dekker (2001). "Two-dimensional imaging of electronic wavefunctions in carbon nanotubes," *Nature* **412**, 617.
- LeRoy, B.J., Topinka, M.A., Westervelt, R.M., Maranowski, K.D., Gossard, A.C. (2002). "Imaging electron density in a two-dimensional electron gas," *Appl. Phys. Lett.* **80**, 4431.
- LeRoy, B.J. (2003). "Imaging coherent electron flow through semiconductor nanostructures," Ph.D. Thesis, Harvard University.
- LeRoy, B.J., A.C. Bleszynski, K.E. Aidala, R.M. Westervelt, A. Kalben, E.J. Heller, S.E.J. Shaw, K.D. Maranowski, and A.C. Gossard (2005). "Imaging electron Interferometer," *Phys. Rev. Lett.* **94**, 126801.
- Lieber, C.M. (2003). "Nanoscale science and technology: building a big future from small things," *MRS Bull.* **28**, 486.
- Livermore, C., C.H. Crouch, R.M. Westervelt, K.L. Campman, and A.C. Gossard (1996). "The Coulomb Blockade in Coupled Quantum Dots," *Science* **274**, 1332.
- Loss, D. and D.P. DiVincenzo (1998). "Quantum computation with quantum dots," *Phys. Rev. A* **57**, 120.
- Manoharan, H.C., C.P. Lutz, and D.M. Eigler (2000). "Quantum mirages formed by coherent projection of electronic structure," *Nature* **403**, 512.
- Matveev, K.A. (2004). "Conductance of a quantum wire at low electron density," *Phys. Rev. B* **70**, 245319.
- Matveev, K.A. (2004). "Conductance of a quantum wire in the Wigner-Crystal Regime," *Phys. Rev. Lett.* **92**, 106801.
- Mendoza, M. and P. A. Schulz (2003). "Wave-function mapping conditions in open quantum dot structures," *Phys. Rev. B* **68**, 205302.
- Meyer, E., H.J. Hug, and R. Bennewitz (2004). "Scanning probe microscopy: the lab on a tip," Springer-Verlag, Berlin.
- Moon, C.R., L.S. Mattos, B.K. Foster, G. Zeltzer, W. Ko, and H.C. Manoharan (2008). "Quantum phase extraction in isospectral electronic nanostructures," *Science* **319**, 782.

- Nogueira, A. and A. Latge (1998). "Mapping the electronic wave functions by determining current-voltage curves," *Phys. Rev. B* **57**, 1649.
- Olsson, L.Ö., C.B.M. Andersson, M.C. Håkansson, J. Kanski, L. Ilver, and U.O. Karlsson (1996). "Charge accumulation at InAs surfaces," *Phys. Rev. Lett.* **76**, 3626.
- Ohlsson, B.J., M.T. Björk, H. Magnusson, K. Deppert, L. Samuelson, and L.R. Wallenberg (2001). "Size-, shape-, and position-controlled GaAs nano-whiskers," *Appl. Phys. Lett.* **79**, 3335.
- Oppenheim, A. V. and A. S. Willsky (1997). "Signals & Systems Second Edition," Prentice Hall Upper Saddle River, New Jersey.
- Qian, J., B.I. Halperin, and E.J. Heller (2010). "Imaging and manipulating electrons in a one-dimensional quantum dot with Coulomb blockade microscopy," *Phys. Rev. B* **81**, 125323.
- Ruzin, I.M., V. Chandrasekhar, E.I. Levin, and L.I. Glazman (1992). "Stochastic Coulomb blockade in a double-dot system," *Phys. Rev. B* **45**, 13469.
- Samuelson, L., C. Thelander, M.T. Bjork, and M. Borgstrom (2004). "Semiconductor nanowires for 0D and 1D physics and applications," *Physica E (Amsterdam)* **25**, 313.
- Schnez, S., J. Güttinger, M. Huefner, C. Stampfer, K. Ensslin, and T. Ihn (2010). "Imaging localized states in graphene nanostructures," *Phys. Rev. B* **82**, 165445.
- Stopa, M. (2002). "Rectifying behavior in Coulomb blockades: charging rectifiers," *Phys. Rev. Lett.* **88**, 146802.
- Tans, S.J., M.H. Devoret, H. Dai, A. Thess A, R.E. Smalley, L.J. Geerligs, and C. Dekker (1997). "Individual single-wall carbon nanotubes as quantum wires," *Nature* **386**, 474.
- Tarucha, S., D.G. Austing, T. Honda, R.J. van der Hage, L.P. Kouwenhoven (1996). "Shell filling and spin effects in a few electron quantum dot," *Phys. Rev. Lett.* **77**, 3613.
- Tessmer, S.H., P.I. Glicofridis, R.C. Ashoori, L.S. Levitov, and M.R. Melloch (1998). "Subsurface charge accumulation imaging of a quantum Hall liquid," *Nature* **392**, 51.
- Tinkham, M. (1996). "Introduction to Superconductivity," McGraw-Hill, New York.
- Topinka, M.A., B.J. LeRoy, S.E.J. Shaw, E.J. Heller, R.M. Westervelt, K.D. Maranowski, and A.C. Gossard (2000). "Imaging coherent electron flow from a quantum point contact," *Science* **289**, 2323.

Topinka, M.A., B.J. LeRoy, R.M. Westervelt, S.E.J. Shaw, R. Fleischmann, E.J. Heller, and K. Maranowski (2001). "Coherent branched flow in a two-dimensional electron gas," *Nature* **410**, 183.

Topinka, M. A. (2002). "Imaging coherent electron wave flow through 2-D electron gas nanostructures," Ph.D. Thesis, Harvard University.

Trodahl, H., E. Boyd, K. Nilsson, L. Fröberg, L. Samuelson, and R.M. Westervelt (2009). "Imaging double quantum dots in InAs/InP nanowires," American Physical Society March Meeting 2009, Pittsburgh, Pennsylvania.

van der Wiel, W.G., S. De Franceschi, J.M. Elzerman, T. Fujisawa, S. Tarucha and L.P. Kouwenhoven (2003). "Electron transport through double quantum dots," *Rev. Mod. Phys.* **75**, 1.

Vidan, A., R.M. Westervelt, M. Stopa, M. Hanson and A.C. Gossard (2004). "Triple Quantum Dot Charging Rectifier," *Appl. Phys. Lett.* **85**, 3602.

Vidan, A. (2006). "Charge and spin effects in semiconductor nanowires," Ph.D. Thesis, Harvard University.

Waugh, F.R., M.J. Berry, D.J. Mar, R.M. Westervelt, K.L. Campman, and A.C. Gossard (1995). "Single-electron charging in double and triple quantum dots with tunable coupling," *Phys. Rev. Lett.* **75**, 705.

Woodside, M.T. and P.L. McEuen (2002). "Scanned probe imaging of single-electron charge states in nanotube quantum dots," *Science* **296**, 1098.

Yang, C., Z. Zhong, and C.M. Lieber (2005). "Encoding electronic properties by synthesis of axial modulation doped silicon nanowires," *Science* **310**, 1304.

# Appendix A

## Fitting the plane at cold temperatures

1. By scanning find a featureless (dust free) 1 V x 1 V area near the device and ensure that the feedback is positive over the entire scan area.
  - It is important to pick an area close to the device since there could be small changes in the plane as the tip moves away from the device.
2. Turn down the feedback.
3. Set the *tipH* voltage on the computer control window to 0 and then turn up the knob for the computer controlled z (*tipH* dial on the XYZ box).
4. Run the “flatteninside” macro.
5. Check the plane in Graph A (autoz, zoomout) and record the equation of the plane for future reference.
6. Turn down *tipH*.

7. Set  $V_{buffer}$  in the computer control window to a “safe” value. A negative voltage means the tip is above the sample. A positive voltage will destroy the tip. (Remember there is  $\sim -0.75$  V offset from the diode.) For nanowire samples a value of  $-3$  V is usually safe.
8. Turn on z-guide. (Click toggle button on left side of computer display.)
9. Add grounding cap to  $V_{Limit}$  on the XYZ box, this will allow the piezotube to pull-back if the tip comes in contact, but the tube will not push-out.
10. Turn up the feedback and  $tipH$  knobs.
11. Scan with limited feedback on and slowly lower  $V_{buffer}$  after each scan until tip starts to hit the leads to the device. This allows finding the nanowire’s location exactly without touching the tip to the nanowire.